2017

Three Dimensional Homology Modeling of Organic Cation Transporter 3 to Identify Structural Elements Mediating Transporter-substrate Interactions

Hebing Liu
Virginia Commonwealth University

THREE DIMENSIONAL HOMOLOGY MODELING OF ORGANIC CATION TRANSPORTER 3 TO IDENTIFY STRUCTURAL ELEMENTS MEDIATING TRANSPORTER-SUBSTRATE INTERACTIONS

A dissertation submitted in partial fulfillment of the requirements for the degree of Doctor of Philosophy at Virginia Commonwealth University

by

Hebing Liu
Bachelor of Science, China Pharmaceutical University, China, 2013

Director: Douglas H. Sweet, Ph.D.
Professor, Chair
Department of Pharmaceutics, School of Pharmacy

Virginia Commonwealth University
Richmond, Virginia,
May 3rd, 2017

ACKNOWLEDGEMENTS

First and foremost, I would like to thank my advisor Dr. Douglas H. Sweet for his guidance, patience, and all of his effort that helped me through my entire Ph.D. studies. He is the most intelligent and free-minded advisor I ever know, and his enthusiasm towards his research has been and always will be a motivation for me. Dr. Sweet has always been supportive and given me the freedom to pursue research with my interest, as well as taking up extra-curricula works and responsibilities that could help with my research and personal goals. I am truly grateful for his excellent guidance through these past years.

I would also like to thank all of my committee members Drs. Jürgen Venitz, Phillip Gerk, MaryPeace McRae, and Glen Kellogg for their consistent help in my research. Dr. Venitz and Dr. Gerk have given me numerous brilliant and valuable comments and suggestions in our PK/PD/DT research group, and Dr. McRae's help in our McSweet research group. I have benefited tremendously from these weekly discussions. I would like to thank Dr. Kellogg for his inspirations in modeling studies and his availabilities in all these meetings. I would like to thank Dr. Dukat and Dr. Iyer for providing synthesized test compounds for the antidepressant study. A special gratitude I would like to give to Dr. Phillip Mosier for providing feedbacks and guiding me to develop and finish my 3-D homology modeling studies.

In addition, many thanks go to all faculties in School of Pharmacy for their help in my coursework. I would also like to thank Ms. Keyetta Tate, Ms. Laura Georgiadis and Ms. Shakim Jackson for their kindly help in arranging departmental activities, lab and office supplies, paperwork, reimbursement, and so many other affairs.

I would like to thank my lab-mates Dr. Christine A. Farthing, Dr. Xiaolei Pan, Raymond Lai and Christopher Jay for their help in my study, and all my fellow and senior Pharmaceutics graduate students for their help and advice. In addition, a special thank you to my friends and roommates in Richmond for their support and encouragement.

I would thank the VCU School of Pharmacy, Graduate School and Lowenthal Award for the financial support.

Lastly, I would like to thank my family for all their love and encouragement. My parents raised me with all their love and supported me in all my pursuits. And most of all for my loving, supportive, encouraging, and patient boyfriend Jingyang Lu whose faithful support through my Ph.D. is so appreciated. Thank you.

TABLE OF CONTENTS

LIST OF TABLES

LIST OF FIGURES

List of ABBREVIATIONS

2-D	2-dimensional
3-D	3-dimensional
5-HT	Serotonin
AAPS	American Association of Pharmaceutical Scientists
ABC	ATP binding cassette
AdiC	Amino acid antiporter
ANOVA	Analysis of variance
AP	Alkaline phosphatase
APS	Ammonium persulfate
$ASBT_{NM}$	Apical sodium-dependent bile acid transporter
ASP	4-[4-(dimthylamino)-styryl]-N-methylpyridinium
ATP	Adenosine triphosphate
AUC	Area under the curve
BBB	Blood brain barrier
Blast	Basic local alignment search tool
BMEC	Brain microvessel endothelial cell
BSA	Bovine serum albumin
cDNA	Complementary DNA

CHO	Chinese hamster ovary
C_{max}	Maximum plasma concentration
CNS	Central nervous system
cSNP	Coding single nucleotide polymorphism
D-22	Decynium-22
Da	Dalton
DA	Dopamine
DAPI	4’,6-diamidino-2-phenylindol
DAT	Dopamine transporter
DDI	Drug-drug interaction
DNA	Deoxyribonucleic acid
dNTP	Deoxynucleotide triphosphate
DOPE	Discrete optimized protein energy
EDTA	Ethylene-diamine-tetra-acetic acid
EMA	European Medicines Agency
EV	Empty vector
FBS	Fetal bovine serum
FDA	Food and Drug Administration
Glp-T	Glycerol-3-phosphate transporter
HCl	Hydrochloride acid
HEK	Human embryonic kidney 293
HEPES	4-(2-hydroxyethyl)-1-piperazineethanesulfonic acid
IC_{50}	Half maximal inhibition concentration

IgG	Immunoglobulin G
KAc	Potassium acetate
K_m	Michaelis-Menten constant
LacY	Lactose permease
LB	Luria broth
mAb	Monoclonal antibody
MFS	Major facilitator superfamily
MPP^+	1-methyl-4-phenylpyridinium
mRNA	Messenger RNA
NaAc	Sodium acetate
Na_2HPO_4	Disodium phosphate
NaCl	Sodium chloride
NaH_2PO_4	Sodium phosphate
NaOH	Sodium hydroxide
NBT/BCIP	Nitroblue tetrazolium/5-bromo-4-chloro-3-indolyl phosphate
NCBI	National center for biotechnology information
NE	Norepinephrine
NET	Norepinephrine transporter
NMR	Nuclear magnetic resonance
NorM	Multidrug and toxic compound extrusion transporter
OCT	Organic cation transporter
OCTN	Novel organic cation transporter
PAGE	Polyacrylamide gel electrophoresis

PCR	Polymerase chain reaction
PD	Pharmacodynamics
PDB	Protein Data Bank
$PepT_{so}$	Peptide transporter
pH	Potential hydrogen
PiPT	*Piriformospora indica* high affinity phosphate transporter
PK	Pharmacokinetic
PVDF	Polyvinylidene difluoride
RNase	Ribonuclease
RT-PCR	Reverse transcription polymerase chain reaction
SD	Standard deviation
SDS	Sodium dodecyl sulfate
SERT	Serotonin transporter
SLC	Solute carrier
SNP	Single nucleotide polymorphism
SNRI	Serotonin and norepinephrine reuptake inhibitor
SSRI	Selective serotonin reuptake inhibitor
TBS	Tris-buffered saline
TEA^+	Tetraethylammonium
TEMED	Tetra-methyl-ethylene-diamine
TMD	Transmembrane domain
TPA^+	Tetrapentylammonium
Tris	Trisaminomethane

Uptake-1	High-affinity, low capacity reuptake transporters
Uptake-2	Low-affinity, high capacity reuptake transporters
vcCNT	Concentrative nucleoside transporter
V_d	Volume of distribution
V_{max}	Maximum velocity

ABSTRACT

THREE DIMENSIONAL HOMOLOGY MODELING OF ORGANIC CATION TRANSPORTER 3 TO IDENTIFY STRUCTURAL ELEMENTS MEDIATING TRANSPORTER-SUBSTRATE INTERACTIONS

By Hebing Liu, B.S.

A dissertation submitted in partial fulfillment of the requirements for the degree of Doctor of Philosophy at Virginia Commonwealth University

Virginia Commonwealth University

Director: Douglas H. Sweet, Ph.D.
Professor, Chair
Department of Pharmaceutics, School of Pharmacy

Organic cation transporters (OCTs) belong to the organic cation/anion/zwitterion transporter family SLC22, which is part of the major facilitator superfamily. The OCT family contains three influx transporters, OCT1, 2, and 3, which share high sequence homology. OCT1-3 exhibit broad tissue distribution, including the heart, intestine, kidney, liver, choroid plexus, neurons and brain capillaries [1]. They play a pivotal role in the absorption, tissue distribution, and excretion of a diverse array of substances, including drugs, toxins, xenobiotics and neurotransmitters (e.g. metformin, morphine,

serotonin) [1]. OCT substrates exhibit a wide variety of structural and physiochemical properties and currently the nature of the biochemical interactions between substrate and OCTs are unknown. Therefore, identifying which amino acid residues are critical for OCT-substrate interactions is of central importance to understanding and predicting interactions between drugs and OCTs. Our long-term goal is to identify and verify crucial amino acid residues for interaction at the substrate-binding pocket of human OCT3 (hOCT3), which will support breakthroughs in understanding drug absorption, clinical drug-drug interaction, and compound excretion, as well as inform rational drug design strategies for hOCT3 interacting drugs. The working hypothesis for this project is that substitution of hOCT3 residues involved in transporter-substrate interactions, implicated through *in silico* molecular modeling and docking studies, will result in altered affinity (K_m) of the transporter to the substrate.

A three-dimensional (3-D) homology model of human OCT3 was generated using the solved crystal structure of a high affinity phosphate transporter from *Piriformospora indica* (PiPT) as template. A putative binding pocket for the prototypical hOCT3 ligand 1-methyl-4-phenylpyridinium (MPP^+) was identified through docking studies and five residues, Phe36, Val40, Trp358, Glu451 and Asp478, were identified as potentially mediating hOCT3-MPP^+ interactions. Next, a series of conservative and non-conservative amino acid substitutions were introduced to these positions via site-directed mutagenesis. Screening experiments showed that conservative substitution at position Trp358 or Asp478, non-conservative substitution at position Val40, as well as the double mutant Phe36Tyr-Glu451Ala, each resulted in complete loss of MPP^+ transport activity by hOCT3. Kinetic analyses using generated cell lines expressing

functional hOCT3 mutants in isolation (Phe36Ala, Phe36Tyr, Val40Leu, Glu451Ala, Glu451Asp, Phe36Tyr-Val40Leu and Val40Leu-Glu451Ala) provided K_m values for MPP^+ of 29.1±2.0μM, 14.6±0.5μM, 32.2±4.3μM, 40.9±4.8μM, 23.4±3.9μM, 14.4±1.7μM and 70.0±9.7μM, respectively. Thus, the K_m values for all mutants, with the exception of Phe36Tyr and Phe36Tyr-Val40Leu, were significantly increased (indicating reduced affinity) over that of wild type hOCT3 (16.0±2.2μM). All of the residues identified through docking studies appear to influence MPP^+-hOCT3 binding interactions, with Trp358 and Asp478 being the two most important residues. Additionally, 3-D homology modeling of the functional hOCT3 mutant Val40Leu, and all non-functional hOCT3 mutants, indicated changes in binding pocket architecture consistent with weakening of ligand-transporter interactions. Docking of structurally divergent hOCT3 substrates indicated binding interactions in the same general region as that identified for MPP^+, albeit with mostly unique residues, suggesting the presence of one large binding pocket with substrate-specific contacts. Interspecies differences were explored by generating 3-D homology models for rat and murine Oct3. Results from docking studies using compounds exhibiting vastly different binding affinities (K_m or IC_{50}) towards the OCT3/Oct3 orthologs were consistent with varying strength in ligand-transporter binding pocket interactions being the underlying driver for interspecies differences in transporter affinity.

Finally, a series of novel compounds exhibiting anti-depressant-like activity was screened for OCT interaction *in vitro.* Results demonstrated significant inhibitory effects on OCTs for many of the compounds, with several being the most potent OCT inhibitors identified to date (e.g., KAI414). These data suggest that their pharmacological action

may be through inhibition of the OCT component of the uptake-2 system in the CNS. Based on their inhibition profiles, lead compounds (e.g., KAI414) were prioritized for conducting *in vivo* pharmacodynamic studies. Now, this series of compounds can be docked to our validated OCT3 3-D homology models to identify crucial functional groups for transporter-ligand interactions supporting further rational drug design.

In conclusion, this dissertation research successfully generated 3-D homology models for human, rat and murine OCT3/Oct3. Through a series of *in silico* and *in vitro* studies a ligand-binding region was defined, and putative residues mediating transporter-ligand interactions identified and verified. Docking studies with compounds exhibiting interspecies differences in affinity support the conclusion that differences in the binding pocket architecture and strength of molecular interactions with those residues form the basis for inter-species differences in transporter compound affinity.

CHAPTER 1

ORGANIC CATION TRANSPORTERS: IDENTIFICATION OF STRUCTURAL ELEMENTS IMPACTING TRANSPORTER-SUBSTRATE INTERACTIONS

1.1 Overview of Organic Cation Transporters

Progress has been made in understanding the role of membrane transporters in drug safety and efficacy [2]. In particular, more than 400 membrane transporters in two major families – the ATP-binding cassette (ABC) family, which directly binds and hydrolyzes ATP as a driving force for the unidirectional transport of substrates, and the solute carrier (SLC) family, which is indirectly coupled to cellular energy and utilize the membrane potential difference and/or the stored energy of chemical gradients as driving forces – have been annotated in the human genome [3]. Many of these transporters have been cloned, characterized, and localized to tissues and cellular membrane domains in the human body. The effect of transporters on drug disposition, therapeutic efficacy and other aspects has been demonstrated in numerous studies. Currently, the human SLC superfamily is comprised of over 50 separate gene families with a combination of more than 350 confirmed and putative transporter proteins [4]. The SLC22 family contains organic cation/anion/zwitterion transporters with about 30 identified/putative members including organic cation transporters (OCTs and OCTNs), which may interact with hundreds of organic cations, weak bases and some neutral compounds [1].

The members of the SLC22 transporter family are all characterized by 12 α-helical transmembrane domains (TMDs) with a pseudosymmetry between TMDs 1 – 6 and 7 – 12, a large extracellular loop located between TMDs 1 and 2 with three glycosylation sites that are hypothesized to mediate homo-oligomerization and intracellular routing, as well as six sulfhydryl groups (conserved cysteine residues) that could potentially form disulfide bridges; a large intracellular loop between TMDs 6 and 7, which is proposed to be involved in posttranscriptional regulation (through phosphorylation), and intracellular N- and C-termini (hypothesized structure of the SLC22 transporter family shown in Figure 1.1) [5, 6]. OCTs utilize electrochemical gradients of the transported compounds as their driving forces to uptake organic cations into the negatively charged intracellular environment as facilitated diffusion carriers.

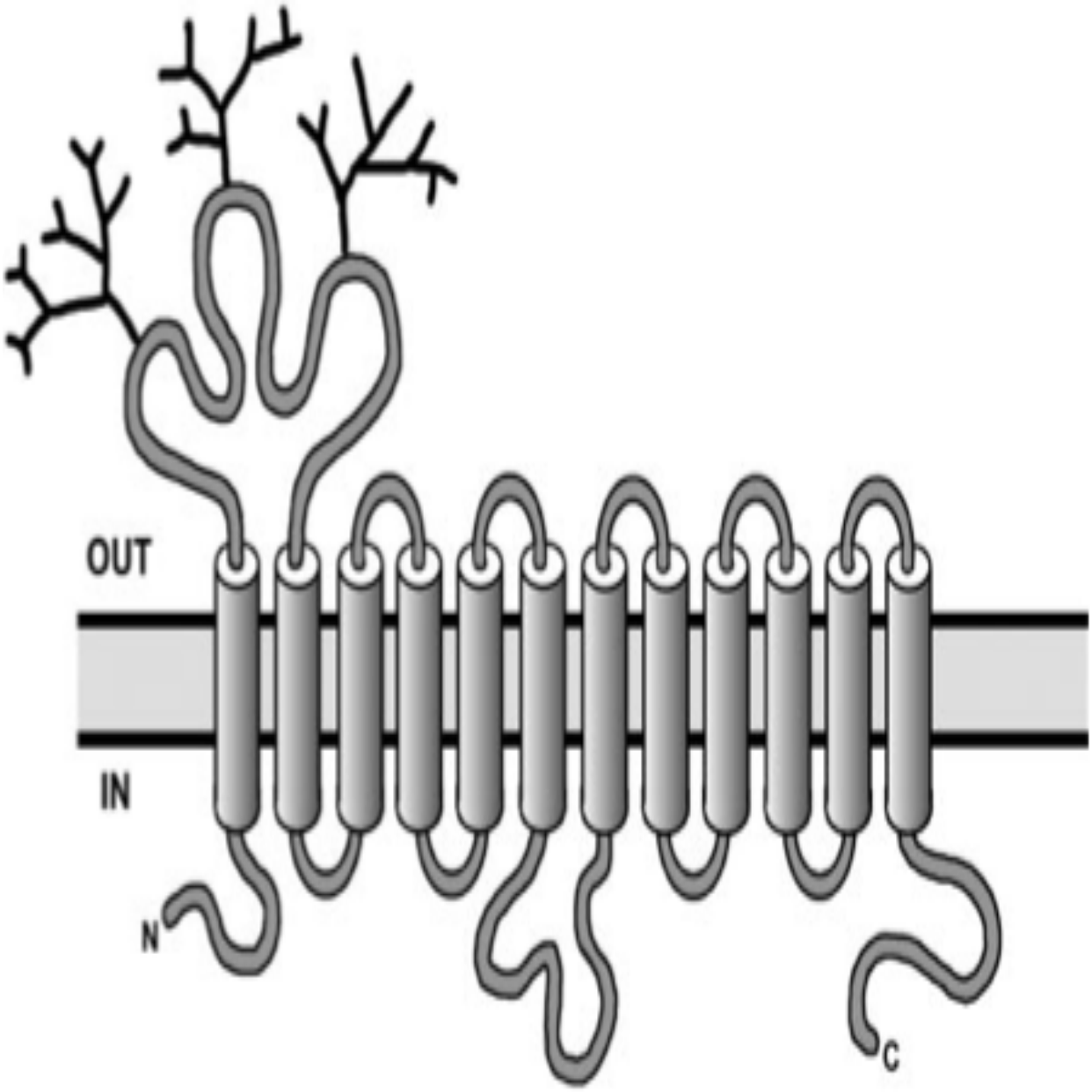

Figure 1.1 Predicted secondary structure of SLC22 transporters [6].

Since the identification and characterization of the first member of the family in 1994, other family members were cloned from species including human, mouse, and rat [1]. Three major OCT subtypes (OCT1, OCT2, and OCT3) have been identified; they share structural as well as substrate similarities. On the amino acid level, organic cation transporter subtypes from rat, mouse, and human exhibit cross-species identities of 78-95% (OCT1), 81-91% (OCT2), and 87-93% (OCT3); within one species (rat, mouse, or human), the amino acid identities between different subtypes are 67-70% between OCT1 and OCT2, 47-57% between OCT1 and OCT3, and 49-51% between OCT2 and OCT3 [7]. Recently, focus has been turned to investigate the function of transporters in different organs, regulation of transporter expression, biochemical implications of the transporters, and to understand the transport mechanisms.

Cloned from rat (r) liver in 1994, rOct1 (Slc22a1) was the first member of the SLC22 family to be identified, and was later cloned from human, mouse and rabbit [1, 8]. OCT1 is mainly expressed in liver where it is located in the sinusoidal membrane of hepatocytes; strong expression is also found in kidney in rodents (rat and mouse) and rabbits, while only small amounts of SLC22A1 mRNA were detected in human kidney. Human OCT1 is expressed in various additional organs including small intestine, lung, heart, skeletal muscle, brain, placenta, mammary gland, adrenal gland, eye, adipose tissue, immune cells, and various tumors [5]. OCT1 has broad substrate specificity. Most substrates of human OCT1 are monovalent organic cations including model cations such as tetraethylammonium (TEA^+), 1-methyl-4-phenylpyridinium (MPP^+), 4-[4-(dimthylamino)-styryl]-N-methylpyridinium (ASP), and 4',6-diamidino-2-phenylindol (DAPI); endogenous compounds including salsolinol, polyamine putrescine; and

therapeutics such as the antidiabetic drug metformin, antiviral drugs, antiparasitic drugs, and so on [5]. OCT1 mediates the uptake of substrates across the sinusoidal membrane into hepatocytes, which is the first step in hepatic excretion of many substances; and the transporter also facilitates passage of endogenous substrates and drugs across the blood-brain barrier (BBB). Inter-individual differences in expression of OCT1, which may be influenced by genetic and epigenetic factors, cause differences in hepatic excretion and tissue distribution of drugs such as metformin. To date, at least 23 coding single nucleotide polymorphisms (cSNPs) have been identified for human OCT1 [9]. Three of these SNPs (Arg61Cys, Cys88Arg, and Gly401Ser) resulted in decreased uptake of MPP^+, indicating that they might be involved with hOCT1-MPP^+ interaction [10]. Twelve of these SNPs have been shown to affect functionality of hOCT1 towards metformin by *in vitro* and *in vivo* data, thus these SNPs might be responsible for the variability observed in patients (Table 1.1) [11, 12].

Table 1.1 Summary of OCTs non-synonymous SNPs associated with metformin disposition.

			Functional Effect		
	dbSNP ID	Mutation	In vitro	In vivo	References
SLC22A1 (OCT1)	rs34447885	Ser14Phe	Reduced V_{max}		[11, 13]
	rs72552761	Gln18His			
	rs34570655	Leu23Val			
	rs35888596	Gly38Asp			
	rs2297373	Phe41Leu			
	rs12208357	Arg61Cys	Reduced uptake	Increased AUC & C_{max} Decreased V_d	[10, 11, 13]
	rs35546288	Leu85Phe	Similar function		[13]
	rs55918055	Cys88Arg	Reduced uptake		[10]
	rs683369	Leu160Phe	Similar function	Reduced diabetes risk in metformin-treated patients	[10, 11, 13]
	rs34104736	Ser189Leu	Reduced V_{max}		[11, 13]
	rs36103319	Gly220Val	Reduced uptake		[11, 13]

dbSNP ID	Mutation	In vitro	In vivo	References
rs4646277	Pro283Leu	Reduced uptake		[14]
rs4646278	Arg287Gly	Reduced uptake		[14]
rs2282143	Pro341Leu	Similar function	No impact	[11, 13, 15]
rs34205214	Arg342His	Similar function		[11, 13]
rs34130495	Gly401Ser	Reduced V_{max} Increased K_m	Increased glucose half-life following metformin treatment	[10, 11, 13]
rs628031	Met408Val	Similar function	Positive predictor for efficacy of metformin	[11, 13, 15]
rs72552762	Gly414Ala			
rs202220802	Met420del	Reduced V_{max} Increased K_m	Increased glucose half-life following metformin treatment	[10, 11, 13]
rs35956182	Met440Ile			
rs34295611	Val461Ile	Similar function		[13]
rs34059508	Gly465Arg	Reduced uptake	Increased glucose half-life following metformin treatment	[11, 13]

	dbSNP ID	Mutation	In vitro	In vivo	References
	rs35270274	Arg488Met	Similar function		[11, 13]
SLC22A2 (OCT2)	rs72552765	Phe45Leu			
	rs8177505	Phe45Ile			
	rs8177504	Pro54Ser	Similar function		[16]
	rs8177509	Phe161Leu	Similar function		[16]
	rs8177507	Met165Ile	Reduced V_{max}		[17]
	rs8177508	Met165Val	Similar function		[16]
	rs57371881	Arg176His			
	rs201919874	Thr199Ile	Reduced V_{max}	Increased C_{max} and AUC	[18, 19]
	rs145450955	Thr201Met	Reduced V_{max}	Increased C_{max} and AUC	[18, 19]
	rs316019	Als270Ser	Reduced V_{max}	Increased C_{max} and AUC	[17-19]
	rs8177513	Ala297Gly	Similar function		[16]
	rs45599131	Leu351Trp			
	rs8177516	Arg400Cys	Reduced V_{max}		[17]
	rs8177517	Lys432Gln	Increased K_m		[17]

	dbSNP ID	Mutation	In vitro	In vivo	References
	rs3907239	Arg463Lys			
	rs17853948	Val502Gly			
	rs17853948	Val502Glu			
SLC22A3 (OCT3)	rs8187715	Thr44Met	Increased V_{max}		[20]
	rs8187717	Ala116Ser	Similar function		[20]
	-	Met370Ile	Reduced V_{max}		[21]
	rs8187725	Thr400Ile	Increased K_m Reduced V_{max}		[20]
	-	Val423Phe	Increased K_m Reduced V_{max}		[20]
	rs12212246	Ala439Val			[22]
	rs9365165	Gly475Ser			[22]

rOct2 (Slc22a2) was cloned from rat kidney in 1996, and was later cloned in human, mouse, rabbit, and pig [1, 23]. Human OCT2 is mainly localized to the basolateral membrane of renal proximal tubules in the kidney; OCT2 is also expressed in small intestine, lung, placenta, brain, thymus, and inner ear [5]. Human OCT2 transports model cations including TEA^+, MPP^+, ASP, N-methylnicotinamide, aminoguanidine; neurotransmitters such as dopamine (DA), epinephrine, norepinephrine (NE), serotonin (5-HT), histamine; and drugs including memantine, oxaliplatin, cimetidine, and metformin. OCT2 mediates the first step in renal excretion of many drugs; it also facilitates the passage of drugs across the BBB (as efflux transporter) and participates in the regulation of intracellular concentrations of neurotransmitters [5]. The efficacy of cationic drugs that are OCT2 substrates and are mainly excreted by the kidney can be improved by comedication of other OCT2 substrates; down-regulated expression of OCT2 may lead to changes in pharmacokinetics and possible nephrotoxicity of OCT2 substrates [5]. Larger, and ethnically more diverse studies on OCT2 have revealed at least 10 cSNPs that altered transporter-substrate interactions [17]. Several functional studies of these polymorphisms have been conducted, and *in vivo* and *in vitro* changes in metformin disposition were observed (Table 1.1) [24].

hOCT3 (SLC22A3) and rOct3 (Slc22a3) were cloned in 1998 from human central nervous system and rat placenta, respectively, and was later cloned from mouse kidney [25-27]. The distribution of OCT3 is broad compared to OCT1 and OCT2; it is expressed in heart, skeletal muscle, brain, small intestine, liver, lung, kidney, urinary bladder, mammary gland, cornea, skin, blood vessels, and tumor cells [5]. In the CNS,

OCT3 has been detected in neurons, glial cells and epithelial cells of the choroid plexus [1, 22, 28, 29]. It is targeted to basolateral membranes of placental epithelium, to the sinusoidal membrane of hepatocytes, and to the luminal membrane of bronchial epithelial cells [1, 22, 28, 29]. Typical model cations for OCTs, neurotransmitters, and drugs such as metformin, are transported by OCT3. OCT3 is involved in the uptake of organic cations into brain, heart, and liver; it also participates in biliary excretion of organic cations, and changes neuronal activities and behavior by regulating neurotransmitter concentrations in the CNS [30]. OCT3 has been suggested to be related with coronary heart disease, prostate cancer, and obsessive-compulsive disorder in children [21, 31, 32]. Inhibitors of OCT3 may be employed to suppress cardiotoxicity of drugs that are OCT3 substrates [5]. At least seven SNPs were detected for human OCT3; however, evidence for functional consequences on metformin disposition is limited (Table 1.1) [9].

1.2 Organic Cation Transporter-Mediated Drug Interaction and Importance

OCTs play a pivotal role in the absorption, tissue distribution, and excretion of a diverse array of substances, including drugs, toxins, environmental pollutants (xenobiotics), neurotransmitters and metabolic waste products [1]. hOCT1, hOCT2 and hOCT3 exhibit overlapping substrate specificities and are able to transport a large variety of organic cations (i.e., weak bases that are positively charged at physiological pH), and some non-charged compounds. Hundreds of important therapeutics have been identified as substrates and/or inhibitors of OCTs so far [1]. *In vivo* studies have

shown that genetic variations in OCT1 are associated with alterations in metformin pharmacokinetics (PK) and co-administration of cimetidine (hOCT inhibitor) decreased metformin renal clearance [11]. Based on the fact that hOCT3 is expressed on the basolateral membrane in hepatocytes, and that liver is a major organ for drug elimination (first pass effect), hOCT3 is also vital for affecting drug bioavailability, supported by a recent study showing that OCT3 plays an important role in the absorption and elimination of metformin [33]. Recently, hOCTs, especially hOCT2 and hOCT3 have been detected in the central nervous system, and speculated to be part of the extraneuronal monoamine transport system (uptake-2 system), responsible for the peripheral reuptake of monoamine neurotransmitters such as serotonin and norepinephrine [26, 34]. Changes in the level of neurotransmitters in the CNS is thought to be the reason for several neurological diseases including depression [35]. So, identifying hOCTs as new targets for treating these diseases is of importance and might offer breakthroughs in treatment since traditional antidepressant drugs targeting the uptake-1 system (e.g., serotonin transporter) are associated with either no response or side effects for a large number of patients [36].

As these transporters have an impact on the pharmacokinetics (e.g., AUC, clearance and tissue distribution) of a broad variety of therapeutics, pharmacodynamic (PD) response might be altered due to concomitant administration of substrates or inhibitors of the same transporter. This is called drug-drug interaction (DDI), which might lead to unexpected side effects to patients. For instance, the glucose-lowering effect of metformin is decreased due to the co-administration of verapamil (hOCT1 inhibitor) [37]. Therefore, the United States Food and Drug Administration (FDA) and the European

Medicines Agency (EMA) have issued guidance documents regarding circumstances under which drug interactions with specified transporters need to be investigated for drug safety and efficacy [38, 39]. Specifically, investigated drugs should be evaluated in vitro to determine whether they are substrates of OCT2 when renal active secretion is important [38].

OCT substrates exhibit a wide variety of structural and physiochemical properties and currently the nature of the biochemical interactions between substrate and transporter are unknown. Polymorphisms that change the expression level, regulation, turnover, and/or substrate affinity of these transporters can potentially influence therapeutic efficacy and may cause toxic side effects of individual drugs [1]. Understanding the mechanism of substrate-transporter interaction and finding critical residues for that interaction may provide information for developing strategies for treating transporter related DDIs. In order to obtain a deeper understanding of drug transport through hOCTs and for designing drugs with optimized biodistribution, excretion and controlled drug-drug interactions, it is important to elucidate the structure of the substrate binding region, and through what mechanisms various substrates bind to the region [40]. In the end, these questions can only be solved by the crystallization of ligand-transporter complexes; however, no transporter of the SLC22 family been successfully crystallized. Therefore, identifying which amino acid residues are critical for transporter-substrate interactions though homology modeling is currently of central importance.

1.3 Current Perspectives of Homology Modeling

New proteins important in biological pathways/processes are routinely discovered, and one of the major goals of structural biology involves formation of protein-ligand complexes, in which the protein molecules act energetically in the course of binding [41]. Understanding the structures of proteins is also essential for understanding the effects of disease mutations, for designing experiments to probe the mechanisms of substrate binding, and for guiding *in silico* drug design [42]. However, determining the structures of SLC22 transporters has proven difficult either through X-ray crystallography, NMR spectroscopy, or electron microscopy due to their partially hydrophobic surfaces, flexibility, lack of stability, and inability to produce a large amount of pure protein [43]. In the absence of experimental data, model building on the basis of a known 3-dimensional structure of a homologous protein is at present the best available method to obtain structural information [41].

Homology modeling uses the fact that two evolutionarily related protein sequences have similar structures [44]. Thus, utilizing the known crystal structure (experimentally solved) of a protein as a template can help mimic the structure of a closely related protein whose structure is unknown. Currently, 83,546 experimental protein structures are available in Protein Data Bank (PDB) [45], and even though the number of solved crystal structures is steadily increasing, the rate is still far slower than the growth of newly discovered proteins [43]. Utilizing homology modeling is helping scientists bridge the gap between sequence and structure space with knowledge we possess [46]. Homology modeling provides knowledge for both medical and biological aspects, such as hypotheses about drug design, ligand binding site, substrate

specificity, molecular etiology of genetically transmitted disease related to SNPs, starting models for X-ray crystallography, and function annotation [41].

Homology modeling provides insights for structure of the target protein, the quality of which depends on the sequence similarity to the template [47]. Models of target proteins built on templates with more than 50% sequence similarities are accurate for drug discovery purposes, mutagenesis experiments can be guided based on models with 25 to 50% similarities to templates, and similarities between 10 to 25% are tentative [48-50]. Building a homology model is a multi-step process, which can be summarized as follows: (1) identification of template; (2) sequence alignment; (3) model building; (4) model refinement, and (5) model validation [51].

Utilizing programs to compare the amino acid sequence of the query protein with sequences of proteins stored in PDB (structures solved) is the first step to identify a suitable template. The most frequently used server is BLAST (Basic Local Alignment Search Tool, NCBI) [52]. The sequences of the query protein and the chosen template are aligned to overlay the evolutionarily related blocks of the two proteins; this procedure is usually conducted with program ClustalX [53]. Possible error in alignment is the main source of deviation in homology modeling even when the correct template was used [41]. Once an alignment is built between the query and template, the template structure is used to guide the construction of a theoretical structure for the target protein. This model building entails two parts: first, for the portion of sequences aligned, the program only needs to adjust side-chain atoms of the template structure based on the amino acids of the target; second, for parts that are not aligned, either deletion or insertion will be performed. Generally rigid-body assembly, spatial restraint, segment

matching, and artificial evolution are used for model building [41]. The most widely used software to generate homology models is MODELLER (University of California at San Francisco, San Francisco, CA) [54]. After refining and validating the model with numerous scoring functions, information from a successfully generated model (after validation) could be used to guide other studies and experiments. The challenge in generating homology models for membrane transporters concerns utilizing templates with low sequence identity and/or similarity, and the divergent membrane topologies of transporters [55]. A list of crystal structure templates (identified through running alignment and choosing transporters with the highest sequence identities) recommended by the International Transporter Consortium to use for homology model generation for SLC transporters is shown below in Table 1.2 [56].

Table 1.2 Recommended templates for homology modeling on SLC transporters [56].

Family	Template
SLC7	Amino acid antiporter AdiC
SLC10	Apical sodium-dependent bile acid transporter $ASBT_{NM}$
SLC15	Peptide transporter $PepT_{SO}$
SLC22	High-affinity phosphate importer PiPT
SLC28	Concentrative nucleoside transporter vcCNT
SLC47	Multidrug and toxic compound extrusion transporter NorM

Over the past two decades, researchers have been conducting experiments to determine the structure and mechanisms of action for organic cation transporters. In the earlier days, transmembrane domains and secondary structures of OCTs were predicted with hydropathy profiles. Prior to building 3-D models for these transporters, determination of which amino acids to look into (and could potentially be involved in ligand-transporter interactions) were based on either the properties and locations of amino acids or whether residues are conserved within certain transporter type(s) [57-59]. As a starting point of studying ligand-transporter (OCT) interactions, the Koepsell group first looked into residues that may be involved in cation transport in rOct1 in 1999 by mutating an acidic amino acid that is conserved in OCTs but not in OATs – Asp475 (presumably located in TMD 11) [57]. Changes in substrate transport property after residue substitution indicated that Asp475 might be a part of an interaction domain [57]. To look further into transporter-ligand interactions, the Koepsell group decided to identify amino acids of rOct2 that are responsible for the higher affinity towards corticosterone compared with the low affinity between rOct1 and corticosterone [58]. Through introducing polypeptide stretches of rOct2 into rOct1, exchanging amino acids between the two transporters, and measuring transport functions, amino acids that might be responsible for the high affinity of rOct2 to corticosterone were identified (Table 1.3) [58].

Due to the fact that 2-D topology models of OCTs could not provide visualization of the binding pocket, scientists began to generate three-dimensional models of OCTs with the help of several crystallized membrane transporters. From the year 2005, 3-D homology models of rOct1, rOct2, rbOct2 and hOCT2 have been reported in literature

using either lactose permease (LacY) from Escherichia coli (PDB ID: 1PV6) or glycerol-3-phosphate transporter (Glp-T) from Escherichia coli (PDB ID: 1PW4) as template [40, 60-62]. In 2005, Popp et al. looked into eighteen consecutive amino acids on the fourth TMD in rat Oct1 because this domain was hypothesized to contain amino acids on one side of the presumed α helix that are conserved within OCTs but not OATs. By introducing mutations to these residues and testing changes in TEA^+ and MPP^+ transport activity (substrate selectivity, affinity and turnover rates) in oocytes, three residues were identified as critical for TEA^+ and MPP^+ uptake [40]. Then they conducted homology modeling and generated an inward-open 3-D model for rOct1 using LacY as template, and claimed the localization of these residues inside the binding pocket [40].

In the same year, Zhang et al. conducted a study to identify amino acid residue(s) responsible for the difference in transport activity between rbOct1 and rbOct2 [61]. Three amino acids on the C-terminal half that are conserved in OCT1 orthologs but different in OCT2 were mutated, and one residue (Glu447) was identified as a contributor to binding properties of rbOct2 [61]. Zhang et al. then built an inward-open 3-D homology model of rbOct2 based on the crystal structure of Glp-T and confirmed that Glu447 faces and lie within the putative cleft region [61, 63].

Following their previous work, the Zhang group further elucidated hOCT2 structure by examining the accessibility to hydrophilic thiol-reactive reagents [64]. Based on the homology model of rbOct2 built by Zhang et al. in a previous study, a 3-D homology model of human OCT2 (using GlpT as template) was generated [63, 64]. All cysteine residues in TMDs 10 and 11 were mutated and tested for transport activity changes (using TEA^+) as well as accessibilities to biotin [64]. Results showed only

Cys474 is exposed to the extracellular aqueous environment, and "participates in forming a transport pathway for TEA^+" [64]. Amino acid residues identified as critical for transporter-substrate interactions from 2-D topology modeling as well as 3-D homology modeling are summarized in Table 1.3.

Table 1.3. Critical residues identified through modeling studies.

Transporter	Model	Template	Critical Residue(s)	Reference
rOct1	2-D topology model	-	Asp475	[57]
rOct2	2-D topology model	-	Ile443, Tyr447, Glu448	[58]
rOct1	3-D homology model	LacY	Trp218, Tyr222, Thr226	[40]
rOct2	3-D homology model	LacY	Cys451	[65]
rbOct2	3-D homology model	GlpT	Glu447	[61]
hOCT2	3-D homology model	GlpT	Cys474	[64]

From these past studies, we noticed that even though a number of amino acid residues have been identified as related to substrate selectivity and affinity, and are supported by experimental data, utilization of information from 3-D models of OCT transporters was kept to a minimum. These models were only used as a validation tool to confirm that the residues are close to the binding pocket. One of our purposes of generating a 3-D homology model of hOCT3 is to provide guidance in mutagenesis experiments and mechanism analyses, not just as an indicator for the probable location of certain residues. The 3-D homology models of OCTs built in earlier studies, albeit 'accurate' at that time, are somehow out-of-date considering the low sequence identities (and low sequence similarities). What we need is to develop 3-D homology models for OCT3 with higher sequence identities/similarities, and utilize them to direct future site-directed mutagenesis studies of OCT-ligand interaction, transport mechanism, novel drug designs and other important purposes. Choosing eukaryotic inorganic phosphate transporter (PiPT) as the template to conduct homology modeling for OCT3 is superior compared to the old templates (LacY and GlpT) because of its higher sequence similarity towards the target transporter (~40%), increasing the confidence of using the generated 3-D model to guide mutagenesis studies; crystal structures of LacY and GlpT are both inwardly oriented, whereas PiPT is crystallized in an occluded state that provides the most interactions between docking ligand and binding pocket; presence of a large intracellular loop between TMDs 6 and 7 in PiPT makes its structure more similar to that of an OCT, compared to the structures of LacY and GlpT that do not contain any large loop; moreover, LacY and GlpT belong to prokaryotic organisms while PiPT belongs to eukaryotic organisms, which makes PiPT closer to OCTs in an

evolutionary point of view. Based on these points and the fact that PiPT is recommended by the International Transporter Consortium, we decided to generate a 3-D homology model of hOCT3 using PiPT as the template [56].

1.4 Species Differences for Organic Cation Transporter 3

OCT3 orthologs from human, rat, and mouse share a great deal of similarities including protein sequence, tissue distribution, operating mechanism, substrates, and so on; these similarities might be explained by the high sequence identity and similarity between the orthologs (with 87% between human and mouse OCT3 and 86% between human and rat OCT3, as shown in Figure 1.2 and Figure 1.3, respectively). Despite these similarities, inter-species differences are also observed. Rodent Oct3s are detected in some tissues where human OCT3 is not expressed (large intestine, spleen, thymus, etc.), and interacting characteristics for some molecules with OCT3 orthologs could be quite diverse (as shown in Table 1.4), which could be used to distinguish OCT3 from different species [1].

Even though the differences between transporter sequences are trivial, they could lead to diverse conformations of the transporters expressed in cell membranes, which might be the cause of different transporter-ligand interacting profiles.

Table 1.4 Substrate* and inhibitor affinities (in μM) for different OCT3 orthologs.

Molecule	hOCT3	mOct3	rOct3	Reference
Corticosterone	0.12		4.9	[26, 66]
Dopamine	1200		384,620	[26, 67, 68]
Estradiol	2.9		1.1	[66, 69]
Norepinephrine	2630*		432	[26, 70]
o-Methylisoprenaline	4.4	1.4		[69, 71]
Serotonin	1000		970	[26, 70]
Cimetidine	17	1.3		[72]
Procainamide	738	11		[27, 73]
Quinine	37	3.0		[29, 73]

Score	Expect	Method	Identities	Positives	Gaps
974 bits(2518)	0.0	Compositional matrix adjust.	481/556(87%)	509/556(91%)	5/556(0%)

```
Query  1    MPSFDEALQRVGEFGRFQRRVFLLLCLTGVTFAFLFVGVVFLGTQPDHYWCRGPSAAALA  60
            MP+FD+AL++ GEFGRFQRRVFLLLCLTGVTFAFLFVGVVFLG+QPD+YWCRGP A ALA
Sbjct  1    MPTFDQALRKAGEFGRFQRRVFLLLCLTGVTFAFLFVGVVFLGSQPDYYWCRGPRATALA  60

Query  61   ERCGWSPEEEWNRTAPASRGPEPPERRGRCQRYLLEAANDSASATSALSCADPLAAFPNR  120
            ERC WSPEEEWN T P    P     +G C RYLLEA N S    S LSC DPL AFPNR
Sbjct  61   ERCAWSPEEEWNLTTPELHVPAERRGQGHCHRYLLEATNTS----SELSC-DPLTAFPNR  115

Query  121  SAPLVPCRGGWRYAQAHSTIVSEFDLVCVNAWMLDLTQAILNLGFLTGAFTLGYAADRYG  180
            SAPLV C G WRY + HSTIVS+FDLVC NAWMLDLTQAILNLGFL GAFTLGYAADRYG
Sbjct  116  SAPLVSCSGDWRYVETHSTIVSQFDLVCSNAWMLDLTQAILNLGFLAGAFTLGYAADRYG  175

Query  181  RIVIYLLSCLGVGVTGVVVAFAPNFPVFVIFRFLQGVFGKGTWMTCYVIVTEIVGSKQRR  240
            R++IYL+SC GVG+TGVVVAFAPNF VFVIFRFLQGVFGKG WMTC+VIVTEIVGSKQRR
Sbjct  176  RLIIYLISCFGVGITGVVVAFAPNFSVFVIFRFLQGVFGKGAWMTCFVIVTEIVGSKQRR  235

Query  241  IVGIVIQMFFTLGIIILPGIAYFIPNWQGIQLAITLPSFLFLLYYWVVPESPRWLITRKK  300
            IVGIVIQMFFTLGIIILPGIAYF P+WQGIQLAI+LPSFLFLLYYWVVPESPRWLITRK+
Sbjct  236  IVGIVIQMFFTLGIIILPGIAYFTPSWQGIQLAISLPSFLFLLYYWVVPESPRWLITRKQ  295

Query  301  GDKALQILRRIAKCNGKYLSSNYSEITVTDEEVSNPSFLDLVRTPQMRKCTLILMFAWFT  360
            G+KALQILRR+AKCNGK+LSSNYSEITVTDEEVSNPS LDLVRTPQMRKCTLILMFAWFT
Sbjct  296  GEKALQILRRVAKCNGKHLSSNYSEITVTDEEVSNPSCLDLVRTPQMRKCTLILMFAWFT  355

Query  361  SAVVYQGLVMRLGIIGGNLYIDFFISGVVELPGALLILLTIERLGRRLPFAASNIVAGVA  420
            SAVVYQGLVMRLG+IGGNLYIDFFISG+VELPGALLILLTIERLGRRLPFAASNIVAGV+
Sbjct  356  SAVVYQGLVMRLGLIGGNLYIDFFISGLVELPGALLILLTIERLGRRLPFAASNIVAGVS  415

Query  421  CLVTAFLPEGIAWLRTTVATLGRLGITMAFEIVYLVNSELYPTTLRNFGVSLCSGLCDFG  480
            CLVTAFLPEGI WLRTTVATLGRLGITMAFEIVYLVNSELYPTTLRNFGVSLCSGLCDFG
Sbjct  416  CLVTAFLPEGIPWLRTTVATLGRLGITMAFEIVYLVNSELYPTTLRNFGVSLCSGLCDFG  475

Query  481  GIIAPFLLFRLAAVWLELPLIIFGILASICGGLVMLLPETKGIALPETVDDVEKLGSPHS  540
            GIIAPFLLFRLAA+WLELPLIIFGILAS+CGGLVMLLPETKGIALPETV+DVEKLGS
Sbjct  476  GIIAPFLLFRLAAIWLELPLIIFGILASVCGGLVMLLPETKGIALPETVEDVEKLGSSQL  535

Query  541  CKCGRNKKTPVSRSHL  556
             +CGR KKT VS S +
Sbjct  536  HQCGRKKKTQVSTSDV  551
```

Figure 1.2 Sequence alignment between human and mouse OCT3.

Query sequence represents human OCT3 and subject sequence represents mouse Oct3.

Score	Expect	Method	Identities	Positives	Gaps
972 bits(2514)	0.0	Compositional matrix adjust.	480/556(86%)	511/556(91%)	5/556(0%)

```
Query  1    MPSFDEALQRVGEFGRFQRRVFLLLCLTGVTFAFLFVGVVFLGTQPDHYWCRGPSAAALA  60
            MP+FD+AL++ GEFGRFQRRVFLLLCLTGVTFAFLFVGVVFLG+QPD+YWCRGP A ALA
Sbjct  1    MPTFDQALRKAGEFGRFQRRVFLLLCLTGVTFAFLFVGVVFLGSQPDYYWCRGPRATALA  60

Query  61   ERCGWSPEEEWNRTAPASRGPEPPERRGRCQRYLLEAANDSASATSALSCADPLAAFPNR  120
            ERC WSPEEEWN T P    P     +G C RYLLE  N S    S LSC DPLAAFPNR
Sbjct  61   ERCAWSPEEEWNLTTPELHVPAERRGQGHCHRYLLEDTNTS----SELSC-DPLAAFPNR  115

Query  121  SAPLVPCRGGWRYAQAHSTIVSEFDLVCVNAWMLDLTQAILNLGFLTGAFTLGYAADRYG  180
            SAPLVPC G WRY + HSTIVS+FDLVC NAWMLDLTQAILNLGFL GAFTLGYAADRYG
Sbjct  116  SAPLVPCSGDWRYVETHSTIVSQFDLVCGNAWMLDLTQAILNLGFLAGAFTLGYAADRYG  175

Query  181  RIVIYLLSCLGVGVTGVVVAFAPNFPVFVIFRFLQGVFGKGTWMTCYVIVTEIVGSKQRR  240
            R+++YL+SC GVG+TGVVVAFAPNF VFVIFRFLQGVFGKG WMTC+VIVTEIVGSKQRR
Sbjct  176  RLIVYLISCFGVGITGVVVAFAPNFSVFVIFRFLQGVFGKGAWMTCFVIVTEIVGSKQRR  235

Query  241  IVGIVIQMFFTLGIIILPGIAYFIPNWQGIQLAITLPSFLFLLYYWVVPESPRWLITRKK  300
            IVGIVIQMFFTLGIIILPGIAYF P+WQGIQLAI+LPSFLFLLYYWVVPESPRWLITRK+
Sbjct  236  IVGIVIQMFFTLGIIILPGIAYFTPSWQGIQLAISLPSFLFLLYYWVVPESPRWLITRKQ  295

Query  301  GDKALQILRRIAKCNGKYLSSNYSEITVTDEEVSNPSFLDLVRTPQMRKCTLILMFAWFT  360
            G+KALQILRR+AKCNGK+LSSNYSEITVTDEEVSNPS LDLVRTPQMRKCTLILMFAWFT
Sbjct  296  GEKALQILRRVAKCNGKHLSSNYSEITVTDEEVSNPSCLDLVRTPQMRKCTLILMFAWFT  355

Query  361  SAVVYQGLVMRLGIIGGNLYIDFFISGVVELPGALLILLTIERLGRRLPFAASNIVAGVA  420
            SAVVYQGLVMRLG+IGGNLY+DFFISG+VELPGALLILLTIERLGRRLPFAASNIVAGV+
Sbjct  356  SAVVYQGLVMRLGLIGGNLYMDFFISGLVELPGALLILLTIERLGRRLPFAASNIVAGVS  415

Query  421  CLVTAFLPEGIAWLRTTVATLGRLGITMAFEIVYLVNSELYPTTLRNFGVSLCSGLCDFG  480
            CLVTAFLPEGI WLRTTVATLGRLGITMAFEIVYLVNSELYPTTLRNFGVSLCSGLCDFG
Sbjct  416  CLVTAFLPEGIPWLRTTVATLGRLGITMAFEIVYLVNSELYPTTLRNFGVSLCSGLCDFG  475

Query  481  GIIAPFLLFRLAAVWLELPLIIFGILASICGGLVMLLPETKGIALPETVDDVEKLGSPHS  540
            GIIAPFLLFRLAA+WLELPLIIFGILAS+CGGLVMLLPETKGIALPETV+DVEKLGS
Sbjct  476  GIIAPFLLFRLAAIWLELPLIIFGILASVCGGLVMLLPETKGIALPETVEDVEKLGSSQL  535

Query  541  CKCGRNKKTPVSRSHL  556
             +CGR KKT VS S++
Sbjct  536  HQCGRKKKTQVSTSNV  551
```

Figure 1.3 Sequence alignment between human and rat OCT3.

Query sequence represents human OCT3 and subject sequence represents rat Oct3.

1.5 Organic Cation Transporter-Mediated Neurotransmitter Disposition in Brain

Depressive disorders are among the most serious and burdensome psychiatric illnesses in the world, costing billions of dollars each year in US alone [74]. Previous studies have proved that neurotransmitter levels are low in depressive disorder patients. Current treatment is focusing on maintaining monoamine neurotransmitter (serotonin and/or norepinephrine) levels in synaptic clefts by inhibiting high affinity, low capacity monoamine uptake-1 transporters (e.g., serotonin transporter (SERT), norepinephrine transporter (NET), dopamine transporter (DAT), Figure 1.4) with serotonin transporter reuptake inhibitors (SSRIs, e.g., fluoxetine) and serotonin and norepinephrine transporter reuptake inhibitors (SNRIs, e.g., venlafaxine). However, this approach could end up with undesirable side effects, delayed onset of action, and poor response to the treatment [75, 76]. There are currently no new strategies for diagnosing or treating depressive disorders, so scientists are focusing on the low affinity, high capacity (uptake-2) clearance pathway for biogenic amines – the backup system for monoamine neurotransmitter clearance. Increasing evidence has indicated that organic cation transporters, which are widely expressed in the CNS (human OCT expression summarized in Table 1.5), interact not only with catecholamine (a kind of monoamine related to depressive disorders), but also with DA, 5-HT and NE and likely play a role in the regulation of neurotransmitter homeostasis, indicating that OCTs, especially OCT2 and OCT3, could be the major components of uptake-2 system (Figure 1.4) [34, 76]. Studies using inhibitors and knockout mice have been conducted to explore the role of OCTs in depression. Feng et al. noticed a dose-dependent increase in 5-HT level when administering decynium-22 (D-22, an OCT inhibitor), suggesting that OCTs might be

important in adaptive neurophysiological and behavioral response regulations [77]. Oct3 mRNA level as well as protein expression in SERT knockout mice were significantly increased in hippocampus when D-22 was given to SERT knockout mice; antidepressant-like effects were also observed, while mOct1 mRNA level remained unchanged [30, 78]. In another study, infusing antisense mouse Oct3 oligonucleotides to mice ventricle resulted in decreased expression of Oct3 and correlated antidepressant-like effects such as decreased immobility during forced swim test, and so on. [79]. These data suggest that OCT3 might be a compensatory mechanism for dysfunctional 5-HT clearance, an important determinant of CNS monoamine neurotransmitter balance, and a novel target for depressive disorder therapy.

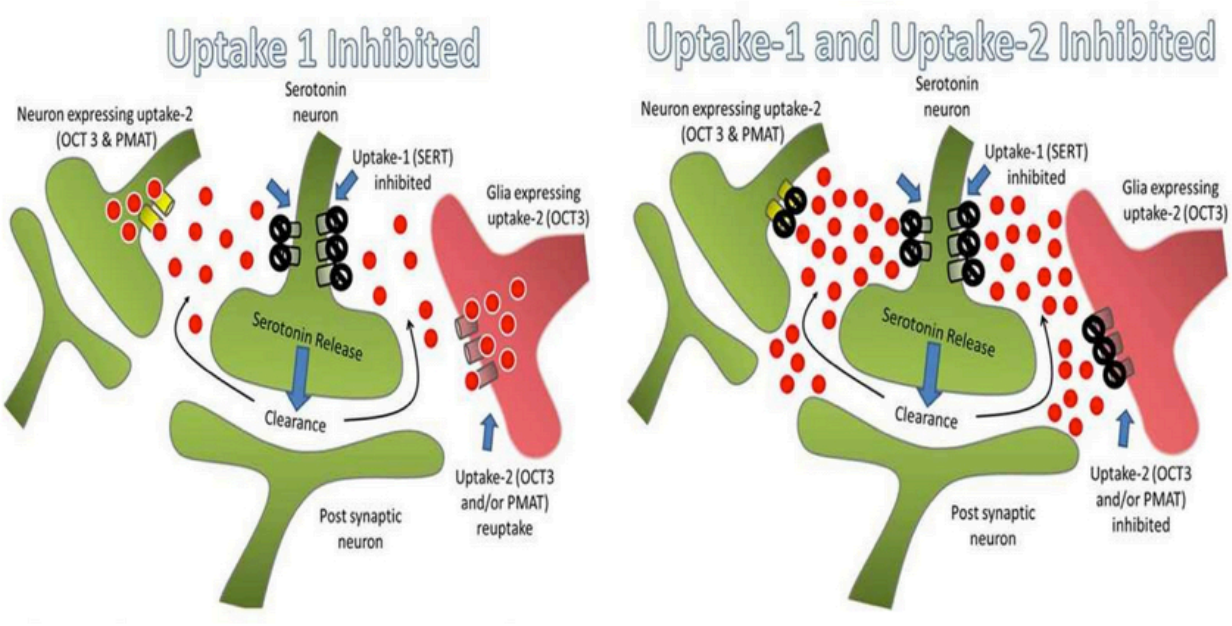

Figure 1.4 Inhibition of monoamine neurotransmitter pathway(s) in treating depressive disorders [76].

Table 1.5 Expression of OCTs in human brain.

Tissue	Transporter	Level	Expression	Localization	Technique	References
Choroid Plexus	hOCT1	mRNA	+		RT-PCR	[80]
	hOCT2	mRNA	+		RT-PCR	[80]
	hOCT3	mRNA	+		RT-PCR	[80]
Brain Capillary	hOCT1	mRNA	+		RT-PCR	[81, 82]
		Protein	+	Luminal and abluminal side of BMECs	Confocal microscopy & western blot	[83]
	hOCT2	mRNA	+/-		RT-PCR	[81, 82]
		Protein	+	Luminal and abluminal side of BMECs	Confocal microscopy & western blot	[83]
	hOCT3	mRNA	+		RT-PCR	[81, 82]
		Protein	+		Confocal microscopy & Western blot	[82]
Neuron and Glia Cells	hOCT1	mRNA	-		Northern blot	[84]
	hOCT2	mRNA Protein	+	Neurons	Northern blot, in situ hybridization & Western blot	[84, 85]

Tissue	Transporter	Level	Expression	Localization	Technique	References
		Protein	+	Neurons	Immunohistochemistry	[86]
	hOCT3	mRNA Protein	+	Astrocytes	RT-PCR & immunohistochemistry	[85, 86]
Different Brain Regions	hOCT1	mRNA	-		Northern blot	[84]
	hOCT2	mRNA	+	Amygdaloideus nucleus	Northern blot	[84]
		mRNA	+	Caudatus nucleus	Northern blot	
		mRNA	+	Cerebral cortex	In situ hybridization	
		mRNA Protein	+	Hippocampus	Northern blot, in situ hybridization & Western blot	
		mRNA	+	Subthalamicus nucleus	Northern blot	
		mRNA	+	Substantia nigra	Northern blot	

Tissue	Transporter	Level	Expression	Localization	Technique	References
		mRNA	+	Thalamus	Northern blot	
	hOCT3	mRNA	+	Caudate nucleus	RT-PCR	[87]
		mRNA	+	Cerebellum	RT-PCR	
		mRNA	+	Cerebral cortex	RT-PCR	
		mRNA	+	Medulla oblongata	RT-PCR	
		mRNA	+	Nucleus accumbens	RT-PCR	
		mRNA	+	Hippocampus	RT-PCR	
		mRNA	+	Substantia nigra	RT-PCR	
		mRNA	+	Pons	RT-PCR	

+: indicates transporter expression
-: indicates no transporter expression detected

Chapter 2

Research Objectives and Specific Aims

2.1 Research Objectives

To identify and verify crucial amino acid residues for interactions at the substrate-binding pocket of hOCT3, which will support breakthroughs in understanding drug absorption, clinical drug-drug interaction, compound extraction, as well as inform rational drug design strategies for hOCT3 interacting drugs. Our hypothesis is that substitution of hOCT3 residues involved in transporter-substrate interactions, implicated through *in silico* molecular modeling and docking studies, will result in altered affinity (K_m) of the transporter to MPP^+. Further, comparing critical residues of human, mouse, and rat OCT3 orthologs may provide an explanation for species differences in transporter function.

2.2 Specific Aims To Address the above Hypotheses

2.2.1 To identify residues critical for transporter-substrate interactions using *in silico* 3-D homology modeling and substrate docking. A 3-D model of hOCT3 is required for predicting substrate binding site and critical residuals.

2.2.2 To test the hypothesis that the critical residues predicted in the model are involved in hOCT3 substrate recognition. The affinity of the transporter (K_m) for MPP^+ should be

altered upon substitution of the true critical residues.

2.2.3 To test the hypothesis that substrates structurally divergent from MPP^+ will have different/additional amino acids critical for hOCT3 interaction. Additional substrate docking, mutational and kinetic studies should be performed to further validate the model.

2.2.4 To test the hypothesis that inter-species transport differences among human, mouse and rat OCT3 orthologs result from differences in the architecture of their binding regions.

Chapter 3

IDENTIFICATION OF hOCT3 STRUCTURAL ELEMENTS IMPACTING TRANSPORTER-SUBSTRATE INTERACTIONS

3.1 Introduction

Organic cation transporters belong to the solute carrier 22 (SLC22) family and mediate the absorption, distribution, and elimination of a broad variety of endogenous and exogenous organic compounds [1, 88]. OCTs are widely expressed in many barrier organs, such as intestine, kidney, liver, and brain [1, 88]. In the intestine, OCT1 and OCT3 are targeted to the brush border membrane of enterocytes and mediate the entry of cationic compounds [1]. OCT1 and 3 are both expressed in the sinusoidal membrane of hepatocytes to mediate the first step of hepatic excretion of substrates [1]. OCT2 and 3 are expressed in the basolateral membrane of proximal tubule cells and govern the first step of renal excretion [1]. Hundreds of important clinical therapeutics as well as numerous endogenous compounds are known substrates and/or inhibitors of OCTs, including metabolites (e.g., creatnine), neurotransmitters (e.g., serotonin, norepinephrine), hormones (e.g., corticosterone), receptor antagonists (e.g., cimetidine), chemotherapeutics (e.g., cisplatin), antidiabetics (e.g., metformin), and so on [1].

Intensive attention has been paid to study the interactions between (as well as transport mechanism of) compounds with OCT1 and OCT2 because of the large

amount of transporter expression in liver and kidney of these two transporters, respectively. However, more and more groups are focusing on OCT3, which is the most widely expressed organic cation transporter (expressed in tissues including skeletal muscle, placenta, heart and many more) [1]. Knockout mouse models showed the importance of Oct3 in different tissues. Intravenous injection of the OCT substrate MPP^+ into Oct3 knockout mice resulted in significantly reduced drug levels in heart and fetus, suggesting a prominent role of mOct3 in the heart and feto-placental interface [89]. A similar conclusion was drawn from a study of samples from patients with heart disease, which suggested that hOCT3 is important for the disposition and action of cationic drugs in the myocardium [90]. A compensatory up regulation of Oct3 in the brain of mice that lack the neuronal serotonin transporter indicated that mOct3 could play a role in neurotransmitter uptake [30, 78]. A recent study has demonstrated the high expression level of OCT3 in adipose tissue, and its ability to regulate extraneuronal norepinephrine uptake [91]. In human, OCT3 has been suggested to be related with coronary heart disease, prostate cancer, and obsessive-compulsive disorder in children [21, 31, 32, 90]. These possible physiological roles of OCT3 as well as numerous studies about interactions between clinical therapeutics and OCT3 justifies the importance of this transporter and the need to study its working mechanism.

In order to understand hOCT3-substrate interactions, structure of the transporter is needed, however, no member of the SLC22 family has been successfully crystallized. Thus there is a need to generate a 3-D homology model of hOCT3 with a suitable template. So far, three-dimensional homology models of rOct1, rOct2, rabbit (rb) Oct2, and hOCT2 have been reported in literature [40, 60-62]. Even though *in vitro* studies

were conducted and identified several amino acid residues that might be critical in terms of substrate and/or inhibitor interactions with these transporters, the models these groups generated were based on templates sharing low sequence identities to OCT, no ligand has been docked to the binding pockets of these models, and they were only used to demonstrate the locations of identified residues, not as guidance to direct mutational studies.

In our study, we generated a 3-D homology model for hOCT3 using eukaryotic inorganic phosphate transporter (PiPT) as the template. Based on information of the predicted amino acid residues through homology modeling and docking, we further tested accuracy of the model by mutating the implicated amino acids to see if the residue substitution altered the affinity between substrate and transporter. After confirming the mutants with sequencing, mutant plasmids were introduced to mammalian cells through stable transfection, and finally changes in transporter-substrate interaction were quantified via saturation assays.

3.2 Materials and Methods

3.2.1 Materials

Tritiated 1-methyl-4-phenylpyridinium ([^{3}H]MPP$^+$) was purchased from PerkinElmer Life and Analytical Science (Waltham, MA), and unlabeled MPP$^+$ was obtained from Sigma-Aldrich (St. Louis, MO). QuikChange Lightning Site-Directed Mutagenesis Kit was purchased from Agilent Technologies (Santa Clara, CA). Lipofectamine® 2000 Transfection Reagent was purchased from ThermoFisher Scientific (Waltham, MA). QIAprep Spin Miniprep Kit and QIAprep Spin Midiprep Kit

were purchased from QIAGEN Inc. (Germantown, MD). GoTaq Green Master Mix was purchased from Promega (Madison, WI). Abcam Plasma Membrane Protein Extraction Kit (ab65400) was purchased from Abcam (Cambridge, MA). DYKDDDDK Tag (D6W5B) Rabbit mAb antibody, and Anti-rabbit IgG AP-linked antibody were purchased from Cell Signaling Technology (Beverly, MA). Na^+/K^+-ATPase α1 (N-15) antibody (sc-16041) was purchased from Santa Cruz Biotechnology (Dallas, TX).

3.2.2 Modeling and Docking

The three-dimensional homology model of hOCT3 was based on the crystal structure of a eukaryotic inorganic phosphate transporter (PiPT) [92]. PiPT belongs to the phosphate: H^+ symporter family of MFS, similar to the SLC22 family, PiPT also contains 12 TMDs and intracellular N and C termini, and a large intracellular loop between TMDs 6 and 7 [93]. The crystal structure of PiPT (PDB ID: 4J05) was solved in complex with its substrate, inorganic phosphate, by Pedersen et al. at a resolution of 2.9 Å in an occluded conformation [92]. The structure of PiPT is currently recommended as the best template for OCTs and OATs because it is a crystallized transporter sharing the most sequence similarity with the human solute carrier group at this time, it possesses similar structure compared with OCTs (previous OCT templates do not contain the large intracellular loop), it was crystallized in an occluded state (could provide more information for compound docking), and PiPT is more evolutionarily close to OCTs and OATs. Based on these factors, we chose to use PiPT as the template to generate a 3-D homology model for hOCT3 [56].

Sequence of hOCT3 was obtained from Universal Protein Resource database (UniProt, accession code: O75751), and the sequence of PiPT was downloaded from

PDB in a fasta file (4J05) [94, 95]. The template and target (hOCT3) sequences were aligned using ClustalX followed by manual adjustments based on the TMDs observed in PiPT structure and predicted for hOCT3 using ICM Browser (Molsoft LLC) and Phobius (Stockholm Bioinformatics Center), the result of alignment is shown in Figure 3.1 [53, 96, 97]. The extracellular loop of PiPT was not part of the crystallization, thus it was not contained in the sequence of the PDB file; the extracellular and intracellular loops between TMDs 1, 2 and 6, 7 of hOCT3 were truncated because no corresponding residues were modeled in the crystal structure of PiPT.

Next, 100 homology models of hOCT3 were generated based on the alignment result and the crystal structure of PiPT (downloaded from PDB) using the MODELLER software (University of California at San Francisco, San Francisco, CA) [54, 95]. A DOPE (discrete optimized protein energy) score was automatically calculated for each model, and it was used to evaluate the quality of a structure model as a whole. Stereochemical quality of a 3-D protein model was checked using the PROCHECK function, which produces a Ramanchandran plot that helps visualize energetically allowed regions, and analyzes the residue-by-residue geometry of a model. A model with more than 90% of amino acids located in the favorable regions of a Ramanchandran plot is generally considered as an acceptable model. The binding pocket of hOCT3 for a specific docking compound was identified using GOLD suite 5.4 by docking a compound into a 12-Å sphere surrounding residue Asp478 (critical residue identified in earlier studies) [57]. Docking was performed by first energy-minimizing the docking compound (substrates for hOCT3, including MPP^+, serotonin, metformin, tetrapentylammonium (TPA^+), and epinephrine, chemical structures shown in Figure 3.2)

using Tripos force field with Gasteiger-Hückel charges in SYBYL X, and then inserting the compound with 10 poses into the pre-defined sphere for each of the one hundred models using GOLD [95, 98]. GOLD's default scoring function was used to determine the best ligand binding mode (pose), then potentially important amino acid residues were identified by analyzing the structure within the binging pocket as well as binding interaction energies.

Figure 3.1 Sequence alignment between PiPT and hOCT3.

Asterisks (*) indicate residues that are the same between the template and the target; colons (:) represent residues that are highly conserved between the sequences; periods (.) represent residues that are weakly conserved between the sequences; and blanks indicate that the residues are different.

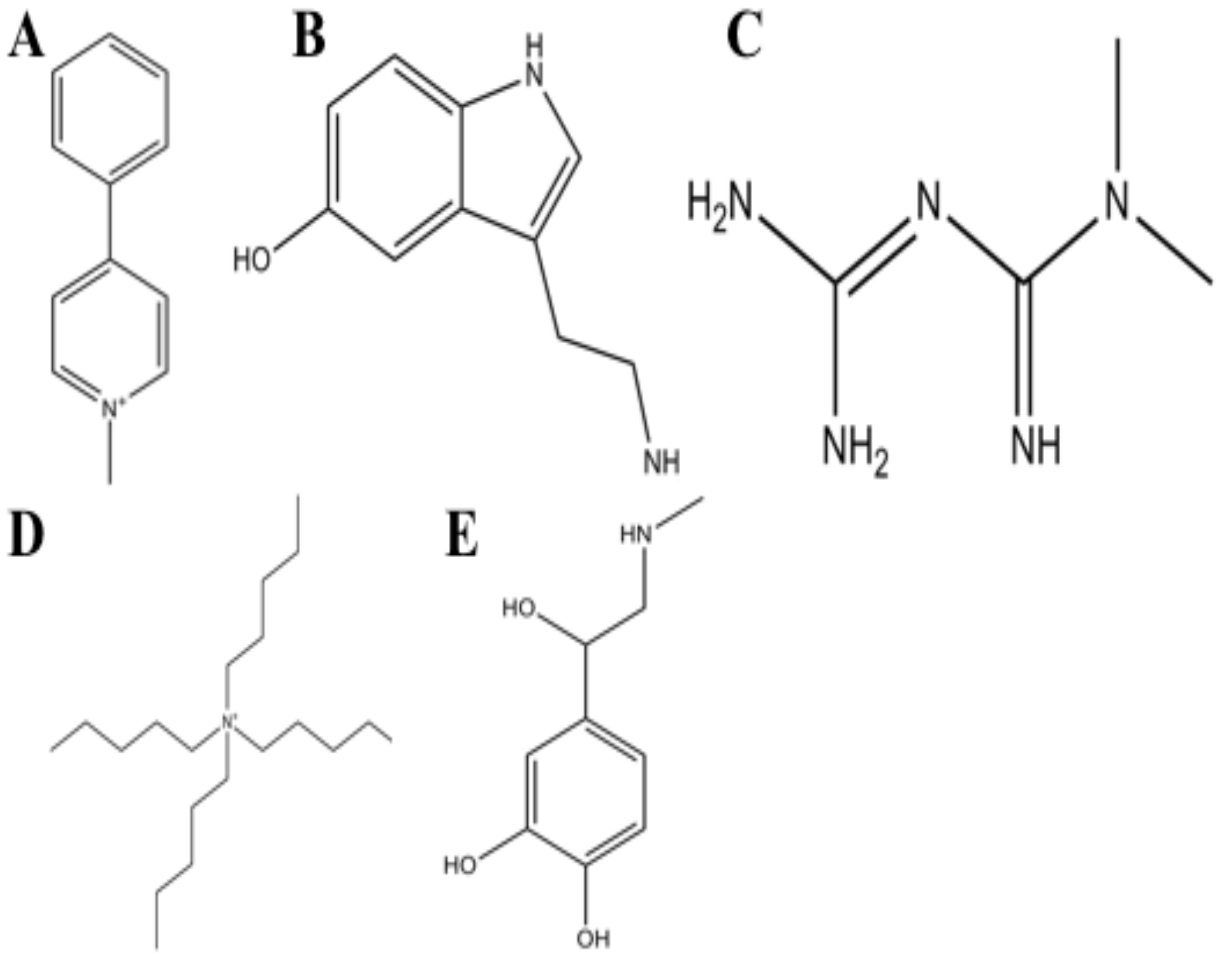

Figure 3.2 Structures of other docking compounds for hOCT3.

Structures of other docking compounds MPP^+ (A), serotonin (B), metformin (C), TPA^+ (D) and epinephrine (E) are displayed, respectively.

3.2.3 DNA Quantification

Concentration and purity of DNA samples were determined using GeneQuant Spectrophotometer.

3.2.4 Transformation

Plasmid DNA of hOCT3 was provided by Dr. Grundemann, the cDNA of hOCT3 is located in vector pcDNA3. Competent DH5α cells (50 µL) were thawed on ice and aliquoted to a pre-chilled tube, then 5 ng plasmid DNA was added to the cells and gently mixed. Mixture was kept on ice for 30 min before heat shocking for 30 s in 42 °C water bath. After adding 950 µL pre-warmed (42 °C) LB broth (Sigma-Aldrich, St. Louis, MO), the tube was kept on ice for 2 min, then shaken for 1 hr at 250 rpm at 37 °C. Different volumes of the mixture were plated on LB-ampicillin (100 mg/mL) agar plates and kept in 37 °C incubator overnight. Ampicillin-resistant colonies were selected and grown in growth media for further experimentation.

3.2.5 Plasmid DNA Extraction

Transformed competent cells were added to 5 mL LB broth containing ampicillin (100 mg/mL) and shaken overnight at 200 rpm, 37 °C. Cells were pelleted by centrifuging at 5000 rpm for 5 min (could be stored at -20 °C). QIAprep Spin Miniprep Kit was used to extract plasmid DNA from cells, the procedure has been described in the protocol [99]. Cell pellet was thoroughly re-suspended with 250 µL of chilled buffer P1 [Tris, EDTA, glucose and RNase A], then lysed by mixing with 250 µL buffer P2 [NaOH and SDS], and neutralized with 350 µL buffer N3 [KAc]. The mixture was centrifuged for 10 min at 13,000 rpm, and the supernatant (about 800 µL) was applied to QIAprep spin column. Column was centrifuged for 1 min at 13,000 rpm, and after

discarding the flow through, 750 µL buffer PE [Tris, and ethanol] was applied, then the column was centrifuged for 1 min at 13,000 rpm twice to discard the flow through completely. QIAprep column was placed in a clean 1.5 mL microcentrifuge tube, and 50 µL buffer EB [NaCl, Tris, and isopropanol] was added to the center of the column and let stand for 1 min before a final 1 min centrifugation at 13,000 rpm to elute plasmid DNA.

3.2.6 Site-Directed Mutagenesis

Site-directed mutagenesis was performed according to the protocol of QuikChange Lightning Site-Directed Mutagenesis Kit [100]. Reagents were added to PCR tubes according to Table 3.1, and PCR was performed with cycles setup as conditions in Table 3.2. Sequences of the primers for each mutation reaction are summarized in Table 3.3. Dpn I restriction enzyme (2 µL) was added to the mixture after PCR reaction and incubated at 37 °C for 5 min, while 45 µL XL 10-Gold Ultracompetent cells (thawed on ice) were aliquoted to a pre-chilled 14-mL BD Falcon polypropylene round-bottom tube. 2-mercaptoethanol (2 µL) was added to the competent cells and incubated on ice for 2 min before 2 µL of the enzyme-treated plasmid DNA was added, then the reaction was incubated on ice for 30 min. The transformation mixture was heat shocked for 45 s at 42 °C before 500 µL NZY$^+$ broth (ThermoFisher Scientific, Waltham, MA) was added. The reaction was incubated on ice for 2 min and the tube was shaken for 1 hr at 250 rpm in 37 °C. Different volumes (50-200 µL) of the mixture were plated on LB-ampicillin (100 mg/mL) agar plates and kept in 37 °C incubator overnight. Ampicillin-resistant colonies were selected and grown in growth media for sequencing and other further experimentation.

Table 3.1 Reagent setup for site-directed mutagenesis.

Reagent	Amount
10* Reaction buffer	5 µL
Plasmid template (5 ng/µL)	5 µL
Oligonucleotide primer #1 (100 ng/µL)	1.25 µL
Oligonucleotide primer #2 (100 ng/µL)	1.25 µL
dNTP mix	1 µL
QuikSolution reagent	1.5 µL
ddH2O	35 µL
QuikChange Lightning enzyme	1 µL (added last)

Table 3.2 PCR cycle parameters.

Cycles	Temperature	Time
1	95 °C	2 min
18	95 °C	20 s
	60 °C	10 s
	68 °C	4 min
1	68 °C	5 min
	4 °C	hold

Table 3.3 Sequences for mutagenesis primers.

Mutation Site	Direction	Sequence (5' – 3')
Phe36Ala	Forward	AGACCACGCCGACGGCGAGGAAGGCGAAGG
	Reverse	CCTTCGCCTTCCTCGCCGTCGGCGTGGTCT
Phe36Tyr	Forward	ACGCCGACGTAGAGGAAGGCGAAGGTG
	Reverse	CACCTTCGCCTTCCTCTACGTCGGCGT
Val40Ala	Forward	GTGCCCAGGAAGGCCACGCCGACGA
	Reverse	TCGTCGGCGTGGCCTTCCTGGGCAC
Val40Leu	Forward	GTGCCCAGGAAGAGCACGCCGACGAAG
	Reverse	CTTCGTCGGCGTGCTCTTCCTGGGCAC
Trp358Ala	Forward	CACCACTGCGCTTGTGAACGCAGCAAACATAAGAATAAGTG
	Reverse	CACTTATTCTTATGTTTGCTGCGTTCACAAGCGCAGTGGTG
Trp358Phe	Forward	CCACTGCGCTTGTGAAGAAAGCAAACATAAGAATAAGTGTGC
	Reverse	GCACACTTATTCTTATGTTTGCTTTCTTCACAAGCGCAGTGG
Trp358Tyr	Forward	CCACTGCGCTTGTGAAGTAAGCAAACATAAGAATAAGTGTGC
	Reverse	GCACACTTATTCTTATGTTTGCTTACTTCACAAGCGCAGTGG

Mutation Site	Direction	Sequence (5’ – 3’)
Glu451Ala	Forward	CTGAATTTACCAAATAAACAATTGCAAAGGCCATGGTTATCCCTAG
	Reverse	CTAGGGATAACCATGGCCTTTGCAATTGTTTATTTGGTAAATTCAG
Glu451Asp	Forward	TAGGGATAACCATGGCCTTTGATATTGTTTATTTGGTAAATTCAGA
	Reverse	TCTGAATTTACCAAATAAACAATATCAAAGGCCATGGTTATCCCTA
Asp478Glu	Forward	TGTTCAGGTCTGTGTGAGTTTGGGGGAATCATAGC
	Reverse	GCTATGATTCCCCCAAACTCACACAGACCTGAACA

3.2.7 DNA Sequencing

DNA sequencing was performed by Genewiz using Sanger DNA sequencing technique (South Plainfield, NJ). Samples containing 10 µL plasmid DNA (80 ng/µL) and 5 µL specific primer (5 pmol/µL) were pre-mixed and shipped to Genewiz. Sequencing results were retrieved electronically.

3.2.8 Tissue Culture

Chinese hamster ovary (CHO) cells were maintained at 37 °C with 5% CO_2 in DMEM F-12 medium (Mediatech Inc., Herndon, VA) containing 10% FBS and 1% penicillin/streptomycin.

Stably transfected CHO cells expressing hOCT3 (CHO-hOCT3), hOCT3 mutants, as well as empty vector, were established in this study. All transfected cell lines were maintained at 37 °C with 5% CO_2 in DMEM F-12 medium containing 10% FBS, 1% penicillin/streptomycin, and 250 µg/mL G418.

3.2.9 Transfection

Stable transfection was performed according to the Lipofectamine® 2000 Reagent protocol [101]. One day before transfection, $8*10^4$ cells/well CHO cells were seeded in 12-well tissue culture plates. On the day of transfection, a mixture of Lipofectamine® 2000 (4 µL/well) and OptiMEM medium (96 µL/well, ThermoFisher Scientific, Waltham, MA) was made by mixing the two ingredients, then the mixture was incubated for 5 min at room temperature. Transfection plasmid DNA (1 µg, 1 µg/µL) was added to 100 µL OptiMEM medium and mixed with 100 µL of Lipofectamine® 2000-OptiMEM medium mixture, then incubated for 20 min at room temperature. Old medium in each well was replaced with new DMEM F-12 medium containing 10% FBS and 1%

penicillin/streptomycin, the 200 µL mixture was then added to each well after incubation and mixed by gentle shaking. The plates were kept in a 37 °C incubator with 5% CO_2, and G418 (1 mg/ml) was applied to transfected cells for selection. Cells were lifted from wells and kept in flasks after patches of G418 resistant cells have been established (successful selection against non-transfected cells).

3.2.10 Cellular Uptake Assay

The procedure for the cellular uptake assay was adapted from that previously published [94]. Two days before cellular uptake experiment, $2*10^5$ cells/well were seeded in 24-well tissue culture plates and grown in the absence of antibiotics. On the day of experiment, cells were equilibrated in transport buffer at room temperature (22-25 °C) for 10 min [500 µL of Hanks' balanced salt solution containing 10 mM HEPES, pH 7.4]. After equilibrium, this solution was replaced with 500 µL of fresh transport buffer containing either unlabeled MPP^+ (1 µM) spiked with [^{3}H]MPP^+ (0.25 µCi/mL) in the presence or absence of inhibitor, or [^{3}H]MPP^+ (0.25 µCi/mL) with increasing concentrations (1 to 200 µM) of unlabeled MPP^+ for the times indicated. At the end of the incubation, the cells were quickly rinsed three times with ice-cold transport buffer and lysed with 200 µL NaOH (1 N). After shaking for two hours, mixture was neutralized with 250 µL HCl (1 N) and 200 µL HEPES (0.01 M). The radioactivity of cell lysate (400 µL from each well) was quantified by liquid scintillation counting, and the uptake profile was normalized by the total protein content measured by the Bradford method. The cellular uptake of substrates was shown as picomoles of substrate per milligram total protein. All uptake data were corrected for background accumulation in corresponding empty vector transfected control cells. Kinetic calculations were performed using

GraphPad Prism Software version 5.0 (GraphPad Software Inc., San Diego, CA). The Michaelis-Menten constant (K_m) was calculated using nonlinear regression. Results were confirmed by repeating all experiments at least three times with triplicate wells for each data point in every experiment.

3.2.11 Transformation Confirmation

Cells were grown in T-75 flasks before experiment and trypsinized for collection. Cells were suspended in 500 µL lysis buffer [1 M Tris (pH 8.0), 5 M NaCl, 0.5 M EDTA, and 10% SDS] containing proteinase K (0.4 mg/mL) and incubated at 55°C while shaking overnight. Genomic DNA was thoroughly extracted from samples with an equal volume of phenol/chloroform/isoamyl alcohol (25:24:1) after vigorously shaking for 10 min, and centrifuged for 10 min at 15,000 g. The upper aqueous phase was carefully transferred to a fresh tube. After adjusting salt concentration with NaAc, 0.7 volumes of isopropanol was added and mixed well, then the mixture was centrifuged immediately at 15,000 g for 30 min to get the DNA pellet. The pellet was washed with 70% ethanol and resuspended with TE buffer [10 mM Tris (pH 8.0), and 1 mM EDTA].

Genomic DNA (2 ng), Master Mix (5 µL), as well as 1 µL primer pair mix (T7 and hOCT3-REV1) were added in a PCR reaction with cycles setup as conditions in Table 3.4. PCR products were loaded to 1% agarose gel for separation using electrophoresis at 120 V for 60 min, and visualized with UV light box after ethidium bromide staining.

Table 3.4 PCR cycle parameters.

Cycles	Temperature	Time
1	95°C	2 min
18	95°C	30 s
	50°C	30 s
	72°C	3 min
1	72°C	5 min
	4°C	hold

3.2.12 Western Blot Assay

The gel for western blot was cast on the same day of the experiment according to the recipe shown in Table 3.5. Plasmid membrane protein and cytosolic protein were extracted from hOCT3, hOCT3 mutant as well as empty vector transfected CHO cells according to Abcam plasma membrane protein extraction kit protocol [102]. Protein concentrations of the samples were quantified with Bradford method. Plasma membrane protein from each sample (30 μg) was prepared, volume of the samples was adjusted to the same with phosphate buffer [1 M NaH_2PO_4, 1 M Na_2HPO_4], and 5× SDS loading buffer [10% 2-mercaptoethanol, 150 mM Tris, 5% SDS, 25% glycerol, 0.05% bromphenol blue, DI water] was added before the sample was boiled in water for 5 min or incubated in 37 °C water bath for 30 min. After loading the ladder and samples onto the gel, electrophoresis was conducted by applying a current for 60 min at 170 V. The proteins were transferred to PVDF (or nitrocellulose) membrane by applying electrophoresis at 100 mAmps for 60 min, then the membrane was blocked with 5% BSA for 1 hr at room temperature. Membrane was incubated with primary antibody (1:200 with 5% BSA) overnight at 4 °C, and washed with 1× TBS for 3 times (10 min each). Membrane was then incubated with secondary antibody (1:200 with 5% BSA) for 2 hr at room temperature, and washed with 1× TBS for 3 times. NBT/BCIP substrate (diluted with AP buffer, Roche Diagnostics, Indianapolis, IN) was applied to the membrane for protein visualization.

3.2.13 Statistics

Data are reported as mean ± SD. Statistical differences were analyzed using one-way ANOVA followed by Dunnett's post-hoc t-test (α=0.05).

Table 3.5 Recipe for western blot gel.

Running gel		Stacking gel	
Reagent	Volume	Reagent	Volume
H_2O	1.65ml	H_2O	2.83ml
30% Acrylamide mix	1.3ml	30% Acrylamide mix	0.54ml
1M Tris (pH 8.8)	1.95ml	1M Tris (pH 6.8)	0.5ml
10% SDS	50ul	10% SDS	40ul
10% fresh APS	50ul	10% fresh APS	40ul
TEMED	6ul	TEMED	6ul

3.3 Results

3.3.1 Homology modeling of human organic cation transporter 3

GOLD scores of the top ten docked poses of MPP^+ in the binding pocket of hOCT3 are summarized in Table 3.6 along with their corresponding DOPE scores. The largest GOLD score represents the best docking pose, and the smallest DOPE score demonstrates the best homology model. Since our focus was on the binding interaction between docking substrate and hOCT3, our model selection criteria was primarily based on the GOLD score, and by comparing the DOPE scores of these models with top GOLD scores, we noticed that Model 10 not only had the best GOLD score, its DOPE score was also lower than most of the other top ranked models. Thus we chose Model 10 as our best 3-D homology model for hOCT3. The generated 3-D homology model is shown in Figure 3.3 (viewing from extracellular side of the membrane) along with the hypothesized binding pocket; a 2-dimensional demonstration of the topology of this hOCT3 model across plasma membrane is shown in Figure 3.4, and amino acid residues forming the MPP^+ binding pocket are highlighted.

PROCHECK analysis of the selected hOCT3 model generated a Ramachandran plot for the model (Figure 3.5). Ramachandran plot provides a way to visualize energetically allowed regions for backbone torsion angles psi against phi of amino acid residues in protein structure; the plot demonstrates the empirical distribution of data points (amino acid residues) observed in a single structural model. In a Ramachandran plot, amino acids are distributed in four regions – most favored region (red), additional allowed region (yellow), generously allowed region (light yellow) and disallowed region (white). For this hOCT3 model, 83.8% of amino acids were in the most favored region,

12.7% in the additional allowed region, and only a total of 3.5% in the generously and disallowed region (disallowed residues highlighted in Figure 3.4). These observations imply that the structure of our model for hOCT3 is plausible.

Table 3.6 GOLD and DOPE scores for hOCT3.

Model identifier	GOLD score	DOPE score
Model 10	51.70	-47556.887
Model 93	51.04	-47705.746
Model 40	50.66	-47517.859
Model 21	48.98	-47247.949
Model 46	48.80	-47451.941
Model 35	48.21	-46998.316
Model 19	48.15	-47372.027
Model 24	47.61	-47997.582
Model 72	47.30	-47882.953
Model 51	47.02	-47385.375

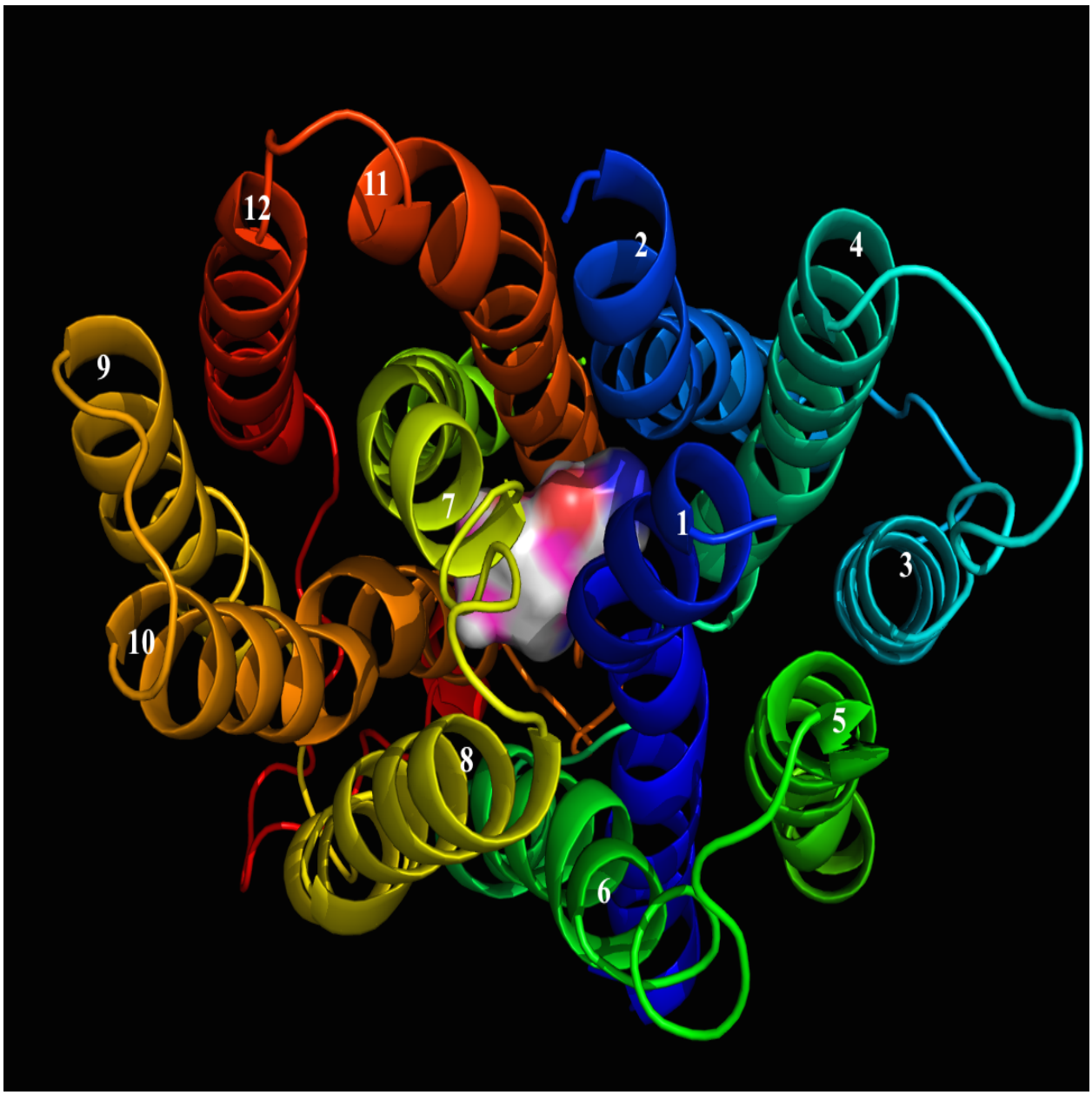

Figure 3.3 3-D homology model of hOCT3.

Transmembrane domains are depicted as ribbons in different colors in sequence (numbered 1 – 12) and hypothesized binding pocket is shown as 'surface' in the middle.

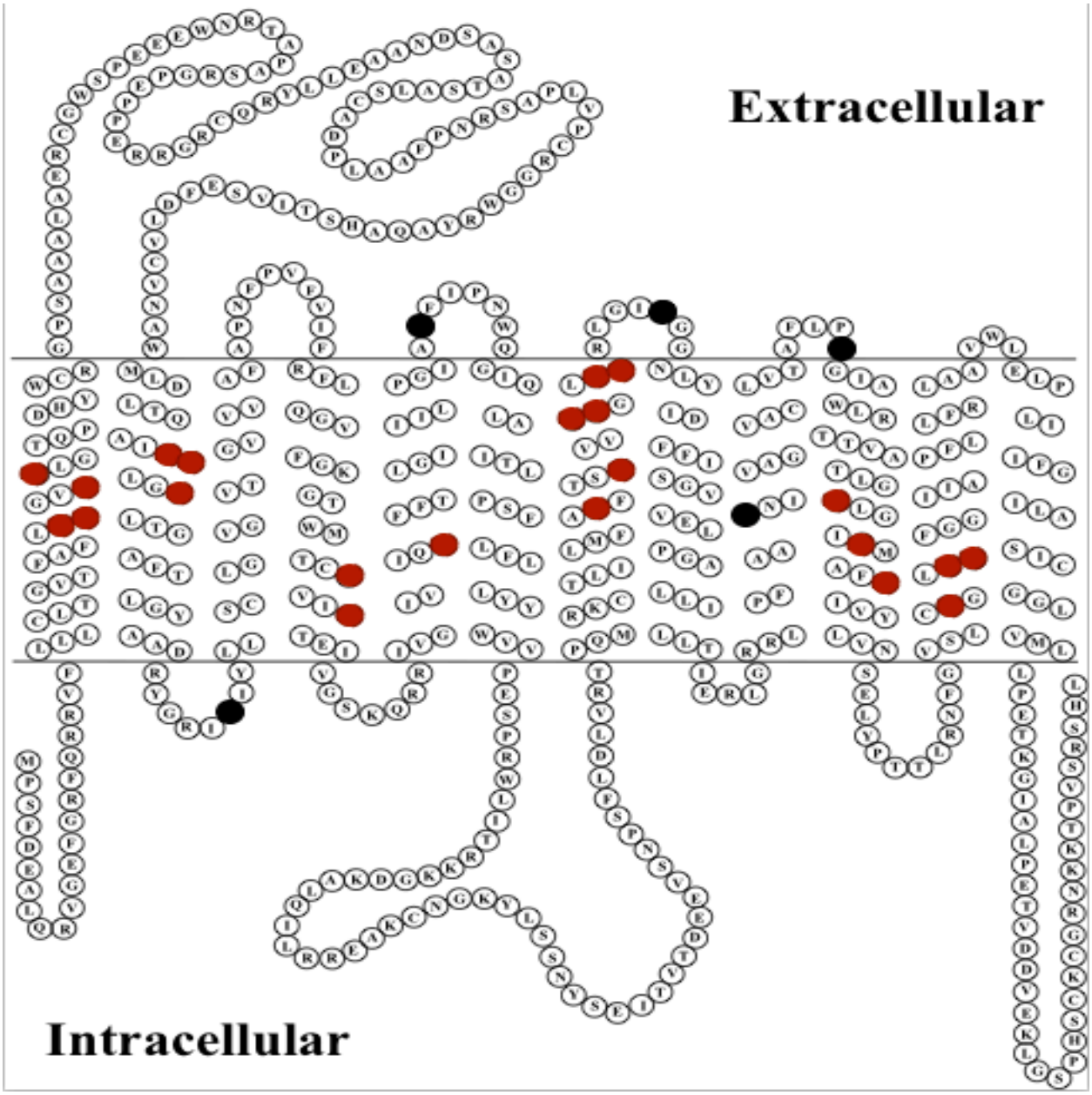

Figure 3.4 2-D topology of hOCT3 across plasma membrane.

Highlighted amino acids (red) are residues forming the binding pocket, and might be involved with hOCT3-substrate interactions; amino acids in black are residues identified to be in the disallowed region in the Ramanchandran plot.

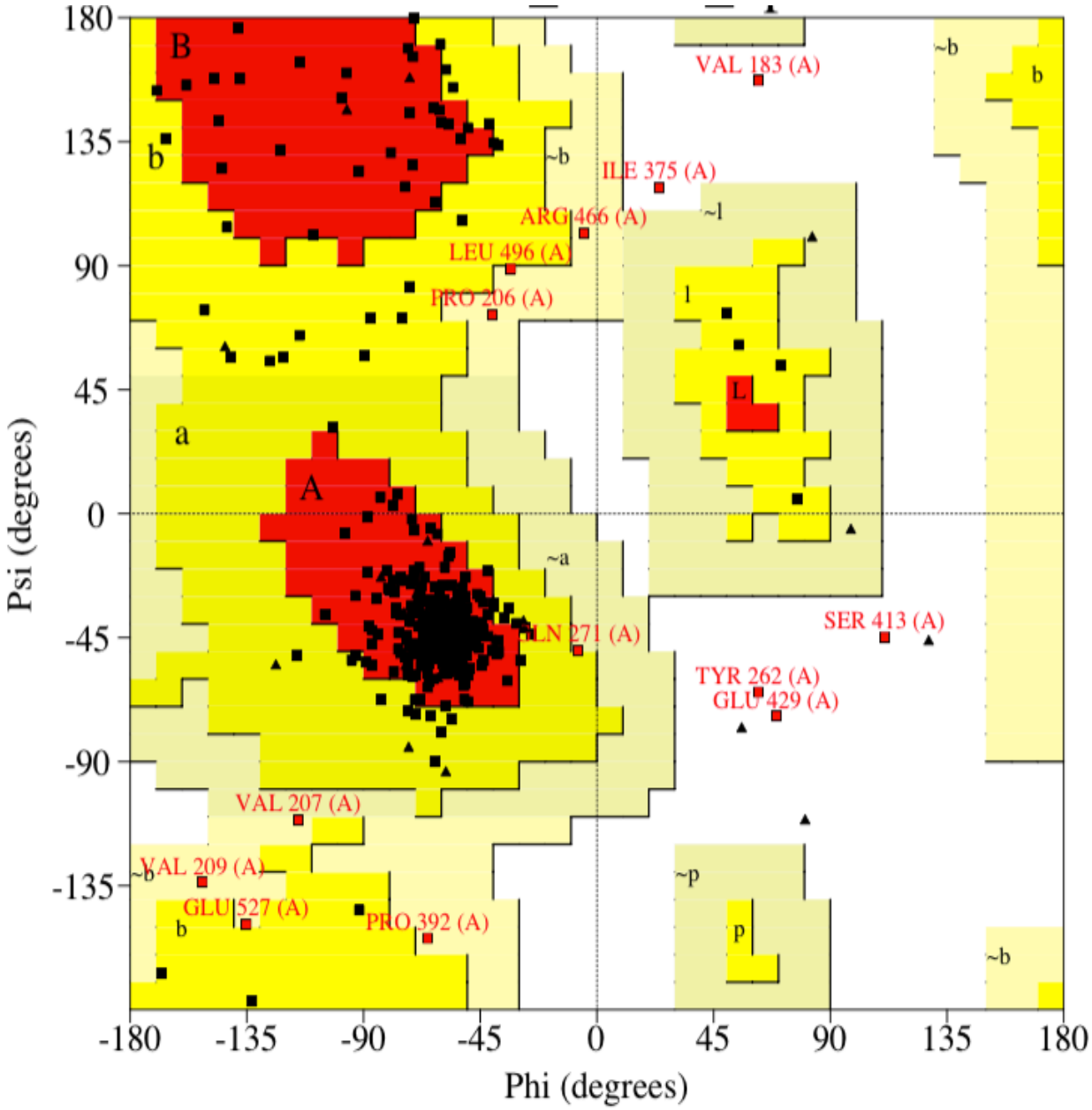

Figure 3.5 Ramachandran plot of hOCT3.

Phi and psi indicate backbone conformation torsion angles of amino acid residues, which represent the rotations of a polypeptide main chain N-Cα and Cα-C bonds. Amino acids are laid out in different regions: most favored region (red), additional allowed region (yellow), generously allowed region (light yellow), and disallowed region (white). Residues depicted in red squares are in the generously allowed and disallowed regions.

Visualizing the generated homology model for hOCT3 in Pymol, we were able to identify all the amino acid residues surrounding and forming the large binding pocket responsible for MPP^+ docking in the transporter. These residues are from different transmembrane domains that intertwine and form the binding region: TMD 1 (Phe36, Val37, Val40, Phe41), TMD 2 (Leu161, Asn162, Phe165), TMD 4 (Tyr227, Val230), TMD 5 (Met248), TMD 7 (Trp358, Ala362, Tyr365, Gln366, Val369, Met370), TMD 10 (Arg443, Thr447, Glu451), and TMD 11 (Ser474, Cys477, Asp478) (Figure 3.6).

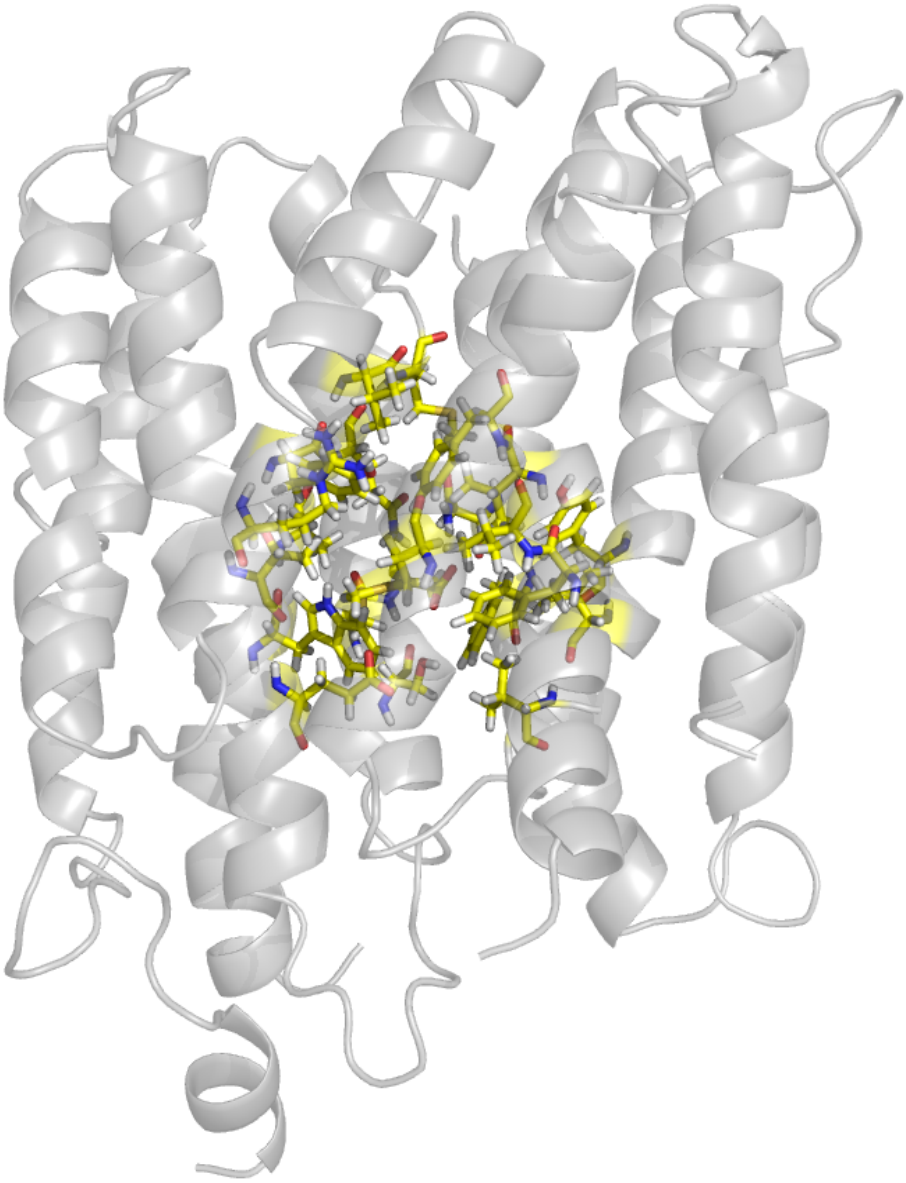

Figure 3.6 3-D demonstration of binding pocket for MPP^+ in hOCT3.

Residues forming the binding pocket are depicted as yellow sticks.

3.3.2 Critical residues identified through substrate docking

To support our modeling study, MPP^+ (prototypical substrate for OCTs) was energy minimized in SYBYL X using Tripos force field with Gasteiger-Hückel charges and docked to the binding pocket of hOCT3 model to identify amino acid residues critical for MPP^+-hOCT3 interactions in GOLD suite 5.4.

From the docking result, the protonated aromatic ring of MPP^+ was detected to be interacting with the negatively charged glutamic acid residue in the pocket (Asp478) through H-bond interaction (Figure 3.7). Moreover, the pyridinium ring and the benzene ring of MPP^+ were seen to be interacting with Phe36, Val40, Trp358, and Glu451 in aromatic or hydrophobic manners (Figure 3.7), these interactions are summarized in Table 3.7.

OCTs are polyspecific transporters, i.e. they have the ability to interact with and transport molecules of different structures. Thus we also investigated hOCT3 interactions with several other substrates showing structural diversity from MPP^+ through energy minimization and docking. Identified amino acid residues that could potentially affect substrate-transporter interactions, as well as their interaction types are summarized in Table 3.7, and shown in Figure 3.8. Comparing the amino acid residues identified for each docking compound, we have noticed that all identified residues could be located in the binding pocket defined for MPP^+ (Figure 3.6), several 'critical' residues were common among certain compounds while others were unique for specific substrate(s). This indicates that the docked substrates would likely bind to the same pocket in the transporter and their specific binding regions may overlap, but these regions are not exactly the same.

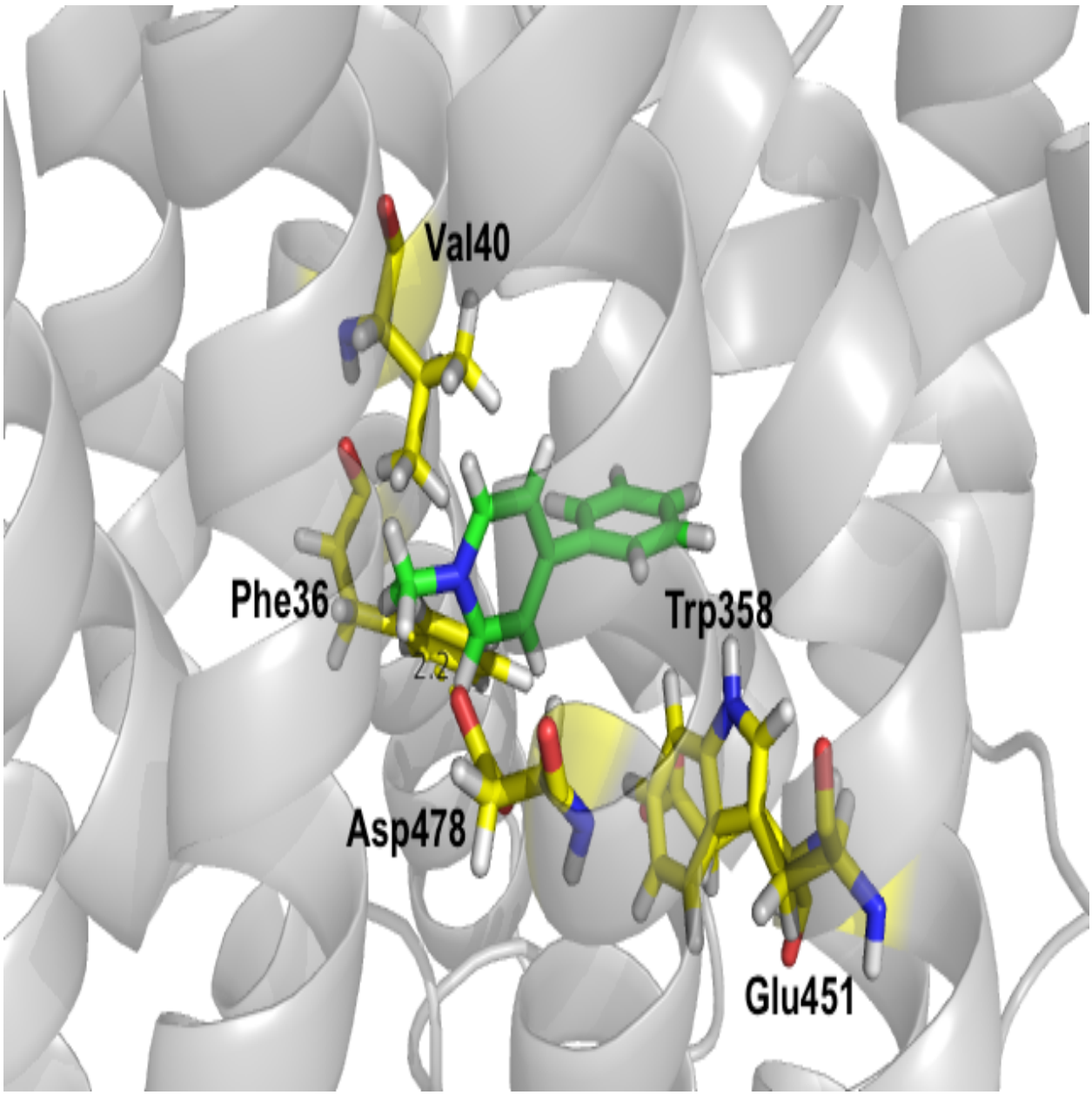

Figure 3.7 MPP^+ docked in the substrate binding region of hOCT3.

The ligand (MPP^+, green) and 'critical' amino acid residues (yellow) are displayed as sticks. The dashed line indicates the H-bond interaction between the protonated aromatic ring of MPP^+ and the negatively charged residue Asp478.

Table 3.7 MPP^+ docking result summary for hOCT3.

Docking substrate	Amino acid residue	Type of interaction
MPP^+	Phe36	Edge face interaction
	Val40	Hydrophobic interaction
	Trp358	Edge face interaction
	Glu451	Edge face/arene-H interaction
	Asp478	H-bond interaction
Serotonin	Val40	Arene-H interaction
	Asn162	Side-chain donor
	Met248	Side-chain acceptor
	Asp478	Side-chain acceptor
Metformin	Met248	Side-chain acceptor
	Trp358	Arene-H interaction
	Ser474	Backbone acceptor
	Asp478	Side-chain acceptor
TPA^+	Trp358	Arene-H interaction
Epinephrine	Phe36	Arene-H interaction
	Val40	Arene-H interaction
	Asn162	Side-chain donor
	Met248	Side-chain acceptor
	Gln366	Side-chain donor
	Cys477	Side-chain acceptor
	Asp478	Side-chain acceptor

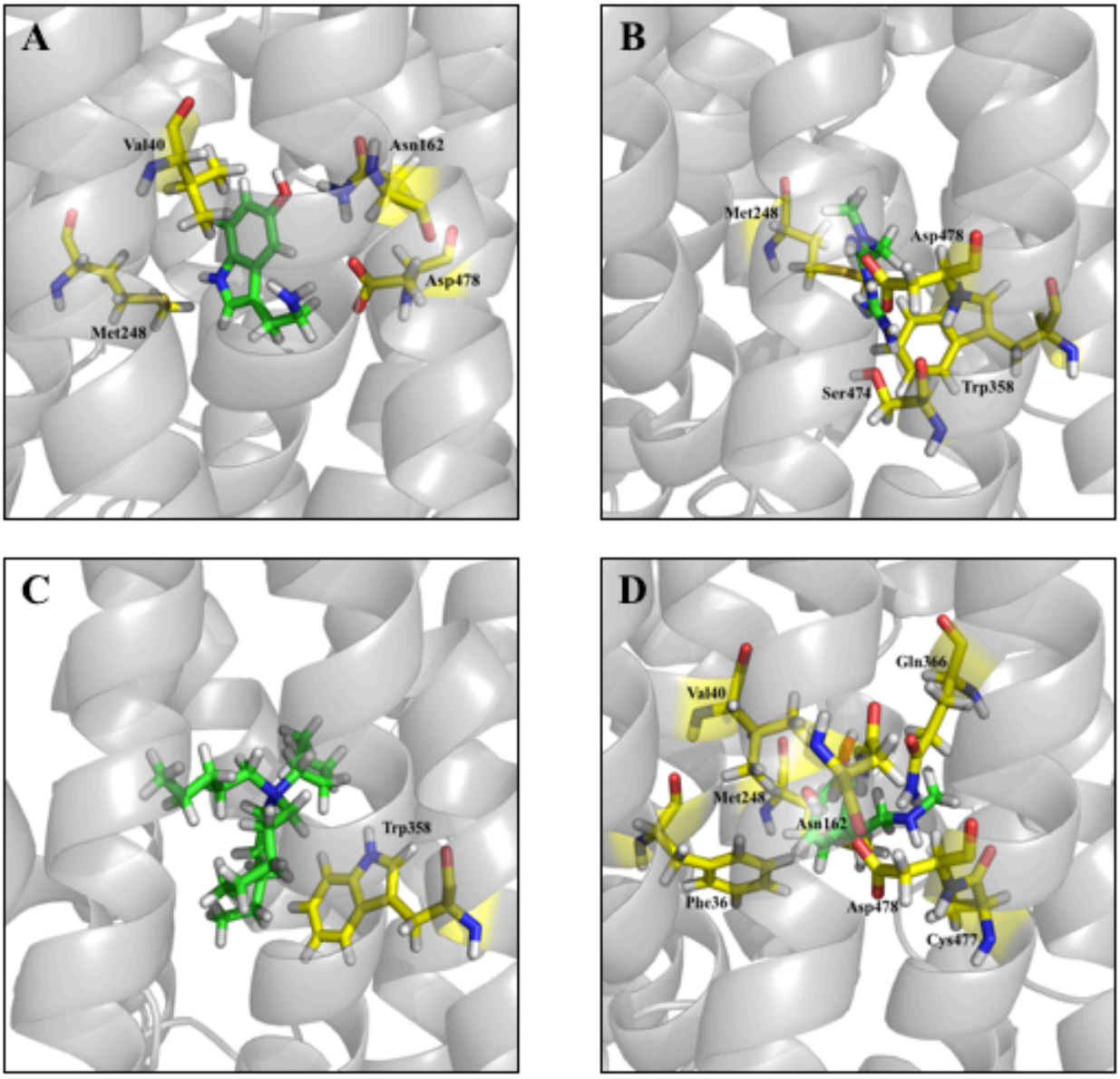

Figure 3.8 Other compounds docked in the substrate binding region of hOCT3.

The ligands (green) – serotonin (A), metformin (B), TPA^+ (C), and epinephrine (D), as well as 'critical' amino acid residues (yellow) are displayed as sticks, and summarized in Table 3.5.

3.3.3 Critical residue substitution

To test our model predictions and if the residues identified are indeed critical for MPP^+-hOCT3 interactions, both conservative and non-conservative (Figure 3.9, [103]) substitutions were introduced to these positions to detect changes in hOCT3 affinity for MPP^+. Both single mutants and double mutants were generated. The substitutions for each residue are listed in Table 3.8.

Since there is no commercially available hOCT3 antibody with consistent performance, we added a FLAG tag (a short piece of peptide with sequence DYKDDDDK) after the last amino acid of hOCT3 (before the stop codon) in order to perform immunoblotting on hOCT3 protein for successive studies; the scheme is shown in Figure 3.10. Using the QuikChange Lightning Site-Directed Mutagenesis Kit along with PAGE-purified oligo primers specifically designed for each site, substitutions were performed and later on confirmed through DNA sequencing (sequencing results for the mutated sites shown in Figure 3.11).

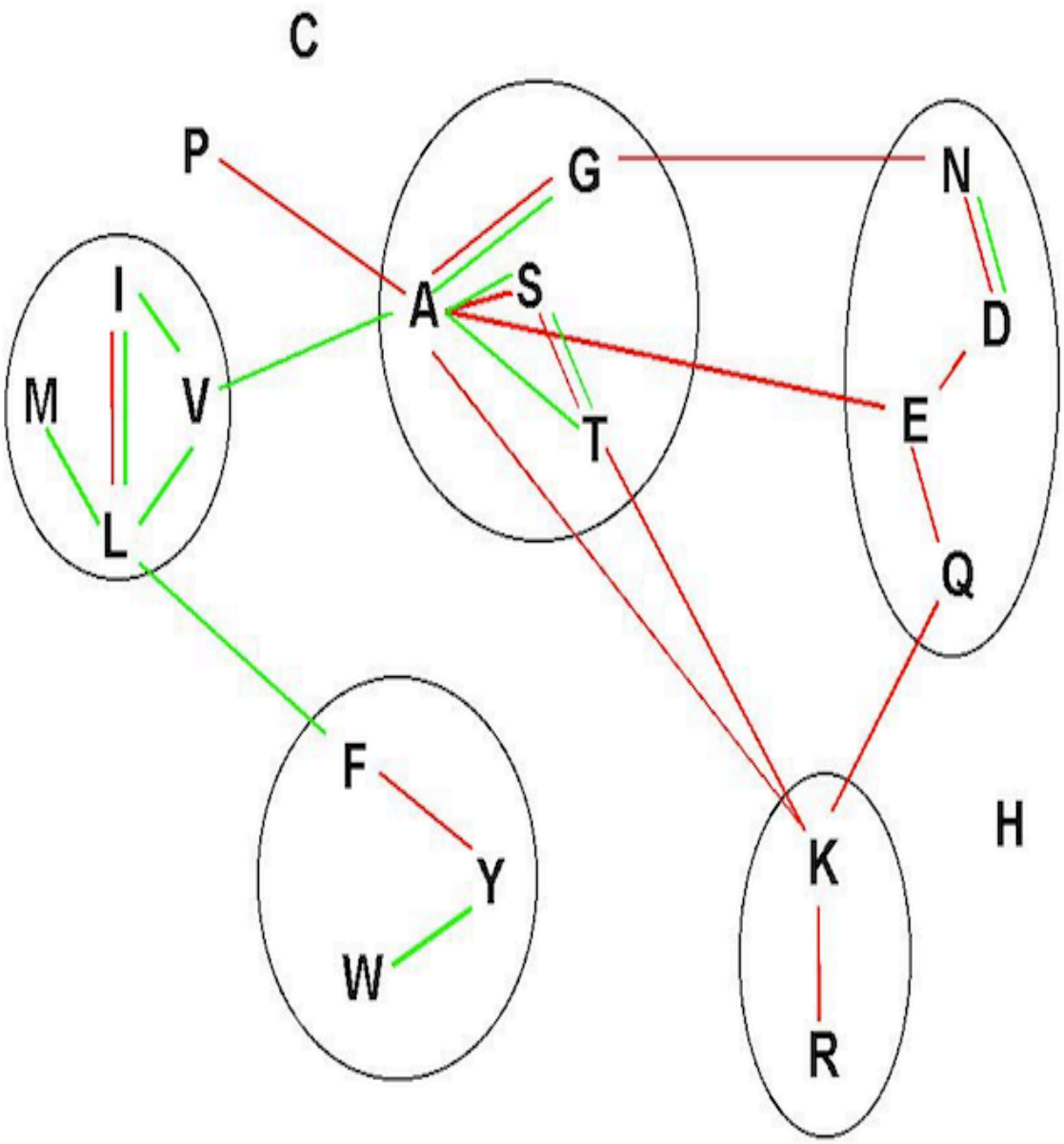

Figure 3.9 Recommended conservative amino acid substitution scheme [103].

Residues roughly equivalent are grouped together in five subsets, which generally correlate with side-chain physicochemical properties.

Table 3.8 Summary of critical residue substitutions.

	Critical residue	Substitution
Single mutants	Phe36	Tyr
		Ala
	Val40	Leu
		Ala
	Trp358	Phe
		Tyr
		Ala
	Glu451	Asp
		Ala
	Asp478	Glu
Double mutants	Phe36Tyr & Val40Leu	
	Phe36Tyr & Glu451Ala	
	Val40Leu & Glu451Ala	

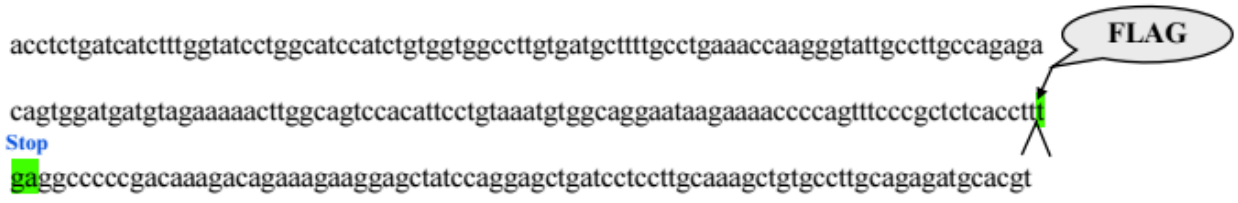

Figure 3.10 Scheme for adding FLAG tag to hOCT3.

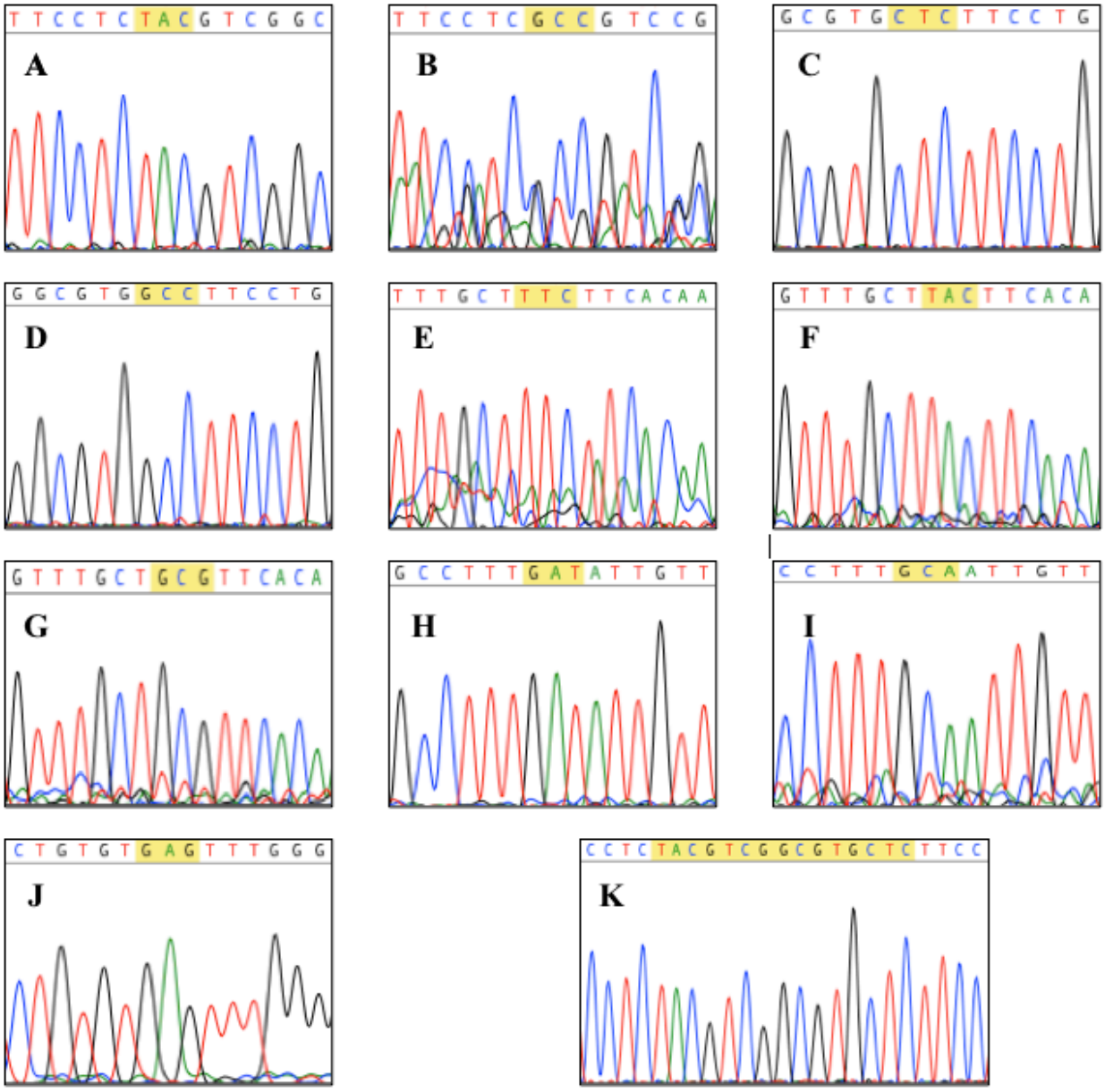

Figure 3.11 Sequencing results for mutants.

Figures were cropped from sequencing results for hOCT3-FLAG mutants Phe36Tyr (A), Phe36Ala (B), Val40Leu (C), Val40Ala (D), Trp358Phe (E), Trp358Tyr (F), Trp358Ala (G), Glu451Asp (H), Glu451Ala (I), Asp478Glu (J), and Phe36TyrVal40Leu (K), with the highlighted parts indicating the substituted sites.

3.3.4 Critical residue confirmation

Upon successful stable transfection of wild type hOCT3 (both regular and FLAG-tagged) as well as generated hOCT3 mutants, we performed an initial screening on the transfected cell lines to detect MPP^+ transport activity (Figure 3.12). Stably transfected non-FLAG hOCT3 wild type-expressing (CHOhOCT3) cells showed marked accumulation of MPP^+ (~3.5 fold) compared to empty vector transfected (pcDNA3.1, CHO-EV) background control cells (11.0 ± 0.2 vs. 3.4 ± 1.5 pmol/mg protein/10 min, respectively). FLAG-tagged hOCT3 wild type-expressing (CHOhOCT3-FLAG) cells exhibited ~7 fold accumulation of MPP^+ (22.7 ± 0.3 pmol/mg protein/10 min) as compared to CHO-EV cells. The known OCT inhibitor quinine (200 μM), showed virtually complete inhibition of hOCT3-mediated MPP^+ uptake (Figure 3.12). Cell accumulation assay demonstrated that the residue substitutions Val40Ala, Trp358Ala, Trp358Phe, Trp358Tyr, Asp478Glu, and double mutant Phe36TyrGlu451Asp almost completely abolished the transport activity of hOCT3 for MPP^+, while the other mutant hOCT3s expressed some level of MPP^+ transport (Figure 3.12). This indicates that residues Trp358 and Asp478 are extremely critical for the interactions between hOCT3 and MPP^+ during the transport process, since a mild change in that specific amino acid (conservative substitution) destroyed transport activity for MPP^+.

Next, for variants still demonstrating MPP^+ transport activity, dose-response studies were performed to estimate K_m values and confirm any changes as compared to wild type hOCT3 (Figure 3.13, Table 3.8). Comparing the K_m values of wild type hOCT3 and FLAG-tagged wild type hOCT3, we noticed that adding the FLAG tag did not significantly alter the affinity of hOCT3 for MPP^+ (16 ± 2.2 vs. 18.4 ± 1.7 μM,

respectively) (Figure 3.13, Table 3.9). Comparing the K_m values of hOCT3 mutants to that of the two wild type hOCT3s (wild type and FLAG-tagged wild type hOCT3), we observed that Phe36Ala, Val40Leu, Glu451Ala, and Val40Leu-Glu451Ala mutations resulted in significantly decreased transporter affinity for MPP^+ (Figure 3.13, Table 3.9), whereas Phe36Tyr, Glu451Asp, and Phe36Tyr-Val40Leu mutations did not significantly change the affinity for MPP^+ (Figure 3.13, Table 3.9). Also by comparing the K_m values of transporter mutants of the same residue, we noticed that substituting the amino acid to alanine (non-conservative substitution) clearly decreased affinity of the transporter for MPP^+ to a larger extent than the conservative mutant; in one case, the non-conservative substitution completely diminished MPP^+ transport (Val40Ala) (Figure 3.12). The changes in transporter affinity for MPP^+ suggest that all of these identified residues are involved in the interaction between hOCT3 and MPP^+.

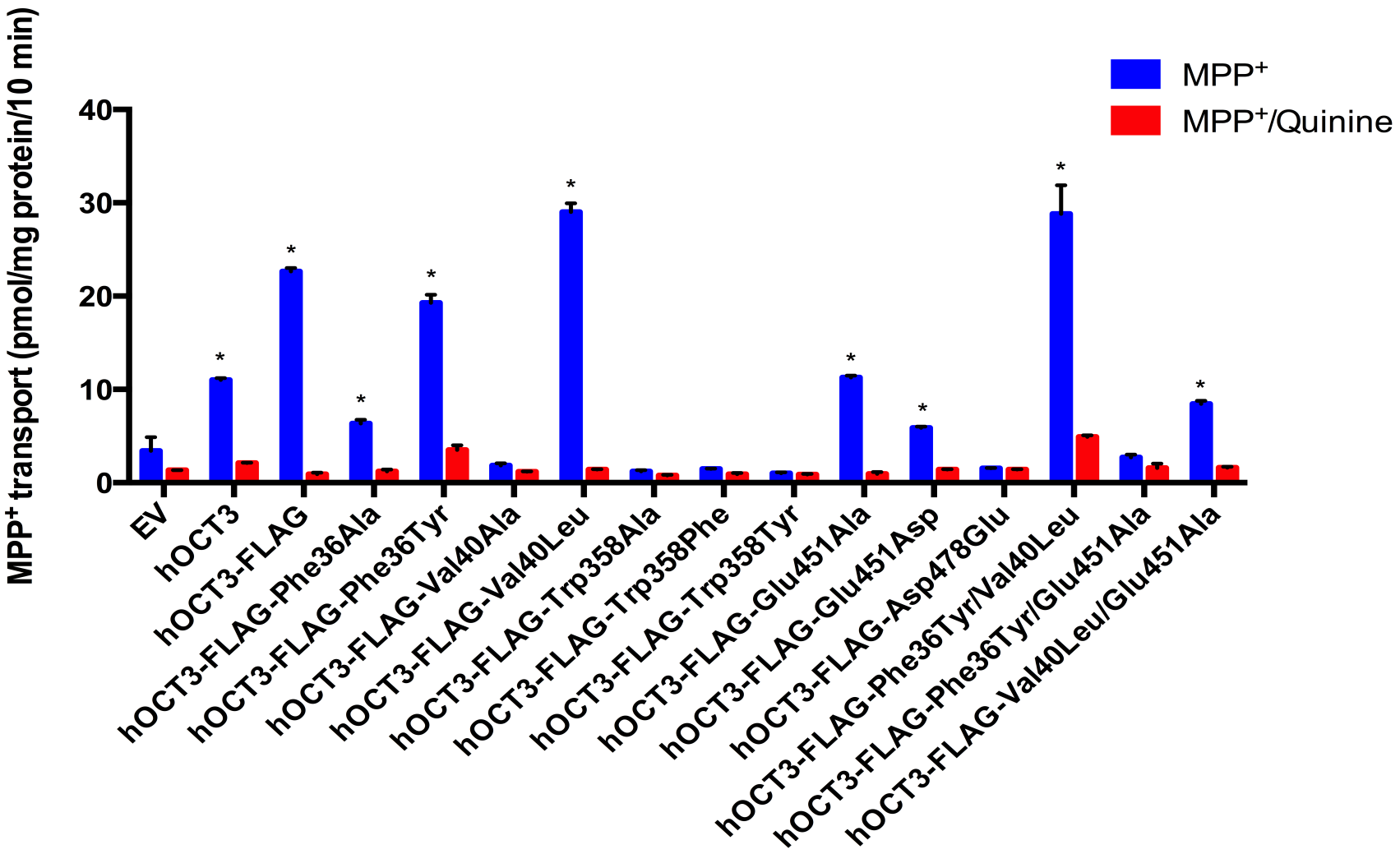

Figure 3.12 Functional screening of wild type and mutant hOCT3 transfected CHO cell lines.

The concentration of MPP^+ was 1 μM, and the concentration of quinine was 200 μM; incubation time was 10 min. Values are mean ± SD of triplicate values. * denotes $p<0.05$ as determined by one-way ANOVA followed by Dunnett's t-test.

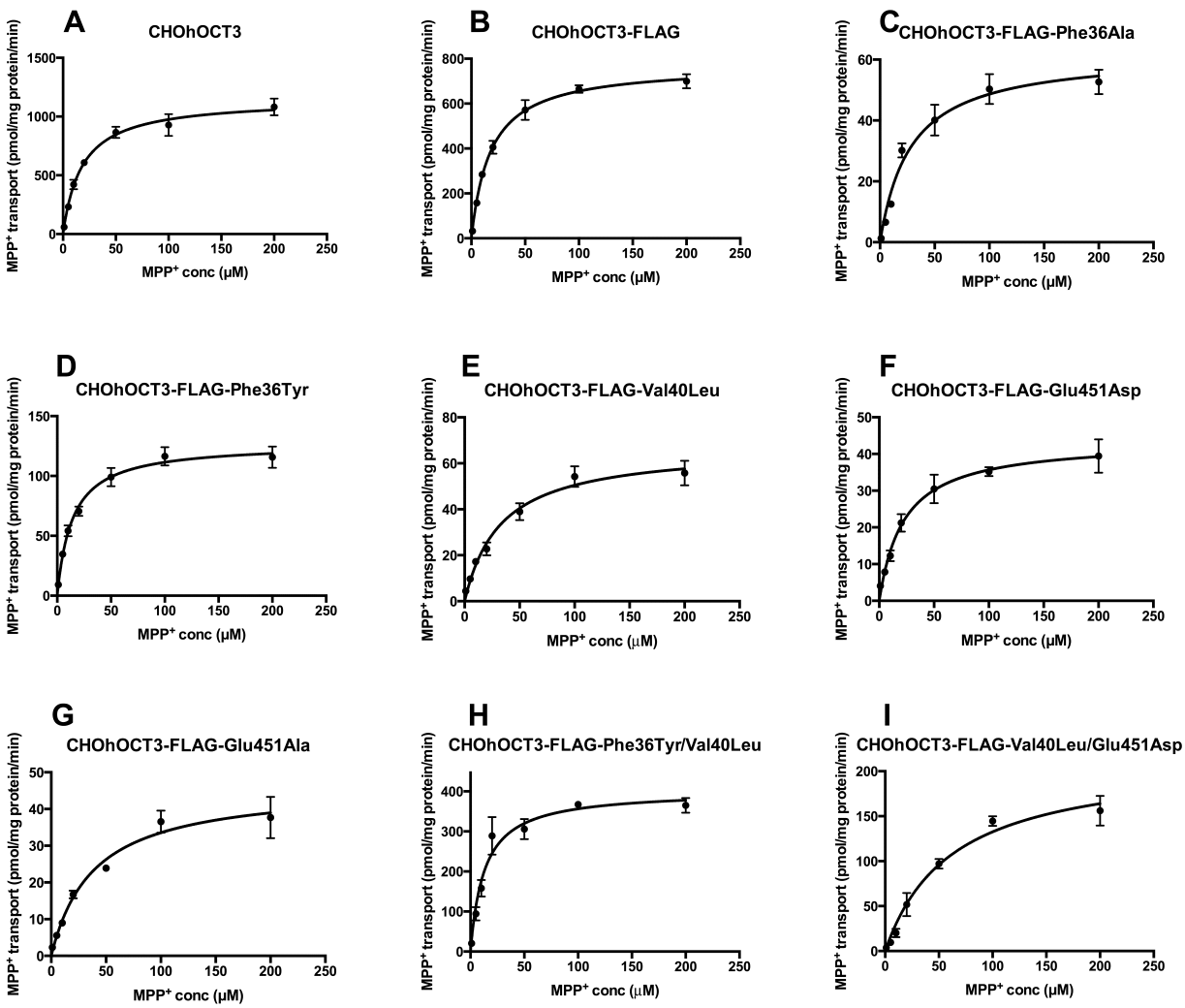

Figure 3.13 Dose-response curves for MPP^+ on wild type and mutant hOCT3.

Michaelis-Menten kinetics of MPP^+ transport in (A) hOCT3, (B) hOCT3-FLAG, (C) hOCT3-FLAG-Phe36Ala, (D) hOCT3-FLAG-Phe36Tyr, (E) hOCT3-FLAG-Val40Leu, (F) hOCT3-FLAG-Glu451Ala, (G) hOCT3-FLAG-Glu451Asp, (H) hOCT3-FLAG-Phe36TyrVal40Leu, and (I) hOCT3-FLAG-Val40LeuGlu451Ala transfected CHO cells. Representative data showing 1 min uptake of MPP^+ measured in stably transfected CHO cells in the presence of increasing concentrations of MPP^+ (1 to 200 μM) are shown. Data were corrected for nonspecific background measured in empty vector control cells and are means ± SD of triplicate values. K_m values were determined with nonlinear regression and the "Michaelis-Menten" model in GraphPad Prism software.

Table 3.9 Summarized K_m values of MPP^+ for wild type and mutant hOCT3.

Transporter type	K_m (μM)
hOCT3	16.0 ± 2.2
hOCT3-FLAG	18.4 ± 1.7
hOCT3-FLAG-Phe36Ala	29.1 ± 2.0*
hOCT3-FLAG-Phe36Tyr	14.6 ± 0.5
hOCT3-FLAG-Val40Leu	32.2 ± 4.3*
hOCT3-FLAG-Glu451Ala	40.9 ± 4.8*
hOCT3-FLAG-Glu451Asp	23.4 ± 3.9
hOCT3-FLAG-Phe36TyrVal40Leu	14.4 ± 1.7
hOCT3-FLAG-Val40LeuGlu451Ala	70.0 ± 9.7*

K_m values were expressed as mean ± SD from triplicate determinations.
* denotes significant difference between wild type and mutant hOCT3 K_m values $p < 0.05$ as determined by two-tailed Student's unpaired t-test.

3.3.5 Plasmid DNA detection of non-functional hOCT3 mutants

To prove the success of stable transfection of cell lines exhibiting no MPP^+ transport activity, genomic DNA from specific transfected cell lines was extracted and amplified through PCR using primer pairs that recognize both ends of hOCT3 cDNA (amplicon size~1.7 kb). Bands shown in Figure 3.14 with sizes about 1.7 kb proved the success of transfection as well as existence of hOCT3 cDNA in tested cell lines (one wild type, one hOCT3 mutant with MPP^+ transport activity, and all non-functional hOCT3 mutants).

3.3.6 Immunodetection of non-functional hOCT3 mutants

To examine the presence of transporter protein in the plasma membrane, western blot assays were conducted. Utilizing both hOCT3- and FLAG-targeting primary antibodies, cytosolic and plasma membrane protein fractions were probed under various conditions. Unfortunately, we were not able to detect any OCT3 signal. However, immunodetection of β-actin in the cytosolic fractions was successful (Figure 3.15), indicating proper technique. Refinement of hOCT3 western blot protocol is ongoing.

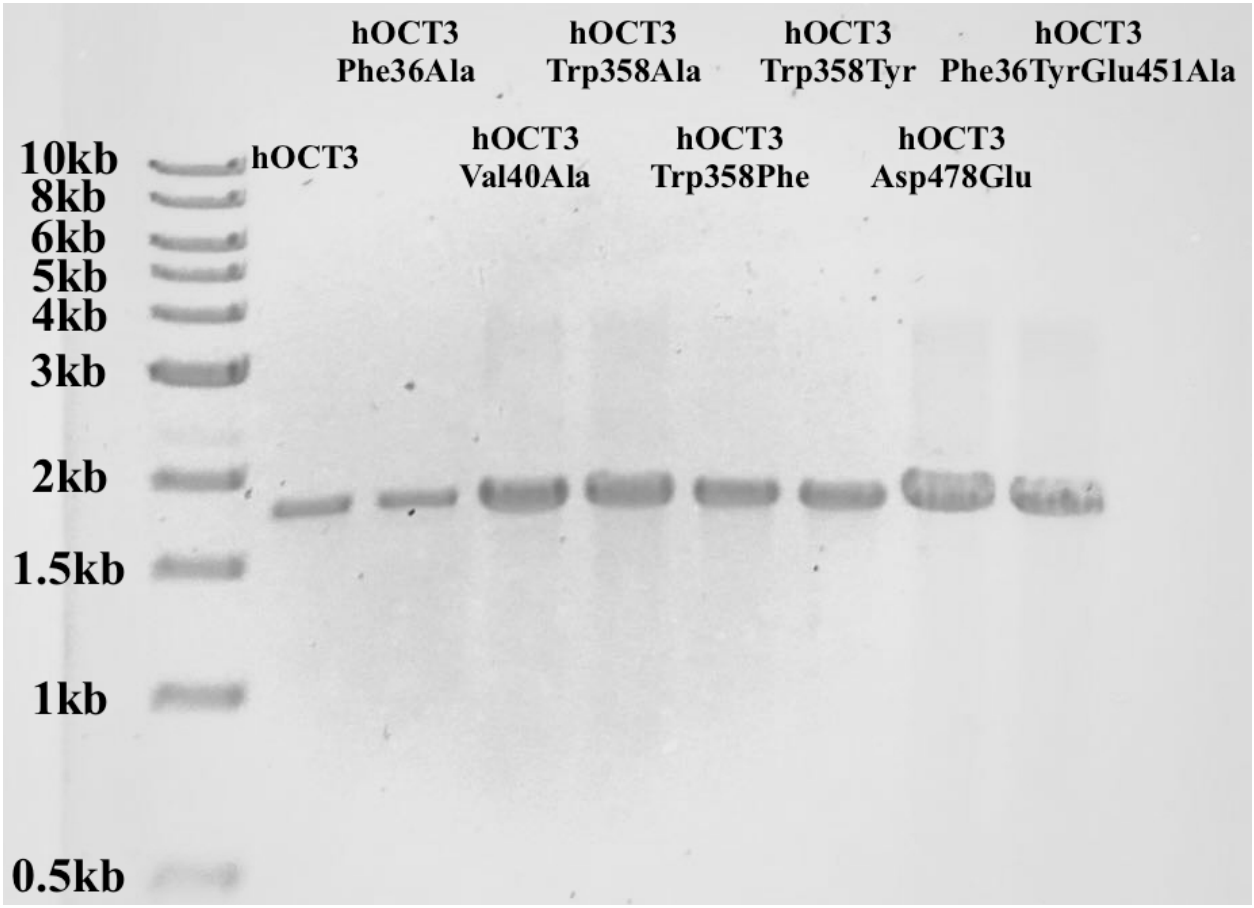

Figure 3.14. PCR result for genomic DNA of mutant cell lines.

TriDye 1 kb DNA Ladder located in lane 1, followed by wild type hOCT3 (lane 2), hOCT3 mutant with transport activity (lane 3), and all non-functional mutants (lane 4 to lane 9).

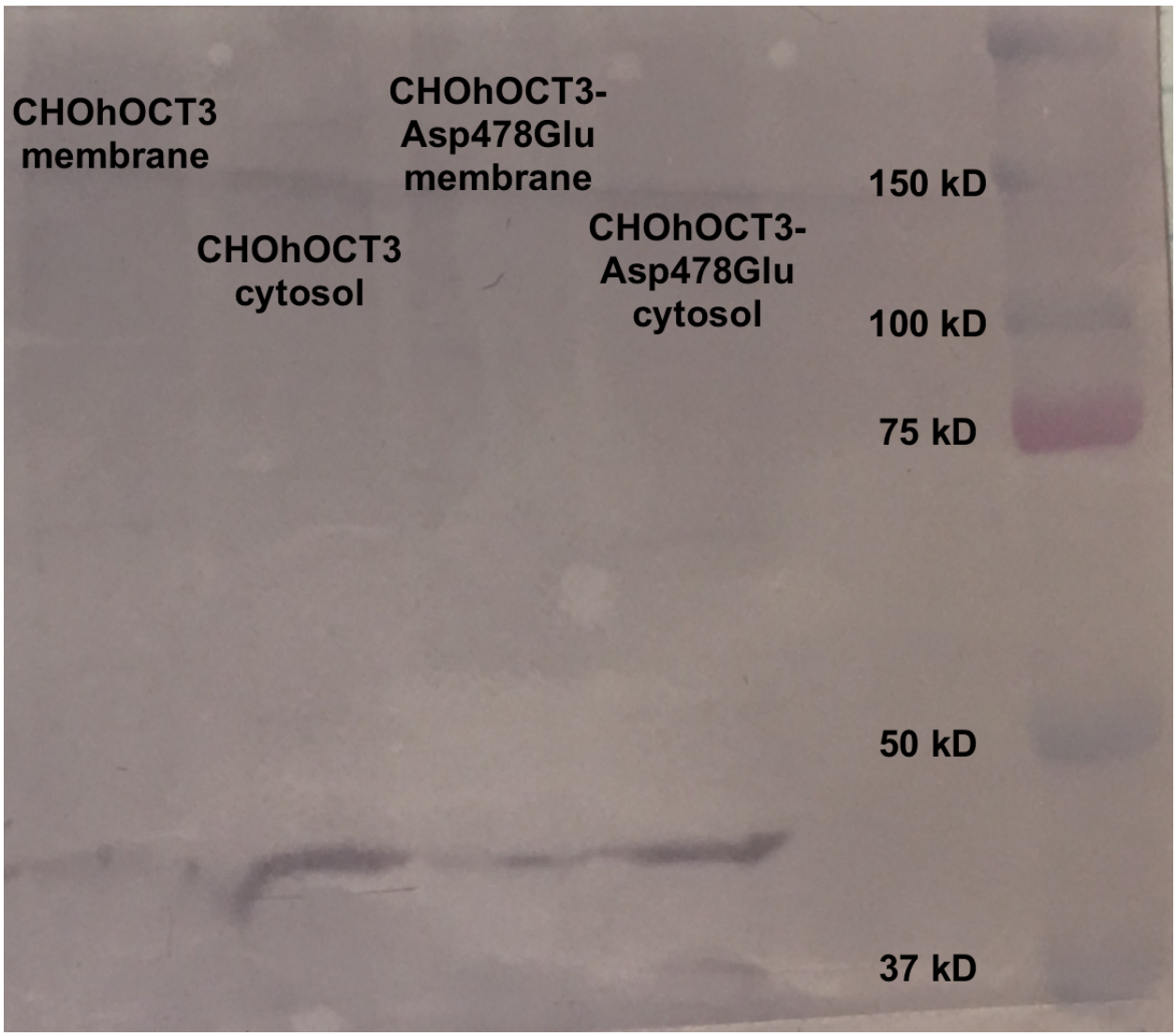

Figure 3.15. Western blot result for wild type and mutant hOCT3 cell lines.

Western blot image showing the detection of β-actin (43 kD) in membrane and cytosolic fractions of wild type and mutant hOCT3 cell lines.

3.3.7 Homology modeling and docking of mutant hOCT3

To further test the performance of our hOCT3 model and the importance of identified residues, novel 3-D homology models of one functional mutant transporter (hOCT3-Val40Leu) as well as three of the nonfunctional mutant transporters (hOCT3-Val40Ala, hOCT3-Trp358Tyr, and hOCT3-Asp478Glu) were generated. MPP^+ was again used as the docking compound to identify any potential interaction between the ligand and the binding pocket. Docking results are shown in Figure 3.15 as well as Figure 3.16 (A), (B), and (C) respectively.

In the hOCT3-Val40Leu model, all of the amino acid residues (Phe36, Trp358, Glu451, and Asp478; except for the substituted residue at position 40, Figure 3.16) identified as 'critical' for MPP^+-hOCT3 interactions were still predicted to be interacting with MPP^+ in similar manners (summarized in Table 3.10). In contrast, the substituted amino acid (Leu40) was farther away from the docked ligand (MPP^+), thus the probability of interaction between Leu40 and MPP^+ is greatly reduced (Figure 3.16). For the other residues, although still identified as critical, their interactions with MPP^+ were not as strong compared with the residues in the wild type model. The distance between the negatively charged atom in Asp478 and the positively charged atom in MPP^+ was longer in the mutant model (2.5 Å vs. 2.2 Å in the wild type hOCT3 model), and aromatic interactions between MPP^+ and other residues were weaker (as shown in Figure 3.16). Thus the decreased affinity for Val40Leu mutant could be a result of slightly altered binding pocket conformation after residue substitution, which changed interaction strengths between MPP^+ and the transporter.

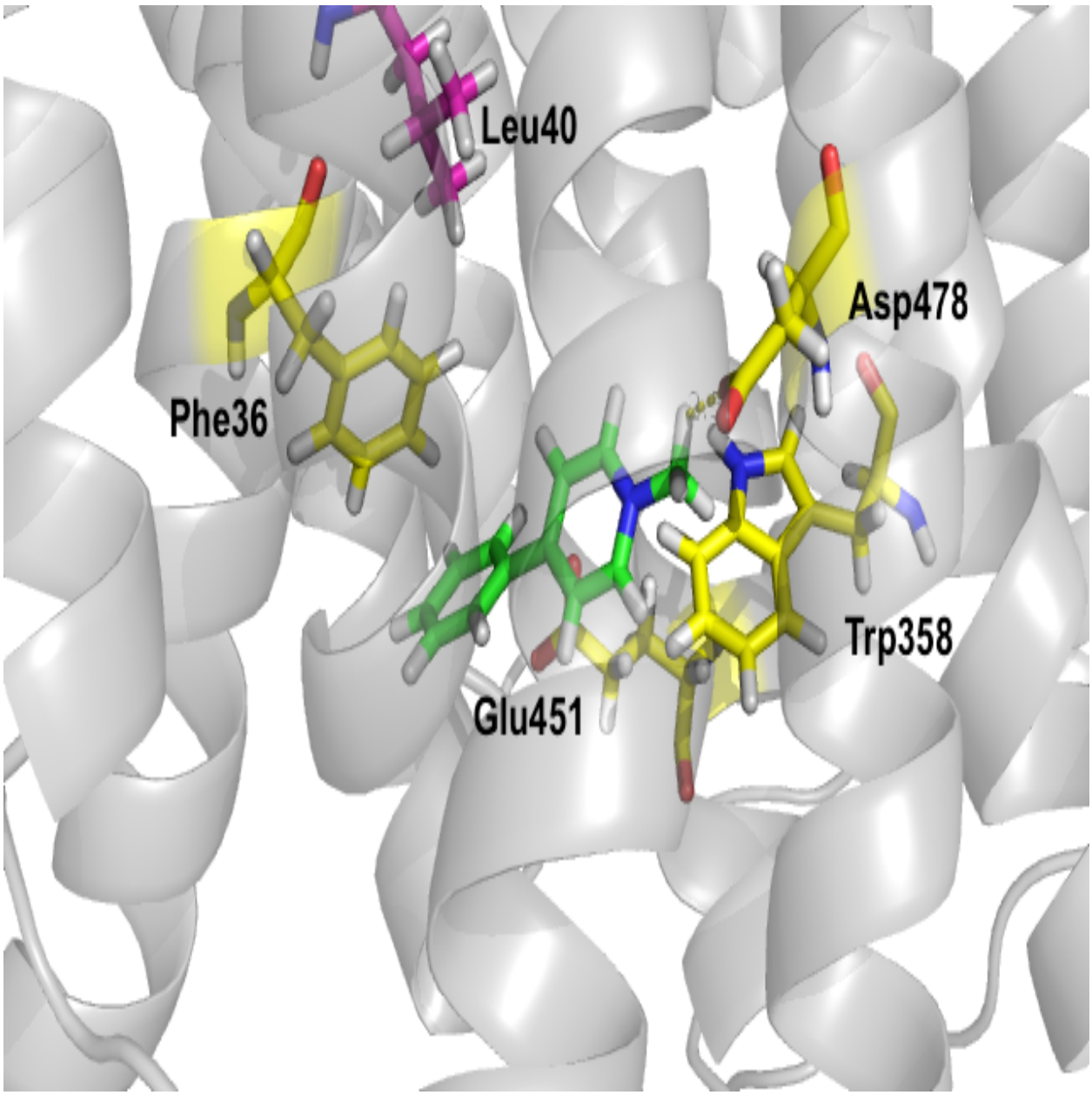

Figure 3.16 Structure of MPP^+ docked in hOCT3-Val40Leu mutant.

Structure of MPP^+ (green) docked in the substrate binding region of hOCT3-Val40Leu model. The ligand (green) and 'critical' amino acid residues (yellow) are displayed as sticks, as well as Leu40 (pink).

Table 3.10 MPP^+ docking result summary for hOCT3-Val40Leu.

Amino acid residue	Type of interaction
Phe36	Arene-H interaction
Trp358	Edge face interaction
Glu451	Edge face/arene-H interaction
Asp478	H-bond interaction

To determine the possible reason for loss of MPP^+ transport activity in non-functional hOCT3 mutants, MPP^+ was docked to the binding pocket of each mutant model, and residues interacting with the ligand were identified (Figure 3.17). Interestingly, similar patterns were observed for all three models. In the hOCT3-Val40Ala model, only Phe479 was identified to interact with MPP^+ through an arene-H interaction; in the hOCT3-Trp358Tyr model, only Phe359 was identified to interact with MPP^+ through an arene-H interaction; and in the hOCT3-Asp478Glu model, only Arg20 was identified to interact with MPP^+ through π-π stacking interaction (Figure 3.17). All other residues in the three binding pockets were either far apart from the ligand or only slightly interacting with MPP^+ in hydrophobic manners (Figure 3.17). None of these three 'critical' residues was predicted to be interacting with MPP^+ in the wild type hOCT3 model, and they are not part of the residues that form the binding pocket in the model, either. All three of the substituted residues were located farther away from MPP^+ (data not shown), and thus could not interact with the compound. Therefore, based on the models, amino acid substitutions that led to complete loss of MPP^+ transport activity changed the confirmation of MPP^+ binding pockets to a large extent and weakened the interacting strengths between residues and MPP^+.

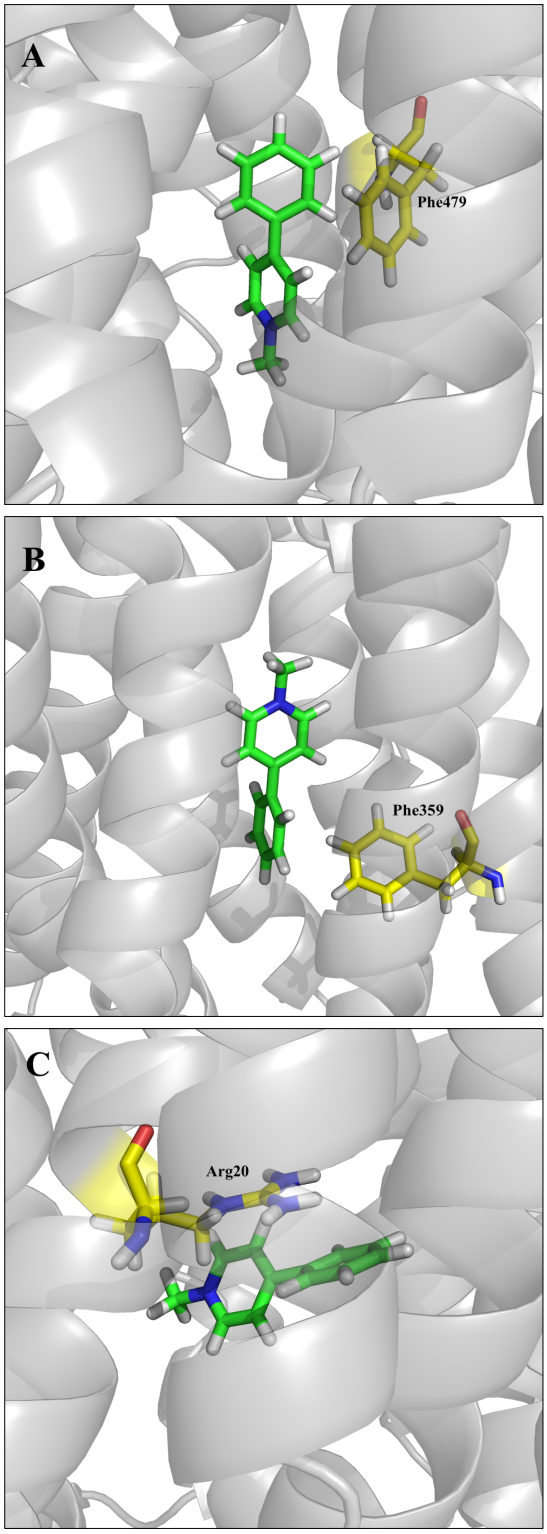

Figure 3.17 Structure of MPP^+ docked in non-functional hOCT3 mutants.

Structure of MPP^+ (green) docked in the substrate binding region of hOCT3-Val40Ala (A), hOCT3-Trp358Tyr (B), and hOCT3-Asp478Glu (C) models. The ligand (green) and 'critical' amino acid residues (yellow) are displayed as sticks.

3.4 Discussion

Recently, more and more attention has been paid to study the interactions between (as well as transport mechanism of) compounds with hOCT3 [1]. The possible physiological roles of hOCT3 (suggested to be related with prostate cancer, coronary heart disease, and obsessive compulsive behavior), the most widely expressed organic cation transporter (expressed in skeletal muscle, placenta, heart, brain, and many more tissues), as well as numerous studies about interactions between clinical therapeutics and hOCT3 justify the importance of this transporter and the need to study its working mechanism.

Due to the lack of an X-ray crystal structure of any member of the SLC22 family, generating a 3-D homology model for hOCT3 with a suitable template is of importance. Homology models of some other OCT transporters (rOct1, rOct2, rbOct2, and hOCT2) have been reported in the literature [40, 60-62]. *In vitro* experiments were conducted in these studies, and several amino acid residues that might be critical in terms of substrate and/or inhibitor interactions with these transporters have been identified (summarized in Table 1.3 together with residues identified using 2-D topology models of OCTs). The 3-D homology models for these OCT transporters, albeit ‘accurate’ at that time, are ‘out of date’ considering they were generated based on templates sharing lower sequence identities to OCT (LacY or GlpT).

Therefore, in the present study, a homology model for hOCT3 was generated using an inorganic phosphate transporter PiPT, recently identified as a superior template compared to LacY and GlpT, as the template [92]. Docking the model with a

prototypical OCT substrate, MPP^+, a binding pocket for MPP^+ that nested in the plasma membrane was identified, together with amino acids that formed the pocket (Figure 3.4).

Residues 'critical' for MPP^+-hOCT3 interactions were identified in this study, and a series of CHO cell lines stably expressing hOCT3 mutants ('critical' residues substituted) were established. Conservative substitutions at Trp358 and Asp478, along with non-conservative substitution at Val40, completely abolished the MPP^+ transport activity of mutant hOCT3. For mutants that still possess MPP^+ transport activity, we observed significantly increased K_m value for several hOCT3 mutants (hOCT3-Phe36Ala, hOCT3-Val40Leu, and hOCT3-Glu451Asp), indicating a decreased affinity between mutant transporters and MPP^+, and the residues identified are contributing to the interactions between MPP^+ and hOCT3. Substitutions (conservative and/or non-conservative) on all residues hypothesized to be critical in MPP^+-hOCT3 interactions led to significant changes in hOCT3 affinity to MPP^+, which demonstrates that our model is valid and could be used as guidance towards future mutational studies to learn about other hOCT3-ligand interactions. Cell lines with double mutant transporters were also generated, which resulted in one abolishment in MPP^+ transport (hOCT3-Phe36Tyr-Val40Leu), decreased transport affinity for one other double mutant (hOCT3-Val40Leu-Glu451Ala), and one double mutant with no significant affinity change (hOCT3-Phe36Tyr-Val40Leu). Based on these results, importance of each identified residue could be ranked: Trp358, Asp478 > Val40 > Phe36, Glu451.

In order to rule out the possibility that the loss of MPP^+ transport activity was due to failure of transfection, protein translation or targeting of transporter protein to plasma membrane, PCR and western blot assays were performed. Genomic DNA from non-

functional mutant cell lines was extracted and genomic integration of the intact cDNA for hOCT3 was confirmed using PCR and gel electrophoresis (Figure 3.14). Western blots of mutant transporter proteins (extracted from plasma membrane of the stably transfected cell lines) were performed, however, to date have been unsuccessful (Figure 3.15).

A 3-D homology model of one of the mutant transporters (hOCT3-Val40Leu) with decreased affinity for MPP^+ was generated using the same protocol. The same amino acids critical for MPP^+-hOCT3 interactions were identified in the mutant model, but interacts with MPP^+ were reduced, and Leu40 (the substituted residue) did not interact with the ligand. Homology models of hOCT3 mutants with no MPP^+ transport activity were also generated and docked with energy-minimized MPP^+. Interactions between MPP^+ and mutant binding pockets were predicted to be weaker compared to wild type hOCT3, and the conformation of binding pockets were altered due to residue substitution, which could be the reason for loss of ability to transport MPP^+. Docking the wild type hOCT3 model with ligands that are structurally divergent from MPP^+ suggested that substrates of hOCT3 with distinct structures interact with different residues inside one large binding pocket, and their individual regions may overlap.

Prior to constructing 3-D models for OCTs, 2-dimensional topology models of OCTs were used for transporter studies. In 1999, Koepsell's group identified residue Asp 475 as being involved with TEA^+ transport in rOct1 by mutating an acidic amino acid that is conserved in OCTs but not in OATs [57]. This negatively charged aspartate residue is located inside the binding pocket of our hOCT3 model (Figure 3.4, Figure 3.6) and identified to be interacting with a number of compounds in this study. In 2005, the

same group identified residues responsible for the discrepancy in corticosterone transport between rOct1 and rOct2 by introducing polypeptide stretches of rOct2 into rOct1, and exchanging amino acids between the two transporters (residues summarized in Table 1.3) [58]. Only one out of the three residues (Glu451) is located inside the binding pocket of our hOCT3 model; while the other two amino acids are both one residue apart from the opening of the pocket [58]. However, amino acids are not conserved between rOct1/rOct2 and hOCT3 in this area, and the affinity of hOCT3 to corticosterone is significantly higher compared with rOct1 (750 fold) and rOct2 (20 fold), so it is likely that the binding site for corticosterone in hOCT3 is different from that in rodent Octs [58].

With the generation of crystallized membrane transporters, in 2005, a 3-D homology model of rOct1 was developed using LacY as the template [40]. Popp et al. looked into eighteen consecutive amino acids on the fourth TMD in rat Oct1 by introducing mutations to these residues and testing changes in TEA^+ and MPP^+ transport activity in oocytes. Three residues were identified as critical for TEA^+ and MPP^+ uptake (Table 1.3) [40]. These residues are conserved in OCTs, however, are not part of the residues identified in this study that form the binding pocket for hOCT3. This information suggests that the binding pockets for rOct1 and hOCT3 are different, and could be supported by our study on one of these residues (hOCT3-Trp223Tyr mutant did not exhibit significant change in MPP^+ transport activity, data not shown).

In the same year, Zhang et al. conducted a study to identify amino acid residue(s) responsible for the difference of transport activity between rbOct1 and rbOct2 by mutating three residues that are conserved in OCT1 but not in OCT2, and the

glutamate residue (Glu451, conserved and identified in hOCT3 model) was identified to be involved with TEA^+-rbOct2 interactions [61].

A cysteine residue (Cys451) critical for choline transport activity in rOct2 was identified by Sturm et al. in 2007 [65]. This non-conserved residue in hOCT3 (Tyr454) was not identified as part of the binding pocket. However, since hOCT3 affinity for choline is very low, and we have already suggested that hOCT3 is likely to have a different binding pocket than rOct2, this residue discrepancy is not too surprising.

Following their previous work, Zhang et al. further elucidated hOCT2's structure by examining the accessibility of binding sites to hydrophilic thiol-reactive reagents [64]. Based on the homology model of rbOct2 built by the same group in a previous study, a 3-D homology model of hOCT2 (using GlpT as template) was generated [63, 64]. All cysteine residues in TMDs 10 and 11 were mutated and tested for transport activity changes (using TEA^+) as well as accessibility to biotin [64]. Results showed that only Cys474 is exposed to the extracellular aqueous environment, and 'participates in forming a transport pathway for TEA^+' [64]. The homology model in their study was in an inward-open facing state, unlike our model for hOCT3, which is in an occluded state [64]. So it is possible that this water accessible cysteine residue is buried inside transmembrane domains when the model is in an occluded state (when a substrate is covered by residues in the binding pocket). Thus, even though this conserved cysteine residue (Cys450) was not identified in our hOCT3 model, it is possible that it could be interacting with TEA^+ (e.g. during substrate recognition), and this can be tested through further mutational studies in hOCT3.

No residue that is subject to non-synonymous SNP has been identified to be responsible in forming the binding pocket of hOCT3, however, one of the naturally occurring SNPs, Gly475Ser, is located close to the binding pocket (one amino acid away) [22]. Thus this residue substitution has the possibility of changing the conformation of the binding pocket and altering the binding affinities for certain compounds, which needs to be investigated.

In summary, a 3-D homology model of hOCT3 was successfully generated. A ligand binding pocket, as well as residues that form the pocket, were determined. Residues related to MPP^+ transport were confirmed by conducting uptake assays for respective mutants. 3-D homology models for four hOCT3 mutants were generated, and interacting residues were identified through docking with MPP^+. These results suggest that hOCT3 substrates with different structures bind to different regions in one large binding pocket, and residues directly interacting with ligands may overlap. Further, loss of transport activity for MPP^+ could be explained by lack of strong interactions between ligand and binding pocket residues. Comparison between our hOCT3 model and early OCT models indicates that the binding pockets of OCTs likely are not the same, although similarities do exist. These results and information about ligand binding in hOCT3 could someday be utilized to help with the development of potent substrates and/or inhibitors, as well as with the study of transport mechanisms.

Chapter 4

SPECIES COMPARISON OF ORGANIC CATION TRANSPORTER 3 THROUGH HOMOLOGY MODELING

4.1 Introduction

In addition to humans, organic cation transporter 3 is also found in other species including mouse and rat, and plays similar roles in these species as well. OCT3/Oct3 orthologs from human, rat, and mouse share a great deal of similarities including tissue distribution, operating mechanism, substrates, inhibitors, and so on, which is likely explained by the high sequence identity (and similarity) between the orthologs (with 87% between human and mouse OCT3/Oct3 and 86% between human and rat OCT3/Oct3) [1]. Despite these similarities, differences do exist; for example, rodent Oct3s are detected in some tissues where hOCT3 is not expressed (large intestine, spleen, thymus) and interacting characteristics for some molecules with OCT3 orthologs can be quite diverse (as shown in Table 1.4). Utilizing transporter-substrate/inhibitor affinity differences, OCT3 orthologs from different species can be distinguished [1].

Even though the differences between transporter sequences are trivial, they could lead to diverse confirmations of the transporters, which might completely differentiate transport abilities among the three species, or differences between the binding sites of the transporters. Both of these might be the cause of different molecule-transporter interacting profiles. Considering the fact that OCT3 transport profiles of

different species are not completely distinct, the affinities between transporters and substrates/inhibitors are only significantly different in a few of the compounds, it is likely that the conformations for these orthologs are similar, with only the binding pockets exhibiting a few discrepancies.

To test the hypothesis that the inter-species differences between human, mouse, and rat OCT3 orthologs are due to differences in their binding regions, homology models of mOct3 and rOct3 were built utilizing the same template (PiPT) and compared with the model of hOCT3. Compounds with significantly different affinities for these transporters were docked into the models; both the binding pockets and interacting residues were compared among species.

4.2 Methods

3-D homology models of mouse and rat Oct3 were generated based on the crystal structure of a eukaryotic inorganic phosphate transporter (PiPT) [92]. PiPT is a membrane of the phosphate: H^+ symporter family of MFS. Similar to the SLC22 family, PiPT also contains 12 TMDs and intercellular termini, the 12 TMDs of PiPT are divided into two parts with 6 helices each (N and C domain), where the two parts are connected by a large intracellular loop [92]. The crystal structure of PiPT (PDB ID: 4J05) was solved in complex with its substrate, inorganic phosphate, by Pedersen et al. at a resolution of 2.9 Å in an occluded conformation [92, 95]. The structure of PiPT is currently recommended as the best template for OCTs and OATs because it is a crystallized transporter sharing the most sequence similarity with the human solute carrier group at this time, it possesses similar structure compared with OCTs (previous

OCT templates do not contain the large intracellular loop), crystallized in an occluded state (could provide more information for compound docking), and PiPT is more evolutionarily close to OCTs. Based on all this information, we are choosing it as the template to generate models for mouse and rat Oct3 [56].

Sequences of mouse and rat Oct3 were obtained from Universal Protein Resource database (UniProt, accession code: Q9WTW5, O88446), and the sequence of PiPT was downloaded from PDB in a fasta file (4J05) [95, 104, 105]. The template and target (mOct3 and rOct3) sequences were aligned with ClustalX followed by manual adjustments based on the TMDs observed in PiPT structure and predicted for rodent Oct3s using ICM Browser (Molsoft LLC) and Phobius (Stockholm Bioinformatics Center), the result of alignment is shown in Figure 4.1 [53, 96, 97]. The extracellular loop of PiPT was not part of the crystallization, and thus was not contained in the sequence of the PDB file; the extracellular and intracellular loops between TMDs 1, 2 and 6, 7 of OCT3 were truncated because no corresponding residues were modeled in the crystal structure of PiPT.

Then, one hundred 3-D homology models of both mOct3 and rOct3 were generated based on the alignment result and the crystal structure of PiPT (downloaded from PDB) using the MODELLER software (University of California at San Francisco, San Francisco, CA) [54]. A DOPE score was automatically calculated for each model, and it was used to evaluate the quality of a structure model as a whole. Stereochemical quality of a 3-D protein model was checked using the PROCHECK function, which produces a Ramanchandran plot that helps visualize energetically allowed regions, and analyzes the residue-by-residue geometry of a model. A model with more than 90% of

amino acids located in the favorable regions of a Ramanchandran plot is generally considered as an acceptable model. The binding pockets of mOct3 and rOct3 for specific docking compound(s) were identified using GOLD suite 5.4 by docking a compound into a 12-Å sphere surrounding residue Asp478 (critical residue identified in earlier studies) [57]. Docking was performed by first energy-minimizing the docking compound (substrates and inhibitor for OCT3, including MPP^+, procainamide, or norepinephrine, chemical structures shown in Figure 4.2) using Tripos force field with Gasteiger-Hückel charges in SYBYL X, and then inserted the compound with 10 poses into the pre-defined sphere for each of the one hundred models using GOLD [26, 27, 70, 73, 95, 98]. GOLD's default scoring function was used to determine the best ligand binding mode (pose), then potentially important amino acid residues were identified by analyzing the structure within the binging pocket as well as binding interaction energies.

Figure 4.1 Sequence alignment of PiPT, mOct3 and rOct3.

Asterisks (*) indicate residues that are the same between the template and the target; colons (:) represent residues that are highly conserved between the sequences; periods (.) represent residues that are weakly conserved between the sequences; and blanks indicate that the residues are different.

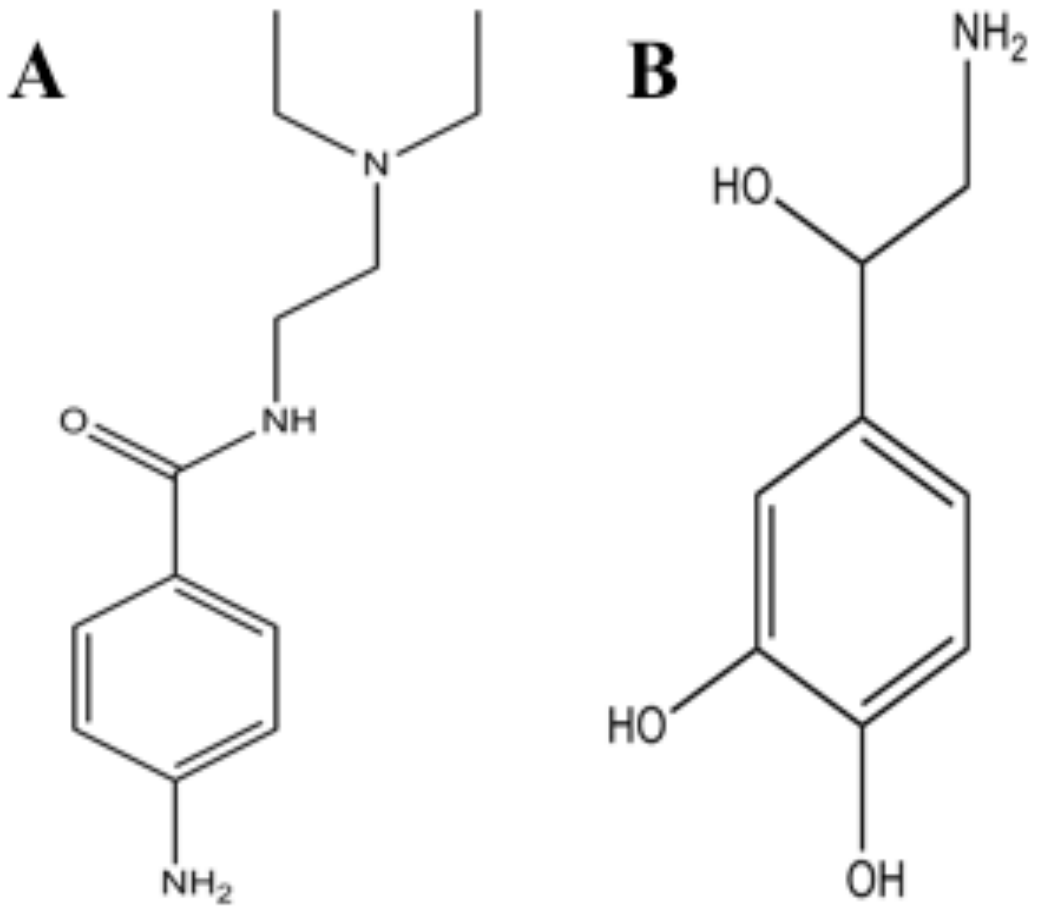

Figure 4.2 Structures of docking compounds for species differentiation.

Structures of other docking compounds procainamide (A) and norepinephrine (B) are displayed, respectively.

4.3 Results

4.3.1 Homology modeling of mouse organic cation transporter 3

GOLD scores of the top ten docked poses of MPP^+ in the binding pocket of mOct3 are summarized in Table 3.6 along with their corresponding DOPE scores. The largest GOLD score represents the best docking pose, and the smallest DOPE score demonstrates the best homology model. Since our focus was on the binding interaction between docking substrate and mOct3, our model selection criteria was primarily based on the GOLD score, and Model 5 had a significantly higher GOLD score compared to other models. Comparing the DOPE scores of these models with top GOLD scores, we noticed that even though Model 5 did not have the lowest score, the value was acceptable and lower than most of the other top ranked models. Thus we chose Model 10 as our best 3-D homology model for mOct3. Visualizing the generated homology model for mOct3 in Pymol, we were able to identify all the amino acid residues surrounding and forming the large binding pocket for MPP^+ in the transporter. The generated 3-D homology model along with the amino acid residues forming the MPP^+ binding pocket are depicted as yellow sticks (Figure 4.3). These residues are from different transmembrane domains that intertwine and form the binding region for MPP^+: TMD 1 (Arg19, Arg20, Leu23), TMD 2 (Leu158, Leu161), TMD 4 (Met219, Thr220, Val223), TMD 5 (Met243), TMD 7 (Phe354, Val358), TMD 10 (Tyr449, Leu450, Ser453), and TMD 11 (Ser466, Gly470, Leu471, Asp473, Phe474, Ile477, Phe481) (Figure 4.3).

PROCHECK analysis of the selected mOct3 model generated its Ramachandran plot (Figure 4.4). Ramachandran plot provides a way to visualize energetically allowed

regions for backbone torsion angles psi against phi of amino acid residues in protein structure; the plot demonstrates the empirical distribution of data points (amino acid residues) observed in a single structural model. For this mOct3 model, 91.9% of amino acids were in the most favored region, 4.5% in the additional allowed region, and only a total of 3.6% in the generously and disallowed region. Also, amino acids in the disallowed region were located far away from the putative binding region (Figure 4.4). These observations imply that the structure of our model for mOct3 is plausible.

Table 4.1 GOLD and DOPE scores for mOct3.

Model identifier	GOLD score	DOPE score
Model 5	52.73	-47491.777
Model 39	49.98	-47725.219
Model 95	49.27	-46448.785
Model 59	49.17	-47334.730
Model 81	48.89	-47610.613
Model 67	48.55	-47504.059
Model 79	48.21	-48019.738
Model 36	47.57	-47617.582
Model 83	46.71	-47378.906
Model 12	46.63	-47413.473

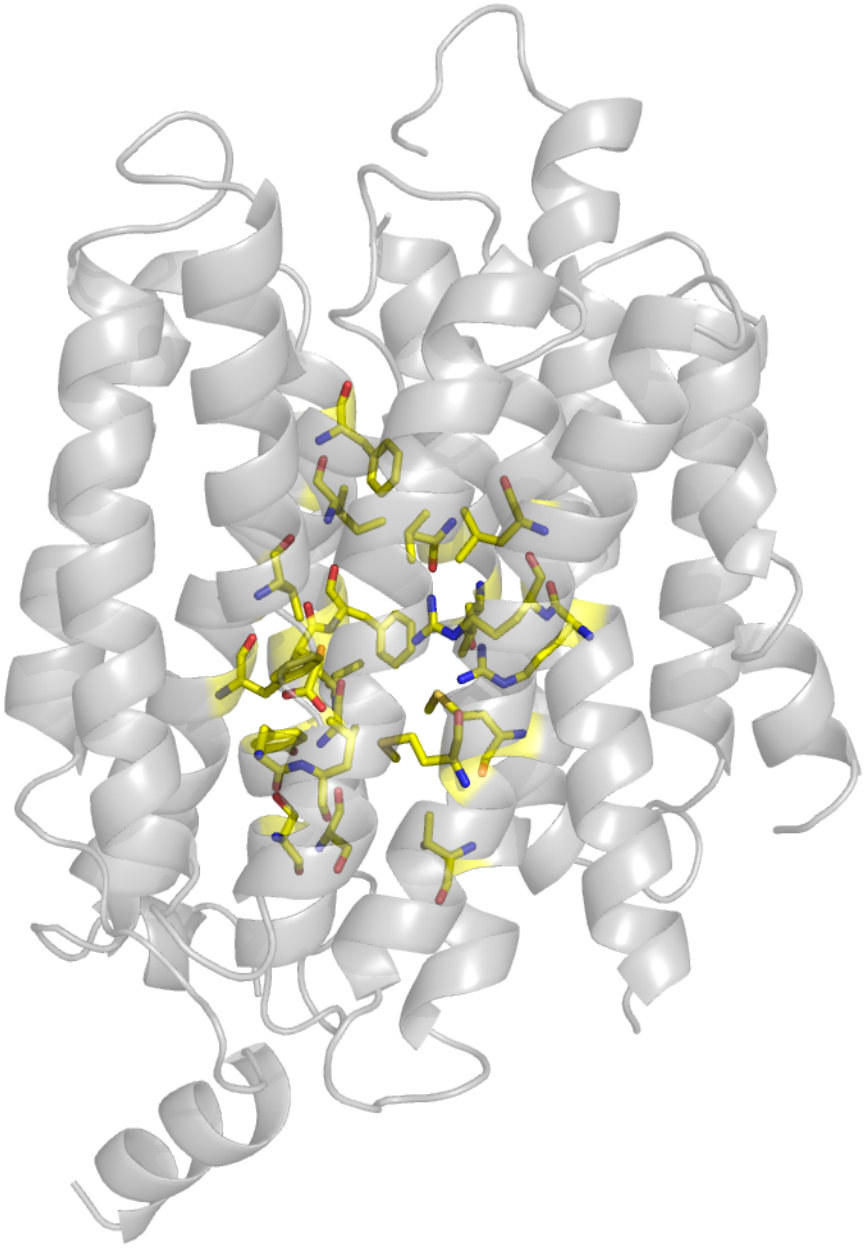

Figure 4.3 3-D demonstration of binding pocket for MPP^+ in mouse Oct3.

Residues (yellow) surrounding the binding pocket are depicted in sticks.

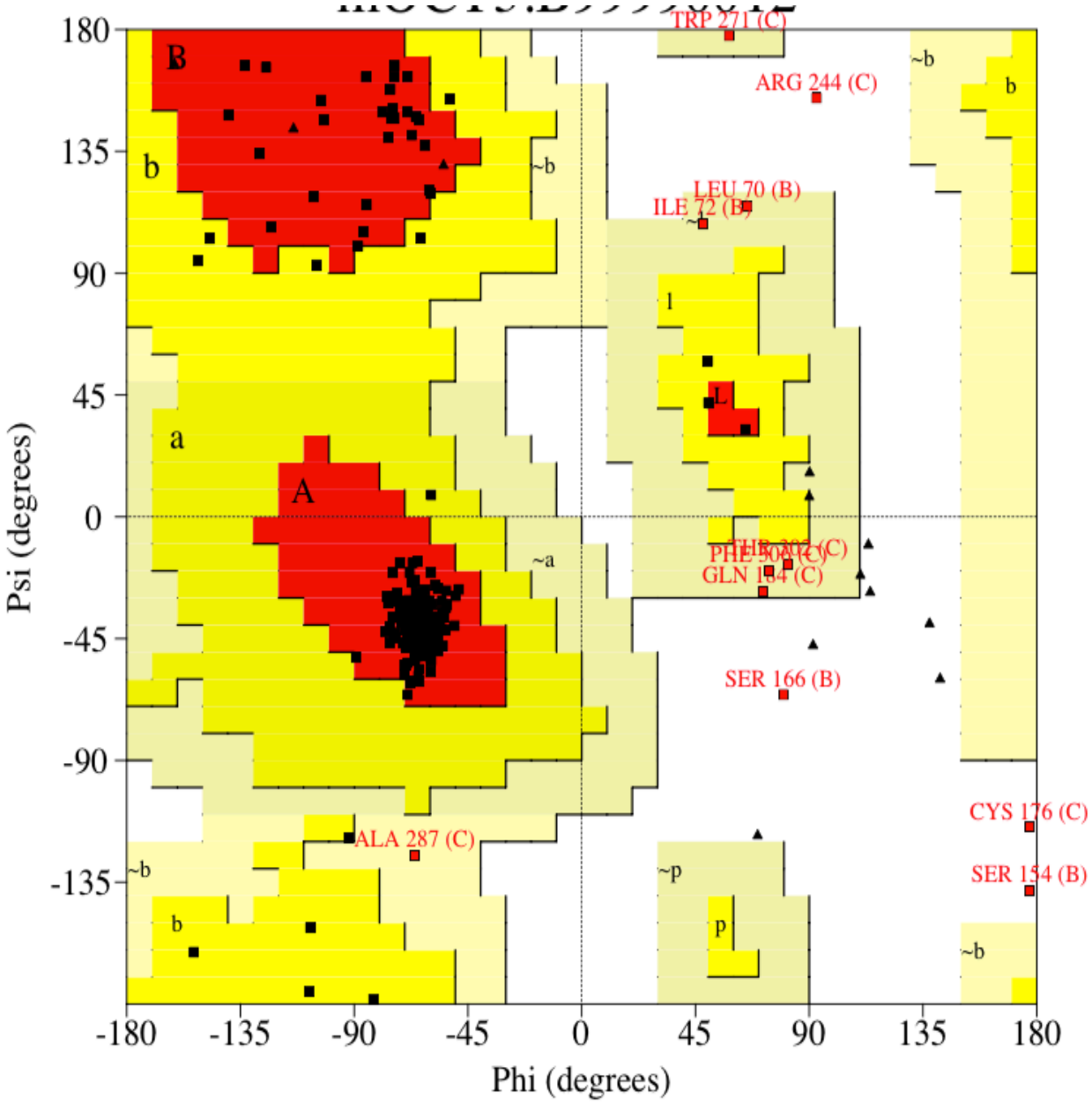

Figure 4.4 Ramachandran plot of mouse Oct3.

Phi and psi indicate backbone conformation torsion angles of amino acid residues, which represent the rotations of a polypeptide main chain N-Cα and Cα-C bonds. Amino acids are laid out in different regions: most favored region (red), additional allowed region (yellow), generously allowed region (light yellow), and disallowed region (white). Residues depicted in red squares are in the generously allowed and disallowed regions.

To determine and compare the interactions between MPP^+ and mOct3 with those in hOCT3, MPP^+ was energy minimized in SYBYL X using Tripos force field with Gasteiger-Hückel charges and docked to the binding pocket of the mOct3 model to identify amino acid residues critical for MPP^+-mOct3 interactions in GOLD suite 5.4.

From the docking result, the aromatic ring of MPP^+ was located in between the aromatic rings of two residues, Arg20 and Phe474, in π-π stacking and edge face interactions (Figure 4.5). Moreover, the pyridinium ring and the benzene ring of MPP^+ were seen to be adjacent to and interacting with Met219, Leu450, Asp473, and Ile477 in hydrophobic manners (Figure 4.5). Identified residues as well as their interaction types are summarized in Table 4.2.

Comparing the residues directly interacting with MPP^+ from both hOCT3 and mOct3 models, we observed that only one amino acid (Asp473) was detected in both models, albeit with different interaction types. We did not detect any ionic salt-bridge interaction resulting from residues in the binding pocket of mOct3; however, a number of other interactions related to the aromatic rings of MPP^+ were observed (π-π stacking, edge face, and hydrophobic interactions). Thus, the binding pockets for MPP^+ in hOCT3 and mOct3 are not the same, but do contain some level of similarity (one common residue as well as similar interaction types).

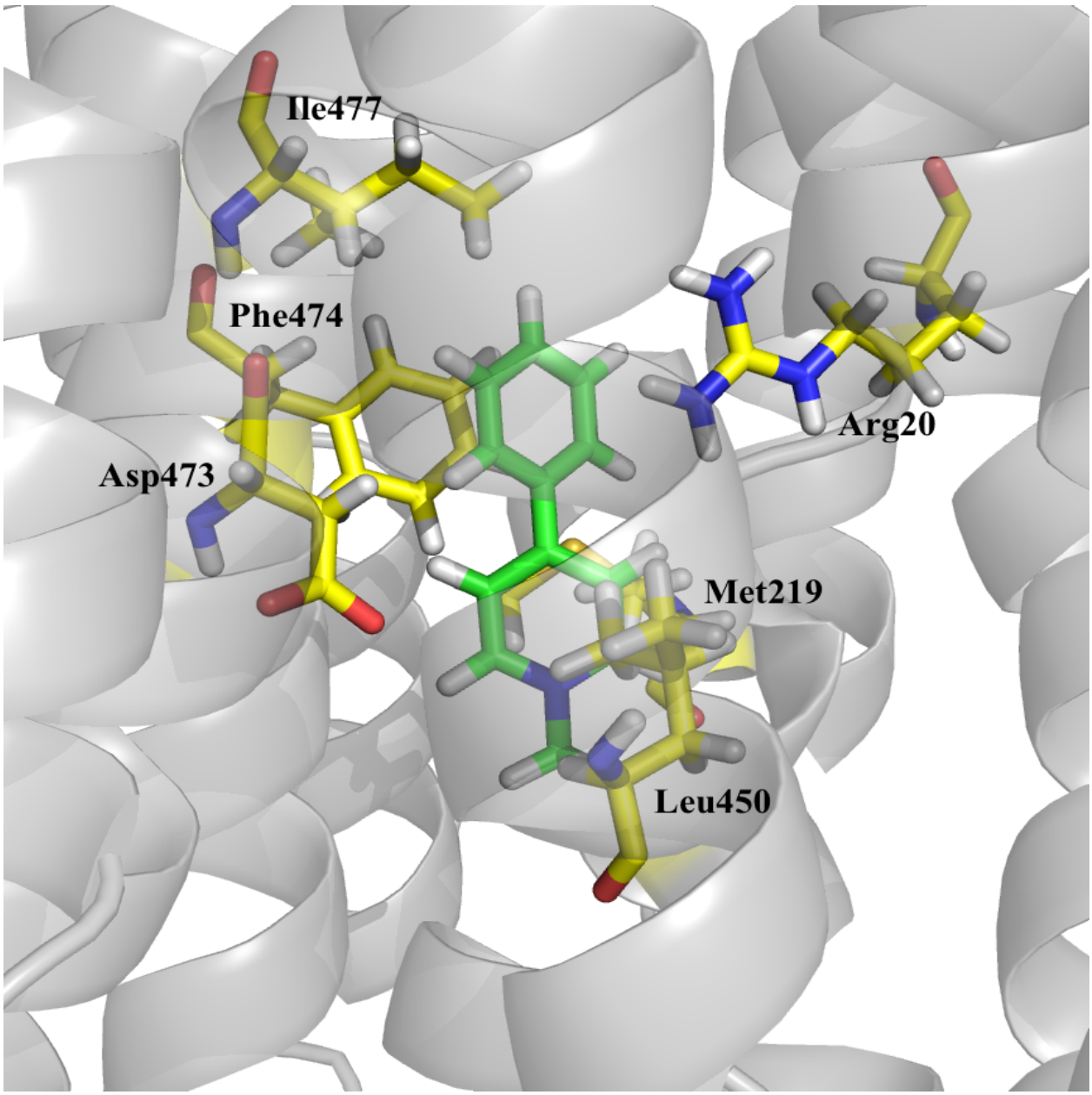

Figure 4.5 Structure of MPP^+ docked in the substrate binding region of mOct3.

The ligand (MPP^+, green) and 'critical' amino acid residues (yellow) are displayed as sticks.

Table 4.2 MPP^+ docking result summary for mOct3.

Amino acid residue	Type of interaction
Arg20	π-π stacking interaction
Met219	Hydrophobic interaction
Leu450	Hydrophobic interaction
Asp473	Hydrophobic interaction
Phe474	Edge face interaction
Ile477	Hydrophobic interaction

4.3.2 Homology modeling of rat organic cation transporter 3

GOLD scores of the top ten docked poses of MPP^+ in the binding pocket of rOct3 are summarized in Table 4.3 along with their corresponding DOPE scores. The largest GOLD score represents the best docking pose, and the smallest DOPE score demonstrates the best homology model. Since our focus was on the binding interaction between docking substrate and rOct3, our model selection criteria was primarily based on the GOLD score, and Models 62 and 68 had significantly higher GOLD scores compared to other models. Comparing the DOPE scores of these models with top GOLD scores, we chose Model 68 as our best 3-D homology model for rOct3 since its DOPE score was significantly smaller than that of Model 62. Visualizing the generated homology model for rOct3 in Pymol, we were able to identify all the amino acid residues surrounding and forming the large binding pocket for MPP^+ in the transporter. The generated 3-D homology model along with the amino acid residues forming the MPP^+ binding pocket are depicted as yellow sticks (Figure 4.6). These residues are from different transmembrane domains that intertwine and form the binding region for MPP^+: TMD 1 (Arg16, Arg19, Arg20), TMD 2 (Asn157, Phe160), TMD 4 (Trp218, Phe222), TMD 5 (Gln242, Phe245), TMD 7 (Trp353, Ser356, Ala357, Tyr360, Gln361), TMD 10 (Glu446, Val448, Tyr449), and TMD 11 (Cys472, Asp473, Gly476) (Figure 4.6).

PROCHECK analysis of the selected rOct3 model generated its Ramachandran plot (Figure 4.7). Ramachandran plot provides a way to visualize energetically allowed regions for backbone torsion angles psi against phi of amino acid residues in protein structure; the plot demonstrates the empirical distribution of data points (amino acid residues) observed in a single structural model. For this rOct3 model, 91.9% of amino

acids were in the most favored region, 4.9% in the additional allowed region, and only a total of 3.3% in the generously and disallowed region. Also, amino acids in the disallowed region were located far away from the putative binding region (Figure 4.6). These observations imply that the structure of our model for mOct3 is plausible.

Table 4.3 GOLD and DOPE scores for rOct3.

Model identifier	GOLD score	DOPE score
Model 62	51.59	-47000.965
Model 68	51.48	-47760.391
Model 80	51.00	-47873.797
Model 93	49.31	-47250.766
Model 66	48.78	-47145.648
Model 42	48.68	-47086.980
Model 71	48.46	-47528.285
Model 16	48.26	-47610.598
Model 38	48.00	-47118.887
Model 34	47.36	-47253.957

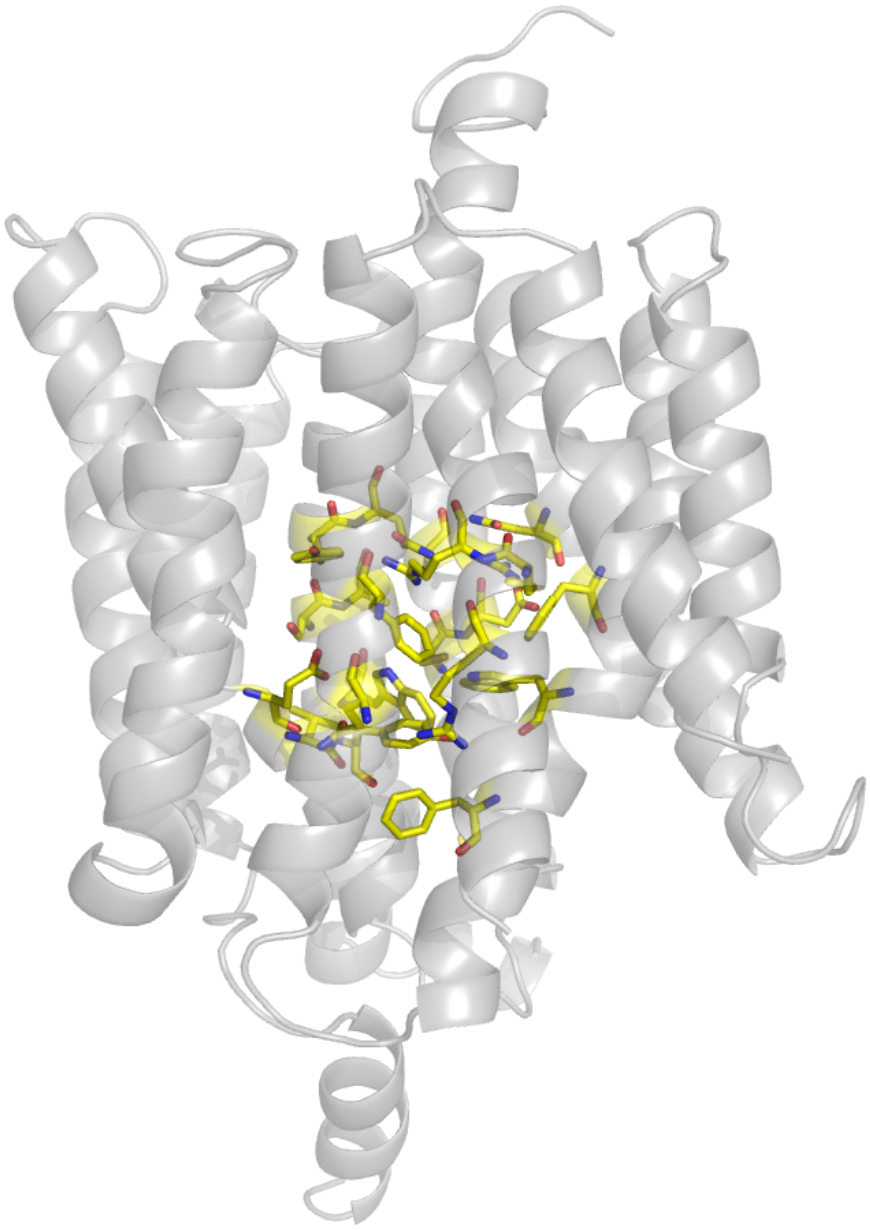

Figure 4.6 3-D demonstration of binding pocket for MPP^+ in rat Oct3.

Residues (yellow) surrounding the binding pocket are depicted in sticks.

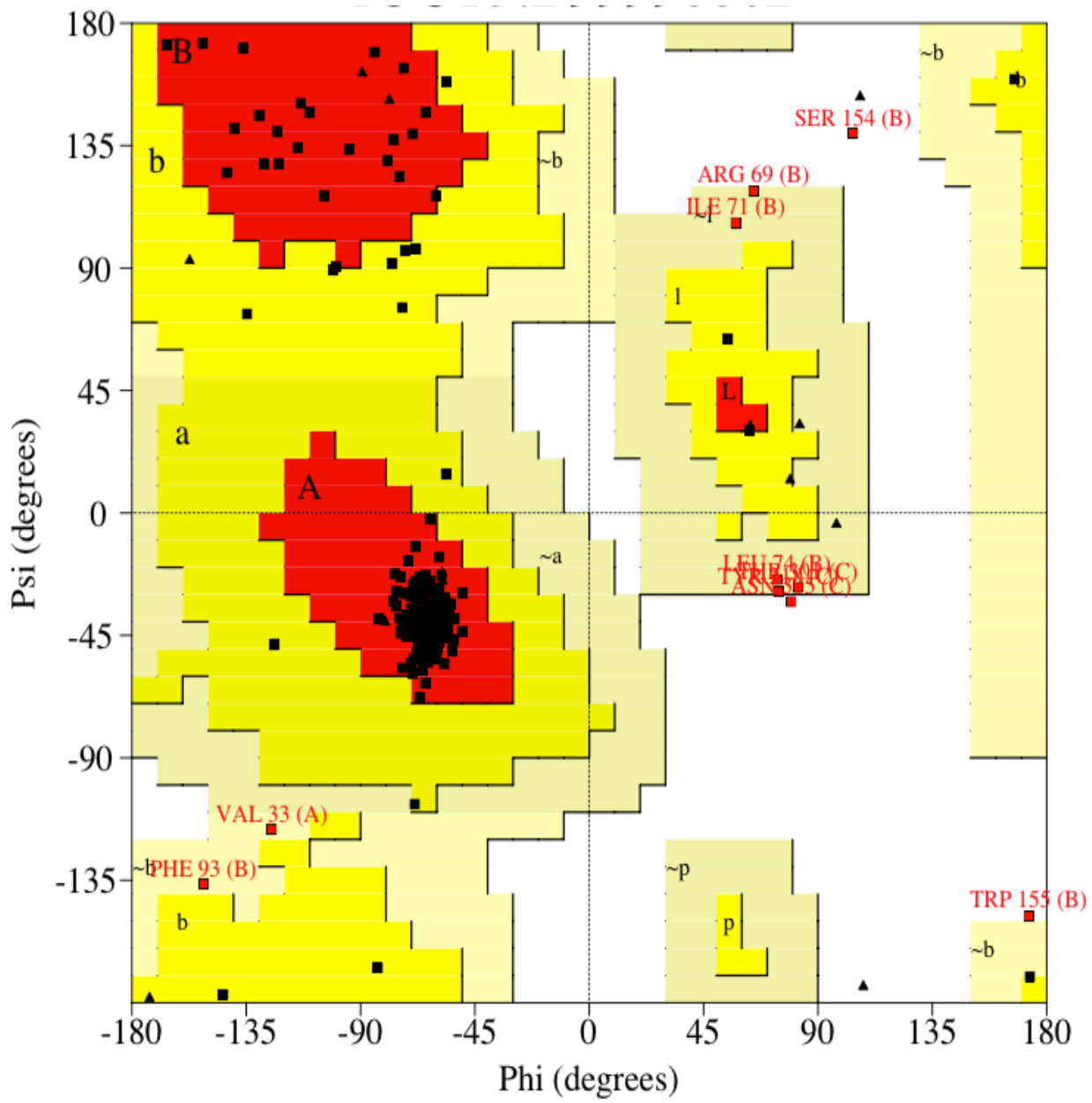

Figure 4.7 Ramachandran plot of rat Oct3.

Phi and psi indicate backbone conformation torsion angles of amino acid residues, which represent the rotations of a polypeptide main chain N-Cα and Cα-C bonds. Amino acids are laid out in different regions: most favored region (red), additional allowed region (yellow), generously allowed region (light yellow), and disallowed region (white). Residues depicted in red squares are in the generously allowed and disallowed regions.

To determine and compare the interactions between MPP^+ and rOct3 with those in hOCT3, MPP^+ was energy minimized in SYBYL X using Tripos force field with Gasteiger-Hückel charges and docked to the binding pocket of the rOct3 model to identify amino acid residues critical for MPP^+-rOct3 interactions in GOLD suite 5.4.

From the docking result, the aromatic rings of MPP^+ were detected to be related to the aromatic rings of residues Try218, Phe245, and Tyr449 (Figure 4.8). Moreover, the pyridinium ring of MPP^+ was observed to be interacting with the positively charged part of Arg20 in π-cation interaction, with Glu446 in polar-nonpolar interaction, and with Phe160 in a hydrophobic manner (Figure 4.8). These interactions are summarized in Table 4.4.

Comparing the residues that were identified to be directly interacting with MPP^+ from both hOCT3 and rOct3 models, we observed that only one amino acid (Glu446) was detected in both models, albeit with different interaction types. We did not detect any ionic salt-bridge interaction resulting from residues in the binding pocket of rOct3, however, a number of other interactions related to the aromatic rings of MPP^+ were observed (π-π stacking, edge face, π-cation, polar-nonpolar, and hydrophobic interactions). An interesting observation was that the conserved aspartate residue (Asp473) in the hOCT3 and mOct3 models was not identified as 'critical' in the rOct3 model. These results suggest that the binding pockets for MPP^+ in hOCT3 and rOct3 are not the same, but do contain some level of similarities (one common residue as well as similar interaction types). Taking this to the next step, we compared 'critical' residues for MPP^+ interactions from the two rodent Oct3 models. Only one amino acid (Arg20) was detected in both models with different interaction types, and the other 'critical'

residues as well as their interaction types were dissimilar (despite one phenylalanine residue at different locations from both models). Thus, the binding pockets for MPP^+ in mOct3 and rOct3 are also unique, but do contain some level of similarity. This is an interesting observation considering the high level of sequence similarities between mouse and rat Oct3.

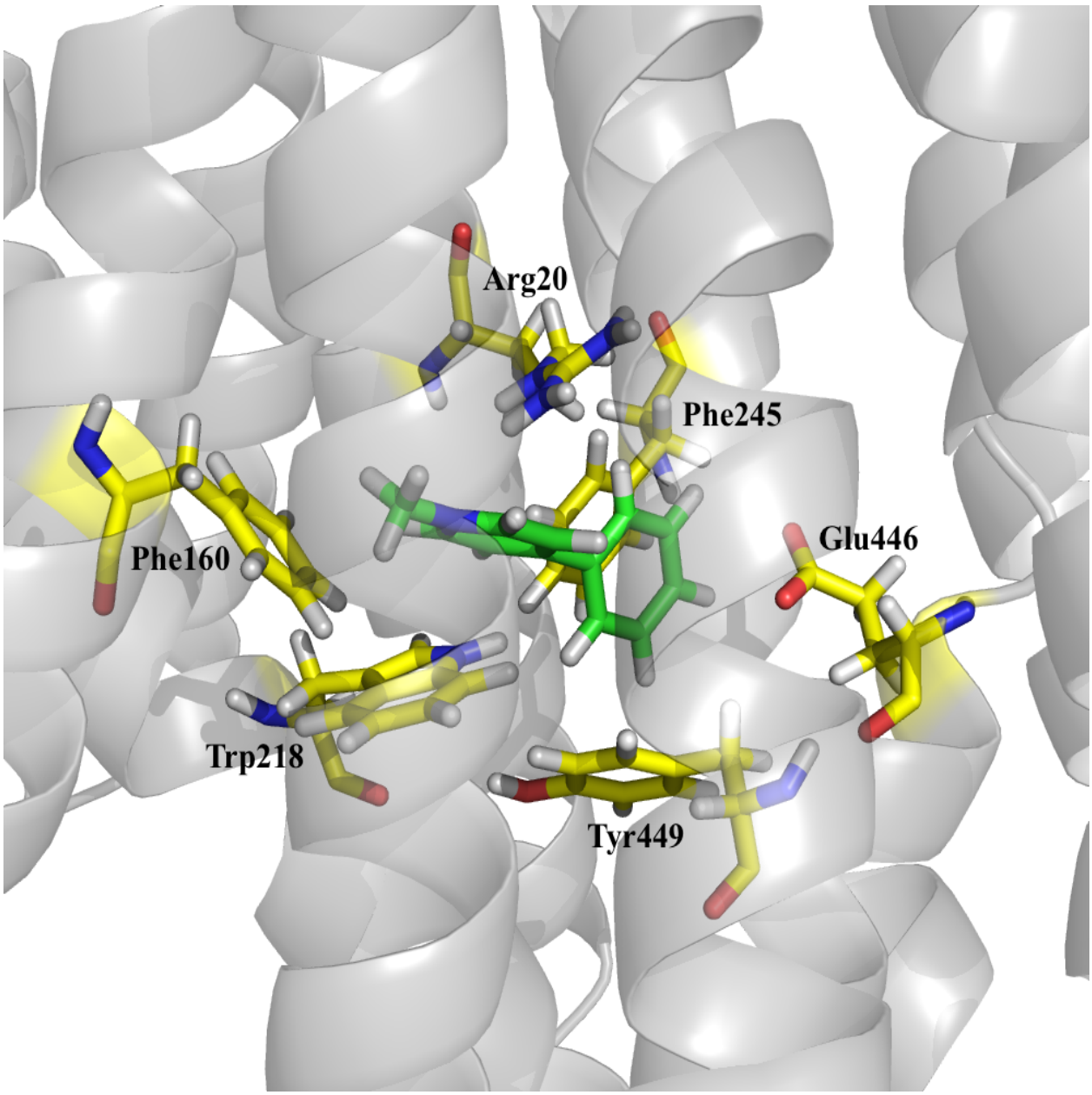

Figure 4.8 Structure of MPP^+ docked in the substrate binding region of rOct3.

The ligand (MPP^+, green) and 'critical' amino acid residues (yellow) are displayed as sticks.

Table 4.4 MPP^+ docking result summary for rOct3.

Amino acid residue	Type of interaction
Arg20	π-cation interaction
Phe160	Hydrophobic interaction
Try218	π-π interaction
Phe245	Edge face interaction
Glu446	Polar-nonpolar interaction
Tyr449	Edge face interaction

4.3.3 Comparison of transporters among species

To test the hypothesis that species differences in OCT3/Oct3 transporter affinity are due to sequence differences in the substrate binding pocket, ligands with significantly different binding affinities for OCT3 orthologs were docked to the binding pockets of human, mouse and rat OCT3/Oct3.

For the comparison between hOCT3 and mOCT3, energy-minimized procainamide (low affinity inhibitor for hOCT3 and high affinity inhibitor for mOct3) was utilized, and residues involved with transporter-procainamide interactions were identified (Figure 4.9), along with their specific interaction types (Table 4.5). Comparing identified residues from both transporters, we observed two residues from hOCT3 that are interacting with procainamide and four residues from mOct3 responsible for procainamide-transporter interactions. One common residue (aspartate) was detected in both models, and in both scenarios this residue was interacting with a positively charged nitrogen atom in procainamide through an ionic salt-bridge interaction. Measured distances between the positively and negatively charged atoms in both models showed that the ionic interaction in mOct3 is stronger (shorter distance, data not shown). The other residue (Phe165) identified in hOCT3 was interacting with the ligand through an arene-H interaction, and this type of interaction was also observed in the mOct3 model (Val223). Two other residues in the binding pocket of mOct3 were also detected and acted as side-chain acceptors for procainamide. Thus, critical residues in mOct3 are more closely situated to the ligand and exerting stronger and more interactions.

Comparing the residues responsible for transporter-procainamide interactions from both hOCT3 and mOCT3 models with residues that form the binding pocket for MPP^+ in both models, we observed that these procainamide-interacting residues are located in the binding pockets for MPP^+, but not necessarily contributing to the interactions between transporters and MPP^+: aspartate residues interacting with MPP^+ were demonstrated to be interacting with procainamide as well, but the interaction type in mOct3 model was different from the type in hOCT3 model. This result suggests that OCT3-interacting compounds (inhibitor in this case) with different chemical structures may share the same binding region, but residues directly interacting with them are likely different (with some overlap).

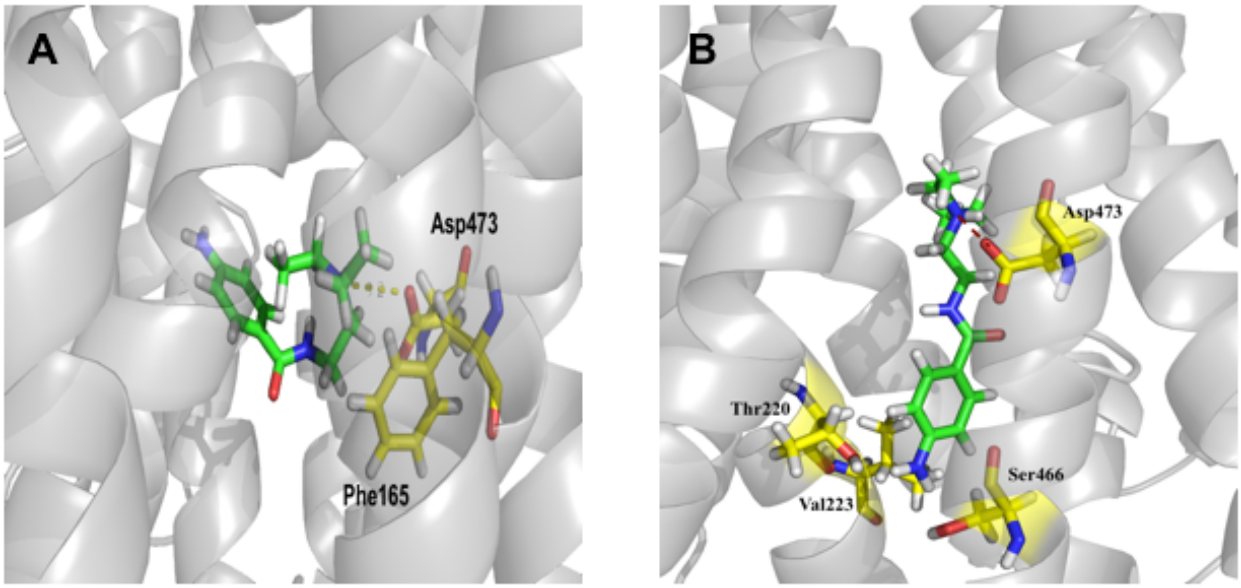

Figure 4.9 Structure of procainamide docked in the substrate binding region of OCT3.

The ligand (procainamide, green) docked in models of hOCT3 (A) and mOct3 (B), as well as 'critical' amino acid residues (yellow) are displayed as sticks. The dashed line indicates ionic salt-bridge interaction between the protonated amine of procainamide and the negatively charged residue Asp478 (Asp473 in mOct3).

Table 4.5 Procainamide docking result summary for human OCT3 and mouse Oct3.

Transporter	Amino acid residue	Type of interaction
hOCT3	Phe165	Arene-H interaction
	Asp478	Ionic salt-bridge interaction
mOct3	Thr220	Side-chain acceptor
	Val223	Arene-H interaction
	Ser466	Side-chain acceptor
	Asp473	Ionic salt-bridge interaction

For the comparison between hOCT3 and rOCT3, energy-minimized norepinephrine (low affinity substrate for hOCT3 and high affinity inhibitor for rOct3) was utilized, and residues involved with ligand-transporter interactions were identified (Figure 4.10), along with their specific interaction types (Table 4.6). Comparing identified residues from both transporters, we observed three residues from hOCT3 that are interacting with norepinephrine and six residues from rOct3 responsible for norepinephrine-transporter interactions. The same common residue (aspartate) was again detected in both models, and in both scenarios, this residue was acting as a side-chain acceptor towards the docked compound. The other residues identified in hOCT3 were interacting with norepinephrine through arene-H interaction and as a side-chain acceptor. Five other residues in the binding pocket of rOct3 were also detected and acted either as side-chain donors for norepinephrine or interacted with the compound due to aromatic rings. Thus, there are more critical residues in rOct3 interacting with norepinephrine, and the types of interactions (for example π-π interaction) are stronger compared to that of the hOCT3 model.

Comparing the residues responsible for transporter-norepinephrine interactions from both hOCT3 and rOCT3 models with residues that form the binding pocket for MPP^+ in both models, we observed that these norepinephrine-interacting residues are located in the binding pockets for MPP^+, but not necessarily contributing to the interactions between transporters and MPP^+. The aspartate residue interacting with MPP^+ was demonstrated to be interacting with norepinephrine as well, but the interaction type in rOct3 model was different from the type in hOCT3 model. The phenylalanine residue (Phe36) was demonstrated to be interacting with both MPP^+ and

norepinephrine in hOCT3 through different types of interactions. Arg20 (with different interaction types) and Trp218 (with the same type of interaction) were demonstrated to be interacting with both MPP^+ and norepinephrine in rOct3. These results further suggest that OCT3-interacting compounds with different chemical structures may share the same binding region, but residues directly interacting with them are likely different (with some overlap).

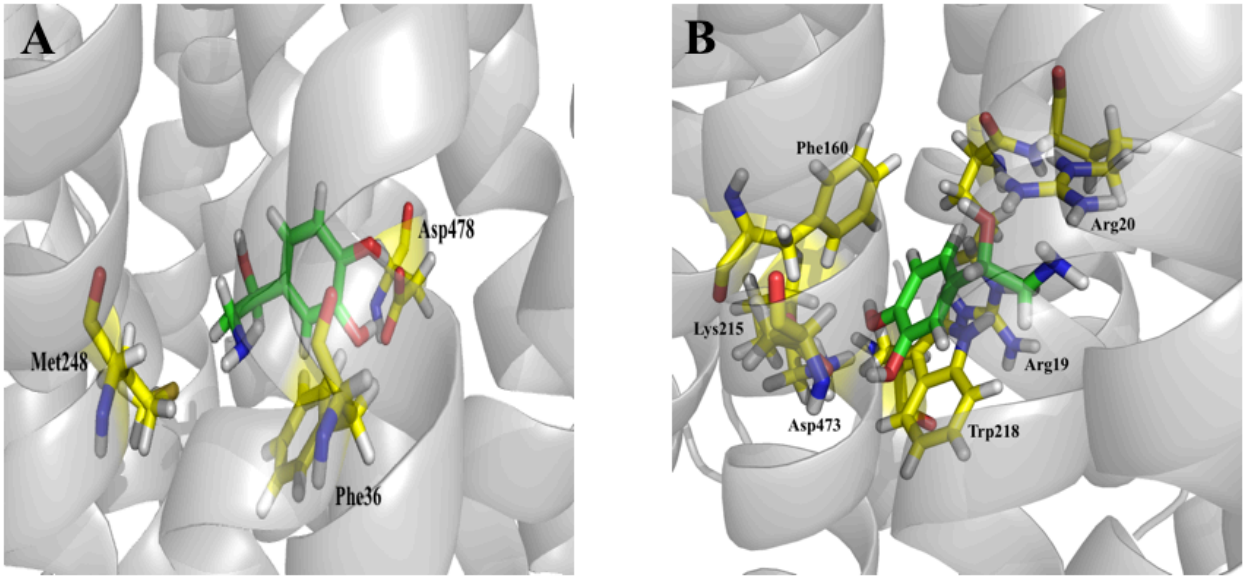

Figure 4.10 Structure of norepinephrine docked in the substrate binding region of OCT3.

The ligand (norepinephrine, green) docked in models of hOCT3 (A) and rOct3 (B), as well as 'critical' amino acid residues (yellow) are displayed as sticks.

Table 4.6 Norepinephrine docking result summary for human OCT3 and rat Oct3.

Transporter	Amino acid residue	Type of interaction
hOCT3	Phe36	Arene-H interaction
	Met248	Side-chain acceptor
	Asp478	Side-chain acceptor
rOct3	Arg19	Side-chain donor
	Arg20	Side-chain donor
	Phe160	Edge face interaction
	Lys215	Side-chain donor
	Trp218	π-π interaction
	Asp473	Side-chain acceptor

4.4 Discussion

Organic cation transporter 3 is the most widely expressed isoform among the OCTs [1]. Regardless of species, the transporter is responsible for absorption, distribution, and elimination of small organic cations in a variety of tissues including intestine, liver, heart, brain, and so on [1]. Even though the OCT3 orthologs share a great deal of similarity, interactions with compounds do exhibit some inter-species differences. As we tried to use information gathered from conducting homology modeling and docking to understand possible transporter-substrate interactions of hOCT3 (Chapter 3), using a similar method to conduct homology modeling and docking on mouse and rat Oct3 and comparing results from these three species could help us understand possible reasons for inter-species differences.

In this study, we successfully generated homology models for mouse and rat Oct3 using the inorganic phosphate transporter PiPT as template; Ramachandran plots for the two transporters indicate the models are in acceptable conformations (with more than 90% of residues located in favorable regions, Figure 4.4 and Figure 4.7). Binding pockets of mouse and rat Oct3 were defined along with residues that form the pockets (Figure 4.3 and Figure 4.6). Comparing these amino acid residues, we observed that there are great differences between the binding pockets of both transporters, i.e. most amino acids forming the binding pockets in mOct3 and rOct3 are different (Figure 4.3 and Figure 4.6). The discrepancy between mouse and rat Oct3 could also be observed in residues involved with MPP^+-transporter interactions (Table 4.1 and Table 4.2), only one amino acid (Glu446) was detected in both models. The binding pocket of human OCT3 is also different from pockets of rodent orthologs, however, analyzing amino acid

residues identified to form the binding pockets has shown that the transmembrane domains where these residues originated from are the same regardless of species (TMDs 1, 2, 4, 5, 7, 10, and 11), thus revealing structural similarities among species.

Despite similar transport profiles for most substrates/inhibitors, transport affinities of several compounds are vastly divergent for different OCT3 orthologs [26, 27, 70, 73]. This is the first study using 3-D homology models to analyze inter-species differences of OCTs. In order to study this inter-species transport difference, 3-D homology models of transporters were docked with substrates that have distinct affinities for OCT3 orthologs. Since no compound with significantly different affinities for all three OCT3 orthologs has been identified, we first compared hOCT3 and mOCT3 using procainamide (an inhibitor for both transporters) [27, 73]. After docking procainamide to the binding region of hOCT3/mOct3, amino acid residues that could be of importance in interactions between the inhibitor and transporter were proposed and they all belonged to the pre-defined MPP^+ binding pocket (Table 4.5). An aspartate residue was identified to interact with procainamide through ionic salt-bridge interaction in both models, while the ionic interaction in mOct3 is stronger than that in hOCT3. Comparing the specific types of interactions between other 'critical' residues (Phe165 in hOCT3; Thr220, Val223, and Ser466 in mOct3) and procainamide, we observed that critical residues in mOct3 are more closely situated to the ligand and implement stronger interactions, which could be the reason why the affinity for procainamide in mouse Oct3 (IC_{50}=11 μM) is significantly higher (~ 70 times stronger) than that in human OCT3 (IC_{50}=738 μM) [27, 73].

Study of the inter-species transport differences between hOCT3 and rOCT3 was also performed using norepinephrine (substrate for hOCT3 and inhibitor for rOct3). Critical residues interacting with norepinephrine were identified through docking of norepinephrine to the binding region of hOCT3/rOct3 (summarized in Table 4.6). These residues all belonged to the pre-defined MPP^+ binding pocket in both models. The same aspartate residue was identified to interact with norepinephrine as side-chain acceptors in both models. Comparing the specific types of interactions between other 'critical' residues (Phe36 and Met248 in hOCT3; Arg19, Arg20, Phe160, Lys215, and Trp218 in rOct3) and norepinephrine, we observed that there are more critical residues in rOct3 interacting with the ligand and the interactions are stronger compared to those in hOCT3 (aromatic interactions in rOct3 versus hydrogen bonds in hOCT3), which could be the reason why the affinity for norepinephrine in rOct3 (IC_{50}=432 μM) is significantly higher (~ 6 times stronger) than that in hOCT3 (K_m=2630 μM) [26, 70].

In summary, as the first study analyzing inter-species differences among OCT3 orthologs, we successfully generated 3-D homology models for mouse and rat organic cation transporter 3, identified their binding pockets for MPP^+, amino acid residues forming the binding pockets, as well as residues that are critical for interactions between transporter and MPP^+. Through more docking studies with procainamide and norepinephrine, residues critical for ligand-transporter interactions were identified. We concluded that the binding pockets of OCTs could be different despite the high sequence similarity between transporters (mouse and rat Oct3). Docking of the two compounds suggested that ligands bind to different regions inside the large binding pocket of OCT3. Differences in the strength and number of strong binding interactions

between ligand and transporter are contributing to the inter-species differences in binding affinities.

Chapter 5

KINETIC INVESTIGATION OF THE INTERACTION BETWEEN A NOVEL SERIES OF COMPOUNDS EXHIBITING ANTI-DEPRESSANT LIKE EFFECTS AND ORGANIC CATION TRANSPORTERS

5.1 Introduction

Depressive disorder, also known as depression, is one of the most burdensome psychiatric disorders in the world. It is often accompanied by low self-esteem, loss of interest in normally enjoyable activities, low energy, and pain without a clear cause [99]. Depressive disorder can negatively affect a person's personal, work, or school life, as well as sleeping, eating habits, and general health [106]. Approximately 6-7% of full-time U.S. workers experienced depressive disorder within the year 2015, the total economic burden of the disease is estimated to be $210.5 billion per year, and for every dollar spent on depression direct costs in 2010, an additional $1.9 was spent on depression-related indirect costs [107]. Between 2-7% of adults with depression die by suicide, and up to 60% of people who die by suicide had depressive disorder or other mood disorders [108]. Although plenty of antidepressant drugs have been used to treat the disease, side effects and delayed onset of action are often observed in clinical applications [76]. And these treatments fail to produce beneficial effects in nearly half of the patients [75].

The cause of depressive disorder is believed to be a combination of genetic, environmental, and psychological factors [99]. Previous studies have demonstrated that depression is often associated with a reduction of monoamine neurotransmitters such as 5-HT and NE in the synaptic clefts [35, 109]. Therefore, understanding the mechanism of 5-HT clearance in the brain is vital for developing antidepressant drugs. There are two distinguishable mechanisms of aminergic neurotransmitter clearance from the synaptic cleft: uptake-1 system (high-affinity, low capacity reuptake through SERT, NET, and DAT) and uptake-2 system (low-affinity, high capacity reuptake) [100]. Currently, most antidepressants are thought to work by blocking the uptake-1 system [75]. Alternatively, the uptake-2 system has gradually gained attention as a new therapeutic target for antidepressants. Increasing evidence has indicated that organic cation transporter 2 (OCT2) and 3 (OCT3), which are widely expressed in the CNS, interact with different kinds of neurotransmitters (DA, 5-HT, and NE) and likely represent important components of the uptake-2 system [35]. For example, administering the OCT inhibitor, normetanephrine, in mice increased extracellular NE levels in brain and produced enhanced antidepressant-like effects [110]. Furthermore, the expression and function of Oct3 in the CNS was significantly increased in SERT knockout mice [30, 78]. Therefore, OCTs may represent unrecognized targets of antidepressants and may impact their pharmacological actions.

Recently, a series of compounds has been synthesized as potential novel therapeutic agents for treating depression in the laboratory of Dr. Malgorata Dukat (Department of Medicinal Chemistry, VCU). Analysis of lead compounds (closely related to test compounds in this study) have shown promising antidepressant-like effects in

mice (Dr. Dukat laboratory, unpublished data). Studies of these compounds suggested that they might not be potent inhibitors of the uptake-1 system, considering their binding affinities for SERT and NET were greater than 10 μM (Dr. Dukat laboratory, unpublished data). Looking at the logP values, molecular weights, and chemical structures (not shown here) of these test compounds, it was determined that they might be OCT substrates and/or inhibitors, potentially exhibiting antidepressant-like effects via uptake-2 inhibition. To test this hypothesis, we examined the interactions of test compounds with hOCT1-3 and mOct1-3 to determine if OCTs could play a role in their antidepressant-like action.

5.2 Materials and Methods

5.2.1 Chemicals

Tritiated 1-methyl-4-phenylpyridinium ([^{3}H]MPP$^+$) was purchased from PerkinElmer Life and Analytical Science (Waltham, MA), and unlabeled MPP$^+$ was obtained from Sigma-Aldrich (St. Louis, MO). Quinine monohydrochloride dihydrate was purchased from Acros Organics (Fair Lawn, NJ). The test compounds were synthesized and provided by Dr. Dukat's laboratory. Details of structures and synthetic routes are not provided at this time (proprietary information).

5.2.2 Tissue Culture

Stably transfected human embryonic kidney 293 (HEK) cells expressing hOCT1 (HEK-hOCT1), hOCT2 (HEK-hOCT2), hOCT3 (HEK-hOCT3), mOct1 (HEK-mOct1), mOct2 (HEK-mOct2), or mOct3 (HEK-mOct3), and their empty vector transfected background control cell lines were maintained at 37°C with 5% CO_2 in DMEM high

glucose medium (Mediatech Inc., Herndon, VA) containing 10% FBS, 1% penicillin/streptomycin, as well as 600 µg/ml G418.

5.2.3 Cellular Uptake Assay

The procedure for cell accumulation assay has been described previously with minor modification [94].Two days before cellular uptake experiment, $2*10^5$ cells/well were seeded in 24-well tissue culture plates (coated with poly-D-lysine) and grown in the absence of antibiotics. On the day of experiment, cells were equilibrated in transport buffer at room temperature (22-25°C) for 10 min. After equilibrium, this solution was replaced with 500 µL of fresh transport buffer containing unlabeled MPP^+ (1 µM) spiked with [^{3}H]MPP^+ (0.25 µCi/mL) in the presence of increasing concentrations (0.1 to 200 µM) of unlabeled test compounds for the times indicated. At the end of the incubation, the cells were quickly rinsed three times with ice-cold transport buffer and lysed with 200 µL NaOH (1 N). After shaking for two hours, mixture was neutralized with 250 µL HCl (1 N) and 200 µL HEPES (0.01 M). The radioactivity of cell lysate (400 µL from each well) was quantified by liquid scintillation counting, and the uptake profile was normalized by the total protein content (quantified using the Bradford method). The cellular uptake of substrates was shown as picomoles of substrate per milligram total protein. Substrate concentration and accumulation time used for kinetic analysis of hOCT1, hOCT2, hOCT3, mOct1, mOct2 and mOct3 (1 µM for MPP^+ 1 min) were determined previously [3, 25]. All uptake data were corrected for background accumulation in corresponding empty vector transfected control cells. Kinetic calculations were performed using GraphPad Prism Software version 5.0 (GraphPad

Software Inc., San Diego, CA). The half maximal inhibitory concentration (IC_{50}) was calculated using nonlinear regression and the "log(inhibitor) vs. response" model. Results were confirmed by repeating all experiments at least three times with triplicate wells for each data point in every experiment.

5.2.4 Statistics

Data are reported as mean ± SD. Statistical differences were analyzed using one-way ANOVA followed by Dunnett's post-hoc t-test (α=0.05).

5.3 Results

5.3.1 Initial screening of test compounds as OCT inhibitors

The inhibitory effects of test compounds were initially screened on three human OCTs and three mouse Octs using MPP^+ as prototypical substrate. Stably transfected hOCT1-expressing (HEK-hOCT1) cells showed marked accumulation of MPP^+ (~62 fold) compared to empty vector transfected background control cells (124.2 ± 1.3 vs. 2.0 ± 0.2 pmol/mg protein/10 min, respectively; data not shown). HEK-mOct1 cells exhibited ~44 fold accumulation of MPP^+ as compared to empty vector transfected background control cells (88.8 pmol/mg protein/10 min). The known OCT inhibitor, quinine (200 μM), showed virtually complete inhibition of hOCT1- and mOct1-mediated MPP^+ uptake (> 90% inhibition; Figure 5.1 (A) and (B)). The cell accumulation assay demonstrated that all test compounds (100 μM) significantly inhibited hOCT1 activity (Figure 5.1 (A)). In HEK-mOct1 cell experiments, all test compounds (100 μM) except KAI419 significantly inhibited MPP^+ transport by mOct1 (Figure 5.1 (B)).

The inhibitory effects of test compounds on hOCT2- and mOct2-mediated transport were examined next. Stably transfected hOCT2-expressing (HEK-hOCT2) cells showed significantly higher amount of accumulation of MPP^+ (~58 fold) compared to empty vector transfected background control cells (115.4 ± 0.1 pmol/mg protein/10 min). HEK-mOct2 cells exhibited ~48 fold accumulation of MPP^+ as compared to empty vector transfected background control cells (95.8 pmol/mg protein/10 min). The known OCT inhibitor, quinine (200 μM), showed almost complete inhibition of hOCT2- and mOct2-mediated MPP^+ uptake (> 98% inhibition; Figure 5.1 (C) and (D)). The cell accumulation assay demonstrated that all test compounds significantly inhibited hOCT2 and mOct2 activity at the concentration of 100 μM (Figure 5.1 (C) and (D)).

Stably transfected hOCT3-expressing (HEK-hOCT3) cells showed significant accumulation of MPP^+ ~56 fold greater than empty vector transfected background control cells (111.2 pmol/mg protein/10 min), and mOCT3 transfected HEK cells showed ~10 fold greater accumulation of MPP^+ compared to control cells with value of 99.2 pmol/mg protein/10 min. MPP^+ transport was almost completely (> 90% inhibition; Figure 5.1 (E) and (F)) blocked by quinine (200 μM), a prototypical inhibitor for OCTs. All test compounds at a concentration of 100 μM significantly inhibited MPP^+ uptake by hOCT3 and mOct3 (Figure 5.1 (E) and (F)).

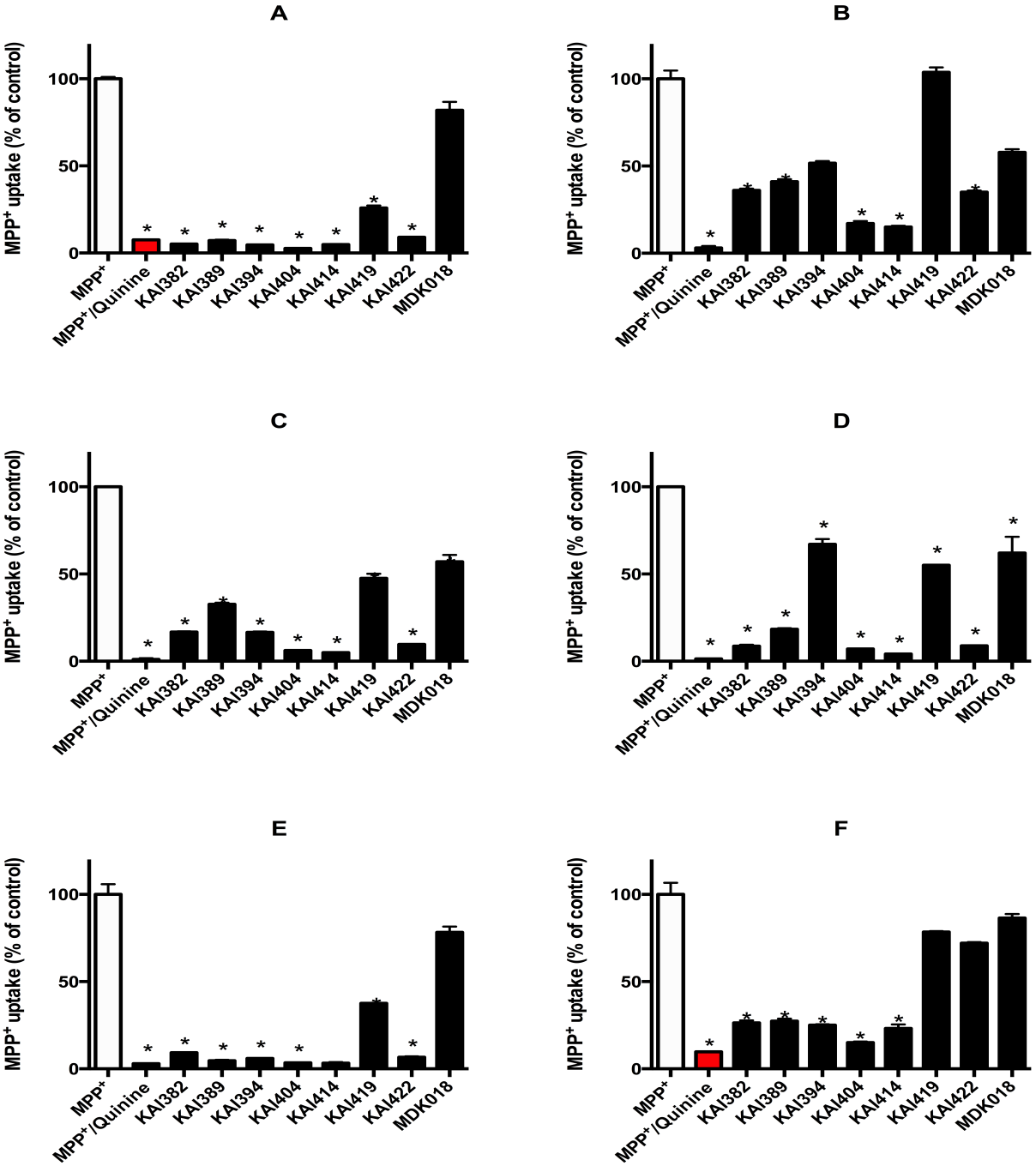

Figure 5.1 Inhibition profiles of test compounds on OCTs.

Inhibition of (A) hOCT1-, (B) mOct1-, (C) hOCT2-, (D) mOct2-, (E) hOCT3-, and (F) mOct3-mediated MPP^+ uptake by test compounds (blue, 100 uM) and quinine (black, 200 uM). The concentration of MPP^+ was 1 uM, incubation time was 10 min, and data shown were corrected for non-specific background. Values are mean ± SD of triplicate values. * denotes $p < 0.05$ as determined by one-way ANOVA followed by Dunnett's t-test.

5.3.2 Determination of IC_{50} values for test compounds

Based on the initial screening results, IC_{50} values of KAI394 for mOct2, of KAI419 for mOct1, mOct2, and mOct3, and of MDK018 for all OCT isoforms were not determined because they did not produce more than 50% inhibition of MPP^+ transport, indicating their IC_{50} values would be larger than 100 μM (Figure 5.1). From the screening result, it was seen that MDK018 is not a potent inhibitor for organic cation transporters.

Dose-response studies were conducted to estimate the IC_{50} values of test compounds exhibiting ≥ 50% inhibition on hOCT1, hOCT2, hOCT3 and their murine orthologs. IC_{50} values of test compounds for hOCT1 were in the low micro-molar range (2.6 μM to 6.3 μM) except for KAI419 (Figure 5.2, Table 5.1). The IC_{50} value of KAI419 for hOCT1 was estimated as 23.3 ± 0.9 μM, which is 4-9 fold higher than the other compounds (Figure 5.2, Table 5.1). Compared with hOCT1 results, IC_{50} values of test compounds for mOct1 were considerably higher (18.6 μM to 37.2 μM), and KAI419 did not inhibit more than 50% of MPP^+ transport in the screening study (Figure 5.3, Table 5.1). Thus, the test compounds exhibited stronger inhibition of hOCT1 than mOct1, indicating a species difference. The IC_{50} values for the two transporters have a similar trend with KAI419 being the least effective test compound.

IC_{50} values of test compounds for hOCT2 were also higher compared to those for hOCT1 (5.1 μM to 48.0 μM). Test compounds exhibit their inhibitory effects towards hOCT1 and 2 in a similar trend, with KAI414 being the most potent inhibitor (5.1 ± 1.3 μM) and KAI419 being the worst inhibitor (48.0 ± 18.7 μM) (Figure 5.4, Table 5.1). The IC_{50} values of test compounds for mOct2 ranged from 4.0 μM to 22.4 μM, and the

values of KAI394 and KAI419 were higher than 100 μM (IC_{50} not determined) (Figure 5.5, Table 5.1). Thus, unlike for the OCT1 orthologs, the inhibition profiles for OCT2 in two species are very similar. KAI414 was also the most potent inhibitor of mOct2 (4.0 ± 0.9 μM).

Dose-response studies for hOCT3 and mOct3 indicated that the IC_{50} values of test compounds for hOCT3 were also in the low micro-molar range (1.4 μM to 8.4 μM) except for KAI419 (Figure 5.6, Table 5.1). The IC_{50} value of KAI419 for hOCT3 was determined as 26.9 ± 8.5 μM, which is 3 – 19 fold higher than the other compounds (Figure 5.6, Table 5.1). This situation is extremely similar to the case in hOCT1. Compared with hOCT3 results, IC_{50} values of test compounds for mOct3 were also considerably higher (17.4 μM to 40.9 μM), and KAI419 could not inhibit more than 50% of MPP^+ transport in the screening study (Figure 5.7, Table 5.1). Therefore, the test compounds more efficiently inhibited hOCT3 than mOct3, indicating a species difference, similar to he trend in hOCT1/mOct1 inhibition. One outstanding point was that KAI422 did not inhibit more than 50% MPP^+ uptake on mOct3, in contrast to being rather potent for the other five OCTs.

All test compounds showed potent affinities for human OCT1 and OCT3, and among the other transporters, mOct2 seemed to have the highest affinity towards the compounds (Table 5.1). Besides MDK018, which showed minimum inhibition effect for all transporters, KAI419 was the least potent inhibitor across all OCT subtypes.

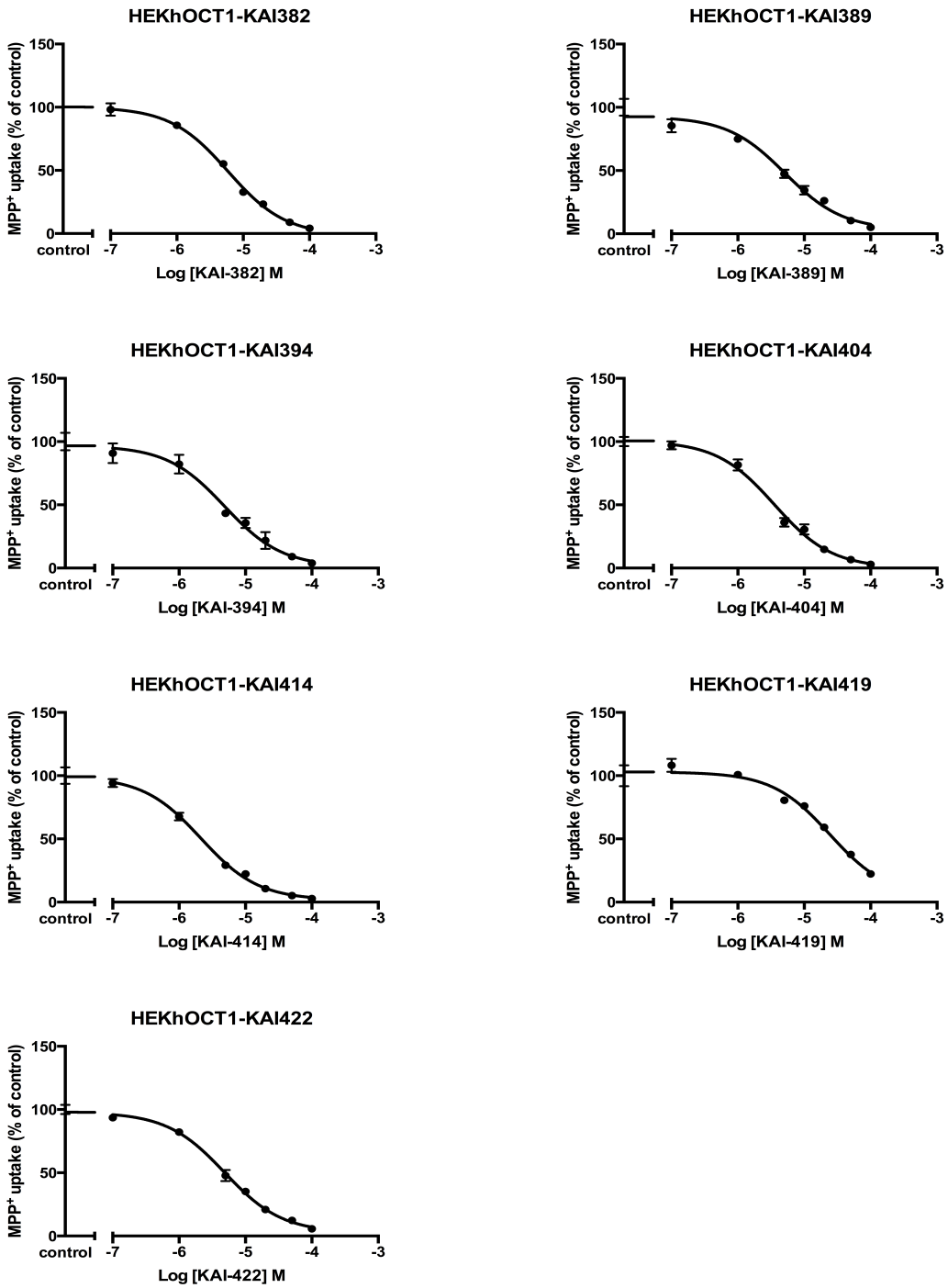

Figure 5.2 Dose-response curves for test compounds on hOCT1.

Representative data showing 1 min uptake of MPP^+ (1 μM) measured in HEK-hOCT1 cells in the presence of increasing concentrations of test compounds (10^{-7} to 10^{-4} M) are shown. Data were corrected for nonspecific background measured in the empty vector control cells and are means ± SD of triplicate values. IC_{50} values were determined with nonlinear regression and the "log(inhibitor) versus response" model using GraphPad Prism software.

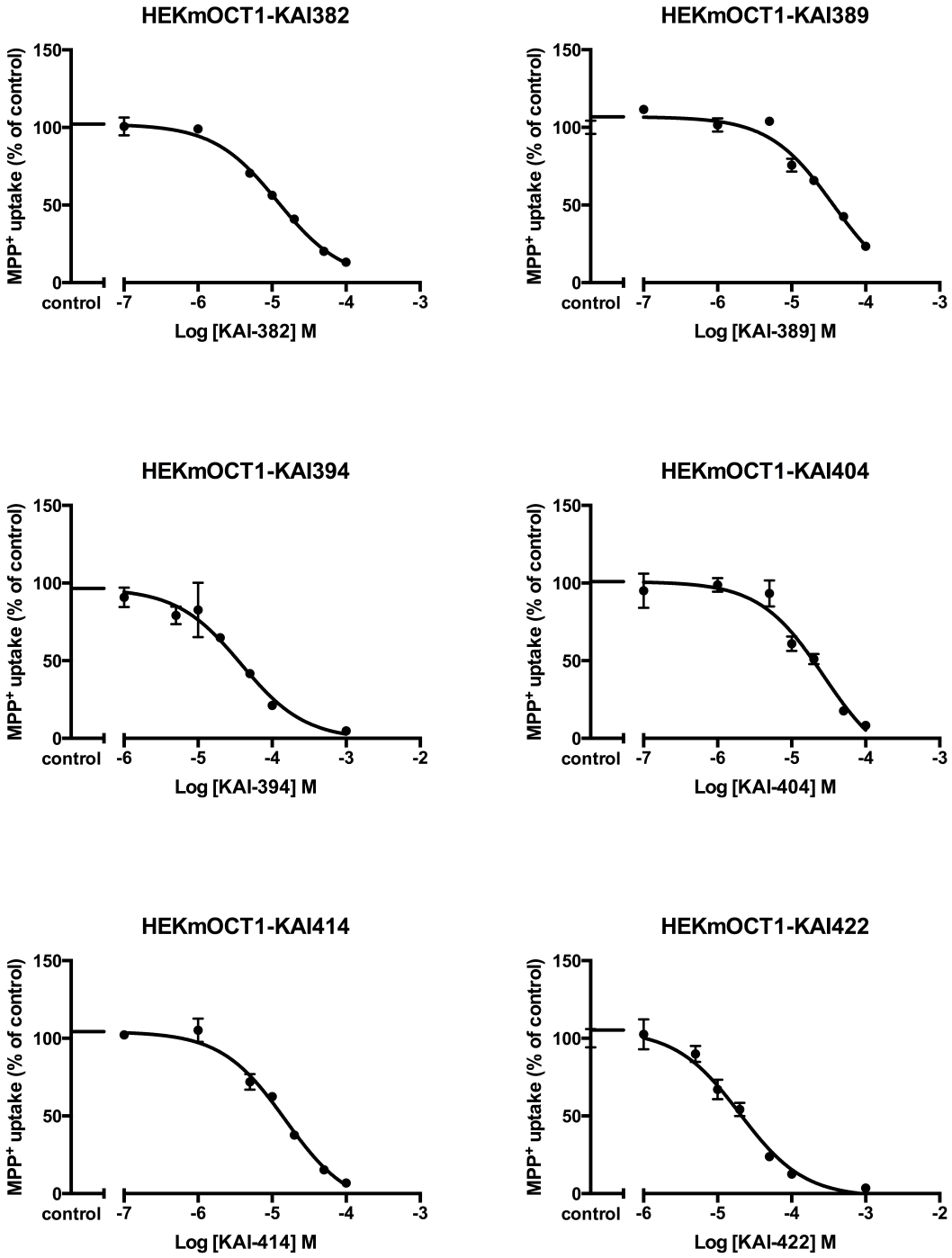

Figure 5.3 Dose-response curves for test compounds on mOct1.

Representative data showing 1 min uptake of MPP^+ (1 μM) measured in HEK-mOct1 cells in the presence of increasing concentrations of test compounds (10^{-7} to 10^{-3} M) are shown. Data were corrected for nonspecific background measured in the empty vector control cells and are means ± SD of triplicate values. IC_{50} values were determined with nonlinear regression and the "log(inhibitor) versus response" model using GraphPad Prism software.

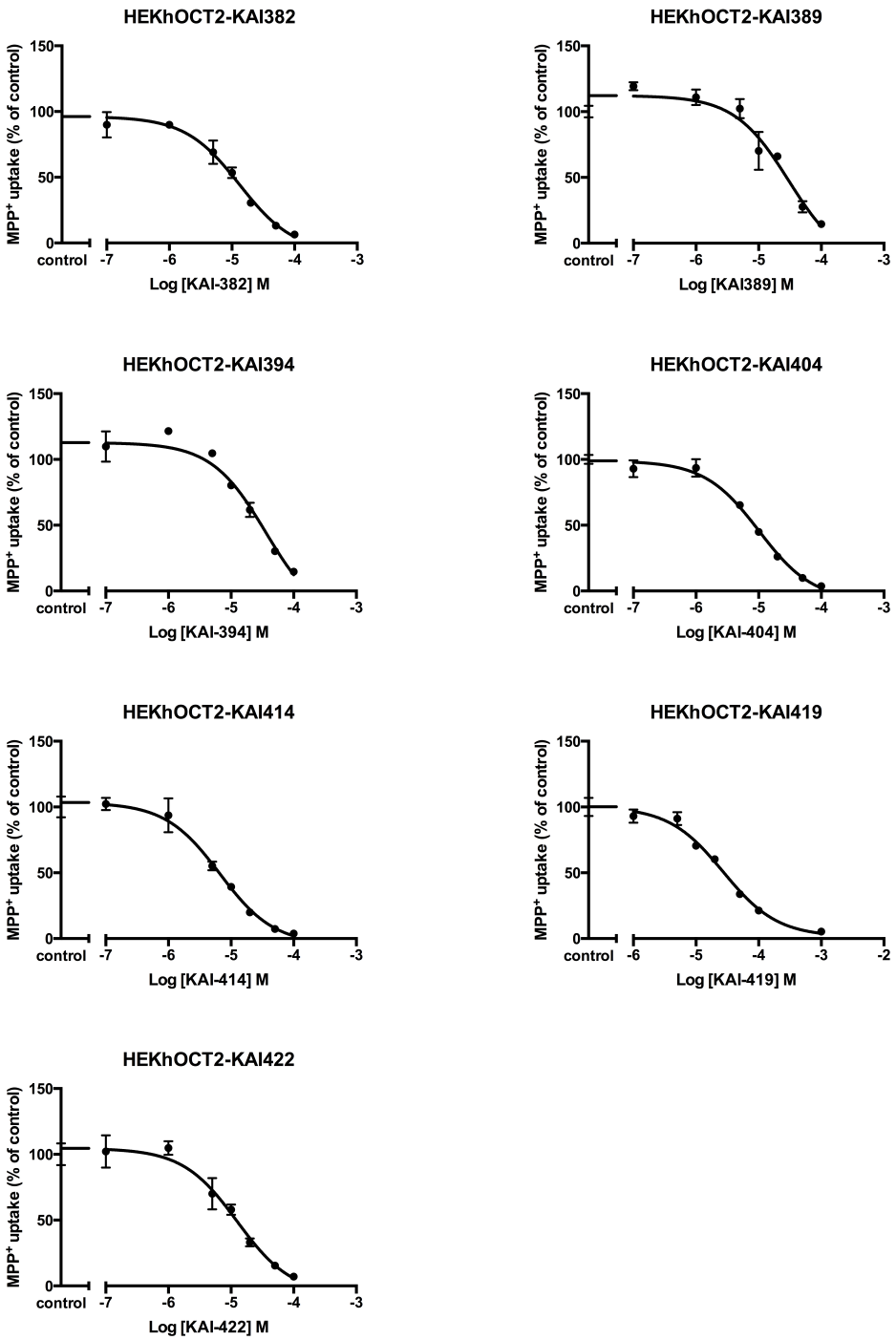

Figure 5.4 Dose-response curves for test compounds on hOCT2.

Representative data showing 1 min uptake of MPP^+ (1 μM) measured in HEK-hOCT2 cells in the presence of increasing concentrations of test compounds (10^{-7} to 10^{-3} M) are shown. Data were corrected for nonspecific background measured in the empty vector control cells and are means ± SD of triplicate values. IC_{50} values were determined with nonlinear regression and the "log(inhibitor) versus response" model using GraphPad Prism software.

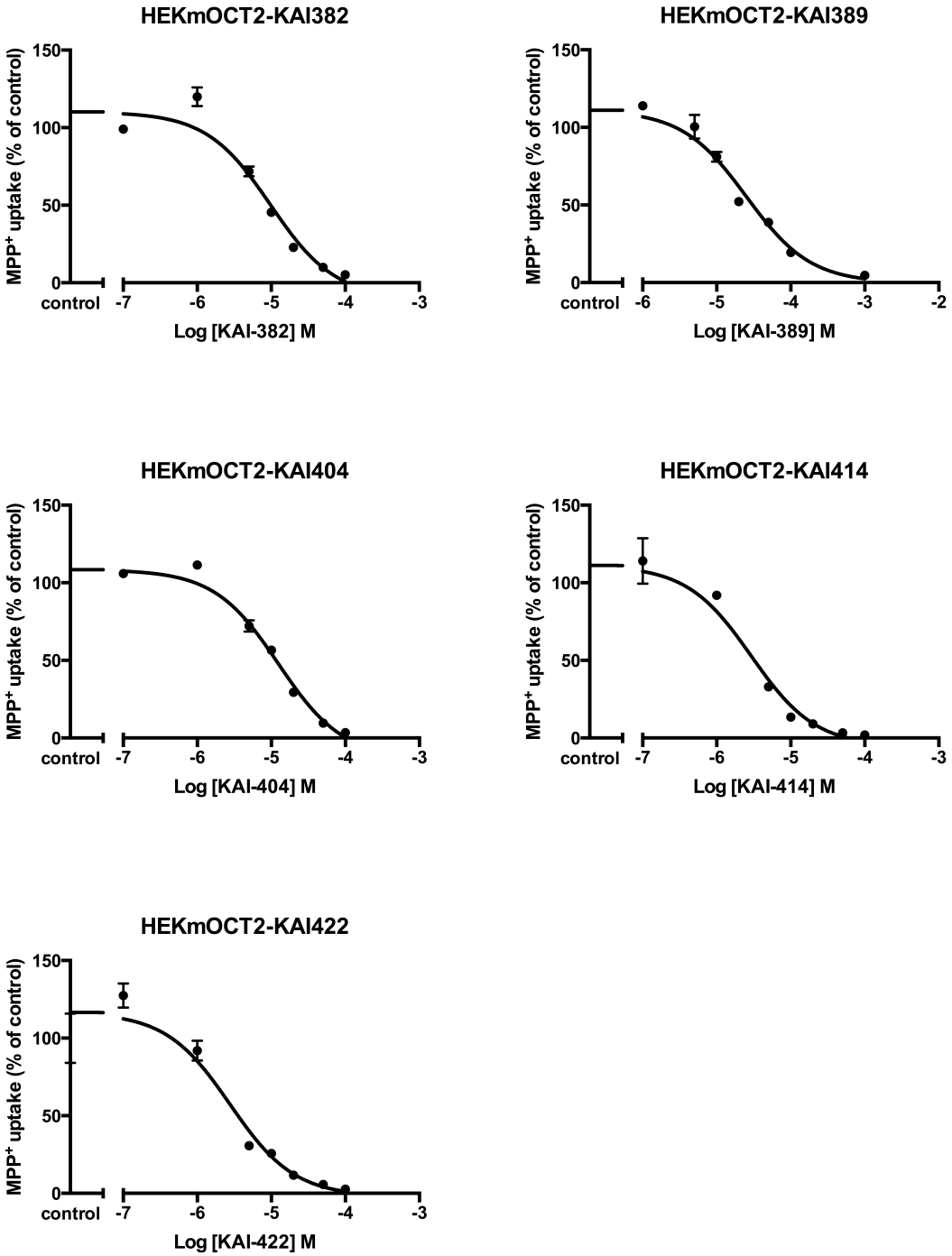

Figure 5.5 Dose-response curves for test compounds on mOct2.

Representative data showing 1 min uptake of MPP^+ (1 μM) measured in HEK-mOct2 cells in the presence of increasing concentrations of test compounds (10^{-7} to 10^{-3} M) are shown. Data were corrected for nonspecific background measured in the empty vector control cells and are means ± SD of triplicate values. IC_{50} values were determined with nonlinear regression and the "log(inhibitor) versus response" model using GraphPad Prism software.

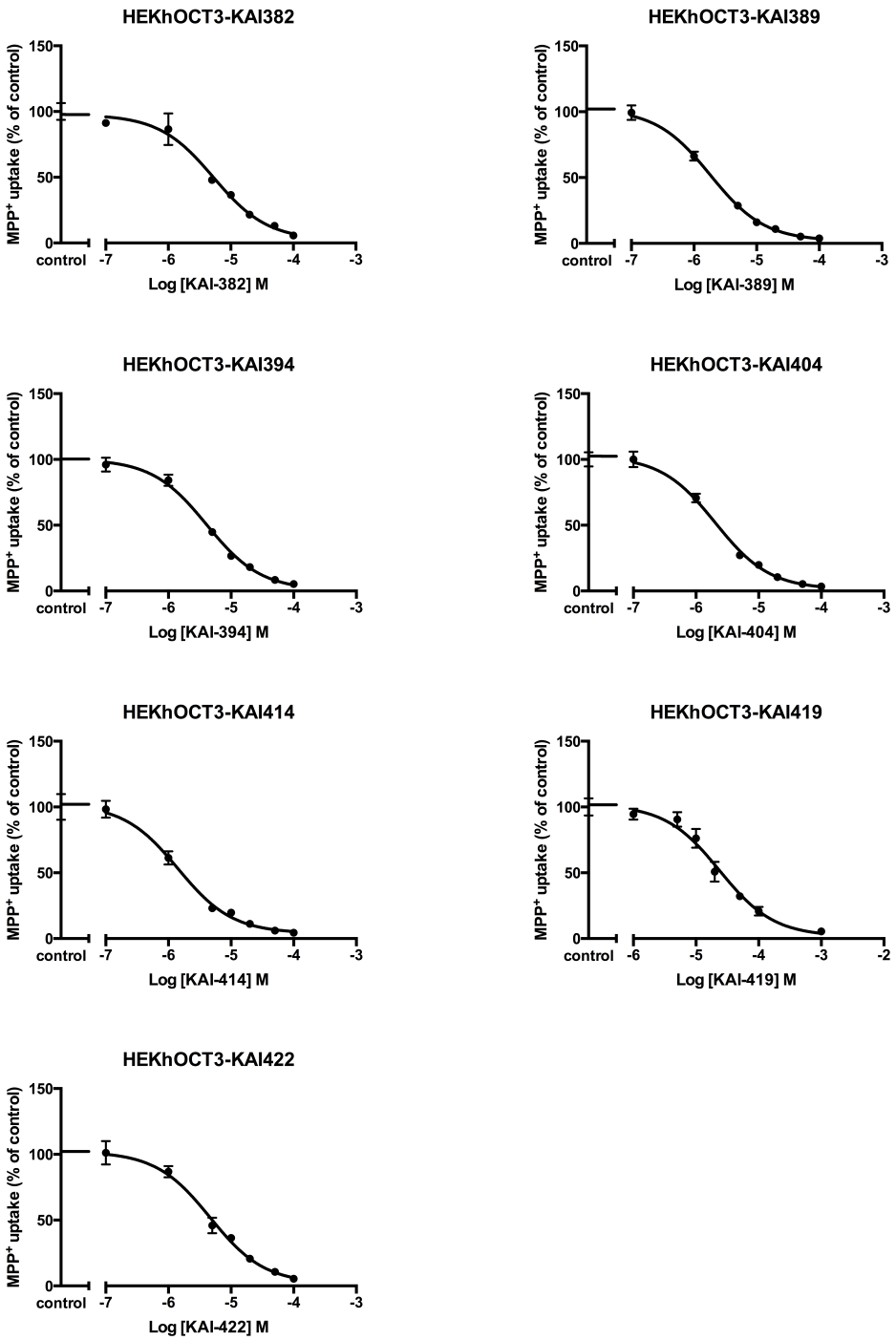

Figure 5.6 Dose-response curves for test compounds on hOCT3.

Representative data showing 1 min uptake of MPP^+ (1 μM) measured in HEK-hOCT3 cells in the presence of increasing concentrations of test compounds (10^{-7} to 10^{-3} M) are shown. Data were corrected for nonspecific background measured in the empty vector control cells and are means ± SD of triplicate values. IC_{50} values were determined with nonlinear regression and the "log(inhibitor) versus response" model using GraphPad Prism software.

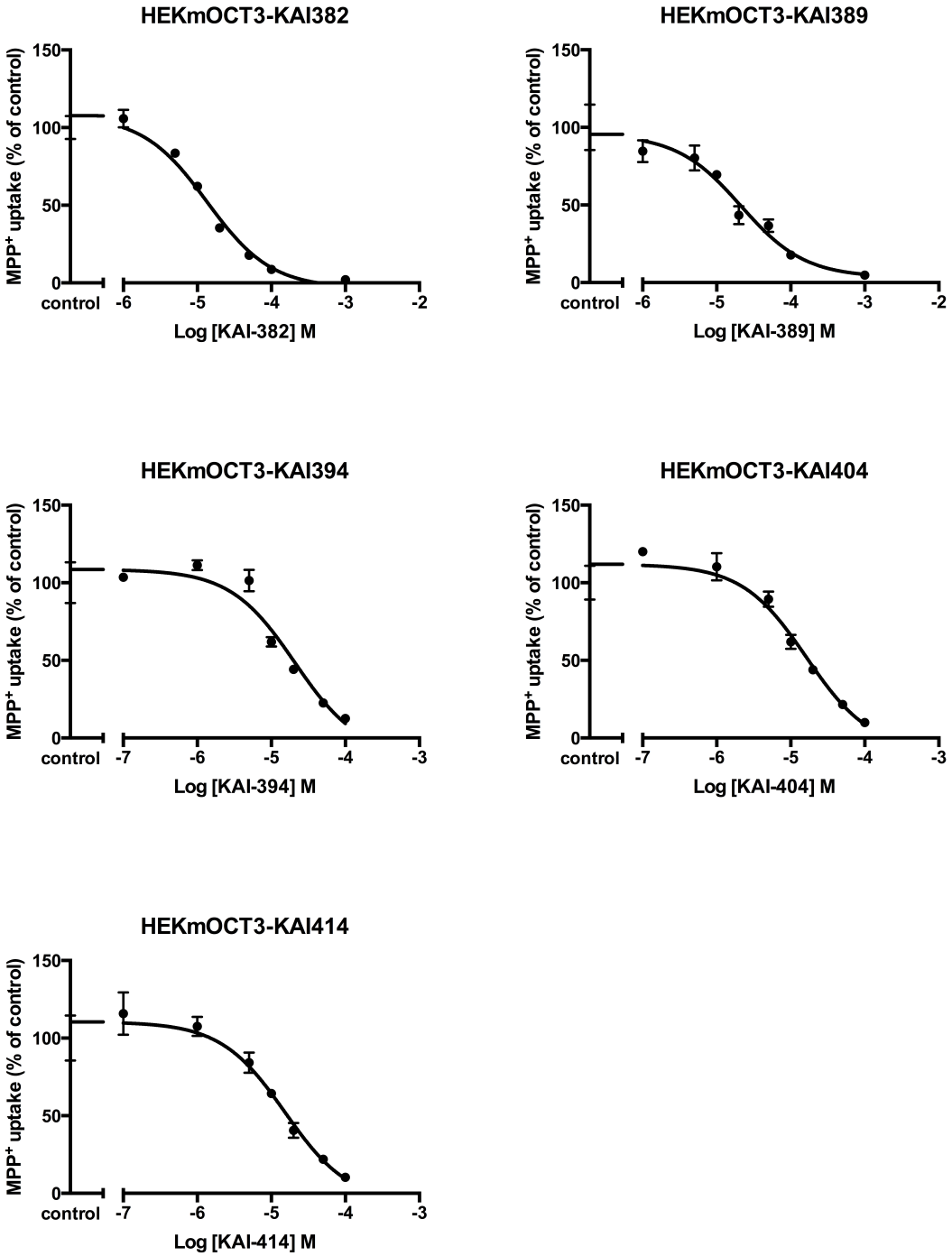

Figure 5.7 Dose-response curves for test compounds on mOct3.

Representative data showing 1 min uptake of MPP^+ (1 μM) measured in HEK-mOct3 cells in the presence of increasing concentrations of test compounds (10^{-7} to 10^{-3} M) are shown. Data were corrected for nonspecific background measured in the empty vector control cells and are means ± SD of triplicate values. IC_{50} values were determined with nonlinear regression and the "log(inhibitor) versus response" model using GraphPad Prism software.

Table 5.1 IC_{50} values of test compounds for human and mouse OCTs

Compound	IC_{50}[a] (μM)					
	hOCT1	hOCT2	hOCT3	mOct1	mOct2	mOct3
KAI382	6.3 ± 1.3	12.8 ± 0.7	8.4 ± 4.4	18.6 ± 7.6	8.9 ± 2.5	23.3 ± 9.6
KAI389	5.6 ± 0.4	36.5 ± 9.1	2.0 ± 0.2	37.2 ± 14.2	22.4 ± 5.9	19.6 ± 3.4
KAI394	4.3 ± 1.6	35.7 ± 0.2	3.8 ± 0.4	38.0 ± 4.9	ND[b]	40.9 ± 18.2
KAI404	2.7 ± 1.0	10.1 ± 0.3	2.2 ± 0.3	33.5 ± 6.3	13.8 ± 3.4	17.4 ± 3.3
KAI414	2.6 ± 0.5	5.1 ± 1.3	1.4 ± 0.1	19.2 ± 3.8	4.0 ± 0.9	18.6 ± 4.4
KAI419	23.3 ± 0.9	48.0 ± 18.7	26.9 ± 8.5	ND	ND	ND
KAI422	5.7 ± 0.8	11.7 ± 3.2	5.0 ± 0.6	22.6 ± 2.3	8.6 ± 5.2	ND
MDK018	ND	ND	ND	ND	ND	ND

[a]IC_{50} values were expressed as mean ± SD from triplicate determinations.
[b]ND, not determined.

5.4 Discussion

Depressive disorder is the fourth leading cause of illness-induced disability according to the global burden of disease study in 2010, and it is predicted to reach the second place by 2020 [111]. Although a wide variety of drugs have been developed and used in treating depression clinically, approximately half of the treated patients failed to find relief using current therapies, especially in mild or moderate cases of depression [109, 112]. This may be due to the presence of multiple clearance pathways for monoamine neurotransmitters in the brain subject to different modes of regulation. Undesirable side effects, including nausea, weight change, anxiety, sexual dysfunction, increased bone fracture risk and gastrointestinal effects, are often observed in the clinical application of antidepressants [36, 75]. Both side effects and the lack of response to traditional therapeutics indicate an unmet need to develop antidepressants with novel mechanisms of action, which will ideally bring greater efficacy as well as fewer side effects compared to existing antidepressants. Recently, human OCT2 and OCT3 have been discovered as key components of uptake-2 system and suggested to play an important role in regulating neurotransmitter clearance in human brain [26, 34]. A number of currently used antidepressants, such as fluoxetine, desipramine, and sertraline, are proven to be effective OCT inhibitors *in vitro* [98, 104]. Currently, it remains unclear what role OCTs have in the therapeutic action of these compounds; however, together the evidence suggests OCTs may be viable targets in treating mood disorders.

The test compounds examined in this study are a series of novel compounds developed as potential therapeutic agents for treating depression [105, 113]. Previous

kinetic studies on other compounds in the same class with similar structures (also generated from Dr. Dukat's laboratory) yielded high binding affinities for SERT and NET (greater than 10 μM); however, a chloride substituted compound demonstrated potent antidepressant-like effects in mice, indicating the possibility of another working mechanism (maybe through targeting uptake-2 system) [105]. In the present study, the interactions of eight novel compounds with OCTs were studied. The inhibitory effects of the compounds varied among different orthologs and paralogs of OCT3, and also depended on their structures (structures not shown at this point). Overall, mOct1 was least sensitive towards compound inhibition, and hOCT2 is the least sensitive in human OCT paralogs (Table 5.1). Several test compound(s) (e.g., KAI422) showed significantly different inhibitory affinities across human and mouse transporters, and could potentially be used as a method to differentiate corresponding transporters. In general, murine orthologs were less sensitive to inhibition by test compounds as compared to human orthologs (Table 5.1). The IC_{50} values of test compounds for mOct2 were comparable (0.6 to 1.4 fold) to those of hOCT2, whereas relatively weaker inhibitory effects were observed for mOct1 and mOct3 compared to those of their human orthologs. Of the eight test compounds, MDK018 did not demonstrate significant inhibitory effects for any tested transporter, and KAI414 was the most potent compound for the transporters (except for slightly higher IC_{50} value in mOct1).

In summary, eight compounds were examined and potent inhibitors for hOCTs/mOcts were identified. The inhibitory effects of compounds with hOCTs/mOcts were tested and compared. Results suggest that novel lead compounds, such as KAI414, could be further tested in mice to look for antidepressant-like effects, and

docking of these compounds to homology models of OCTs should provide useful knowledge regarding highly interactive functional groups. This structure-activity relationship information combined with *in vivo* (previous study by Dr. Dukat's laboratory) and *in vitro* data could support and help with designing the next generation of antidepressants.

Chapter 6

OVERALL CONCLUSIONS AND FUTURE DIRECTIONS

Organic cation transporters are typically located on the membrane of polarized barrier epithelia and are responsible for the absorption, distribution, and elimination of small organic cations including metabolites and drugs [1]. The wide expression of OCT3 in various peripheral organs such as heart, skeletal muscle, brain, small intestine, liver, lung, kidney, and its broad substrate selectivity make the transporter a target for therapeutics as well as a good candidate for rational drug design, but also could result in undesirable side effects (including drug-drug interactions) [1]. Decades have passed since the OCTs have been cloned, but little is known about their transport mechanism, except that they are driven by electrochemical gradient [114]. Thus elucidating the molecular mechanism of OCT3-substrate interactions is important for understanding substrate/inhibitor recognition, drug-drug interaction, and for rational drug design. In this study, we began to study the structure as well as substrate/inhibitor interactions of hOCT3 and its rodent orthologs through homology modeling, and also the potential role of OCT inhibitors in major depressive disorders.

Since no crystal structure of the SLC22 family has been generated, conducting 3-D homology modeling is the only method to get a close estimation of the structure of the transporters. Even though a number of studies have been conducted to learn about

OCT transport mechanism (specifically transporter-substrate interactions), the lack of a high quality template with acceptable sequence identity has made these models obsolete, and could not be used to guide mutational studies (only models with more than 25% similarity compared to the template could be properly used) [49]. In chapter 3 and chapter 4, we created homology models for human, mouse, and rat OCT3 to study their substrate-binding interactions as well as inter-species differences in OCT3-compound interactions. PiPT, the crystal structure of which has recently been established, is an inorganic phosphate transporter that shares high structure and sequence similarities to the transporters of the SLC22 family, and was chosen as the template for model construction [92]. In chapter 3, we used *in silico* modeling to study binding interactions between hOCT3 and different substrates. A 3-D homology model of hOCT3 was generated based on multiple model validation methods, and a pocket region for substrate/inhibitor binding interactions was identified. In the docking study with MPP^+, a prototypical substrate for OCT, five key amino acid residues were identified that interact with the ligand, namely Phe36, Val40, Trp358, Asp451, and Glu478. The validity for this hypothesized binding profile was verified through *in vitro* MPP^+ transport assays on cell lines transfected with hOCT3 mutated at these sites. MPP^+ transport activity of hOCT3 was altered after residue substitutions, with complete loss of MPP^+ transport in Val40, Trp358 and Glu478 mutants, as well as significant decrease of transporter-MPP^+ affinity in the other mutants (except Phe36Tyr and Glu451Asp). Three-dimensional homology model for a hOCT3 mutant with decreased MPP^+ transport activity (Val40Leu) was generated and the binding pocket was not drastically changed; substituted residue was located farther away from the ligand while

other critical residues were still interacting with MPP^+, however the interactions were weaker. Models for hOCT3 mutants with no MPP^+ transport activity were also generated; docking with MPP^+ showed only weak interactions between the ligand and binding pocket residues in each model, and the binding pockets were changed to a large extent. Docking studies with structurally divergent hOCT3 substrates, serotonin, metformin, TPA^+, and epinephrine, demonstrated binding interactions between ligands and critical residues. Comparing key residues for different substrates, we observed that some of the amino acid residues only worked in the interaction with one type of substrate, while other residues were identified more than once, thus interacting with different substrates. These residues include Phe36, Val40, Asn162, Met248, Trp358, and Asp478. These results suggest that different substrates bind to the same binding pocket of hOCT3, but the specific location/region where a ligand binds could be different and may overlap. Comparison between our binding pocket of hOCT3 and identified residues in literature has suggested that binding pockets of OCTs are different in different paralogs, but they do share certain level of similarity.

Human OCT3 and its rodent orthologs share a great extent of sequence, structural, and functional similarities [1]. However, the transport profile for a few substrates and inhibitors are largely divergent among species [1]. For instance, procainamide, a drug for treating cardiac arrhythmias, is a low affinity inhibitor for hOCT3 (IC_{50} = 738 μM), but a high affinity inhibitor for mOct3 (IC_{50} = 11 μM); norepinephrine, a monoamine neurotransmitter, is a low affinity inhibitor for hOCT3 (IC_{50} = 2630 μM), but a substrate for mOct3 with higher affinity (K_m = 432 μM) [26, 27, 70, 73]. In chapter 4, we assessed possible reasons for inter-species differences among

human, mouse, and rat OCT3 through *in silico* modeling and docking studies. Three-dimensional homology models for mouse and rat Oct3 were created using the same protocol as for hOCT3, and binding regions were determined. Binding pockets of human, mouse, and rat OCT3 were all formed by amino acid residues from the same transmembrane domains (TMDs 1, 2, 4, 5, 7, 10, and 11), regardless of species. Binding pockets for human, mouse, and rat OCT3 are different from each other, even though mouse and rat Oct3 share high sequence identity. In the docking study with procainamide, a strong ionic salt-bridge interaction between one key residue (Asp) in OCT3 and the inhibitor was observed for both models (distance between ligand and residue was closer in mOct3). The types of interactions as well as distances to the ligand from other 'critical' residues (Phe165 in hOCT3; Thr220, Val223, and Ser466 in mOct3) have demonstrated that the amino acid residues in mOct3 are more closely situated to the ligand and implement stronger interactions, which could lead to the higher affinity for procainamide in mOct3. In the docking study with norepinephrine, the same aspartate residue was identified to interact with norepinephrine as side-chain acceptors in both hOCT3 and rOct3 models. The types of interactions of other 'critical' residues (Phe36 and Met248 in hOCT3; Arg19, Arg20, Phe160, Lys215, and Trp218 in rOct3) interacting with norepinephrine have demonstrated that there are more critical residues in rOct3 interacting with the ligand and the interactions are stronger compared to those in hOCT3 (aromatic interactions in rOct3 versus hydrogen bonds in hOCT3), which could be the reason for the higher affinity for norepinephrine on rOct3. Therefore, differences in transporter substrate/inhibitor affinity profiles among OCT3 orthologs may be explained by differing strength of interactions between ligands and transporters.

The novel test compounds examined in this work represent a series of compounds developed as potential therapeutics that possess antidepressant-like effects. However, previous studies of compounds of the same family failed to significantly inhibit uptake-1 activity (Dr. Dukat laboratory, unpublished data). Based on their physiochemical properties, we hypothesized that these compounds may be OCT inhibitors and act on uptake-2 system, which may explain the possible antidepressant-like effects. In Chapter 5, we assessed the inhibitory effects of eight test compounds on three OCTs in both human and mouse. At 100 μM, all test compounds except for MDK018 showed significant inhibition on three human OCTs. The IC_{50} values for six of these test compounds (KAI382, KAI389, KAI394, KAI404, KAI414, and KAI422) were in the low micro-molar range on hOCT1 and hOCT3 (1.4 ~ 8.4 μM), and were higher for hOCT2. This trend was not observed in mOcts; IC_{50} values for test compounds on mOct2 were smaller than mOct1 and mOct3. MDK018 and KAI419 had the worst inhibitory effects on OCTs, while KAI414 had the highest inhibitory effect on OCTs. Most inhibition was observed in hOCT1 and hOCT3, and since hOCT1 is not as highly expressed in the brain compared with hOCT2 and hOCT3, administering these test compounds *in vivo* might work favorably towards inhibition of hOCT3. The present study suggests that novel OCT inhibitors might have the potential to produce antidepressant-like effects through inhibiting the uptake-2 system, and test compounds with high affinities towards OCTs could be used as lead compounds for conducting further *in vivo* studies.

In Chapters 3 and 4, we generated homology models for human, mouse, and rat OCT3, as well as for hOCT3 mutants, to evaluate and study ligand-transporter

interactions in their binding pockets. In order to rule out the possibility that loss of transport activity was due to lack of transporter expression in the plasma membrane, experiments using hOCT3 and FLAG antibodies to perform western blot analysis and/or immunocytochemistry on functional and non-functional hOCT3 mutant transfected cell lines are ongoing. For future studies, docked hOCT3 substrates other than MPP^+ should be used to perform saturation assays in order to verify the importance of residues identified in docking studies. In addition, besides comparing homology models among orthologs, OCT paralogs should also be considered. This could be done by generating homology models for hOCT1 and hOCT2. Analyzing their binding pockets could help us understand their functional differences. Even though no residue subject to non-synonymous SNP as been identified to form the binding pocket for hOCT3, one of the naturally occurring SNPs, Gly475Ser, is located next to the binding pocket. A 3-D homology model of this mutant could be generated and used to analyze the potential changes in its binding pocket and transport function, which might be associated with alterations in compound disposition observed *in vivo*. Another major reason for conducting homology modeling is to better understand compound-transporter interactions and generate a pharmacophore for a series of compounds in order to guide future rational drug design or screening for potential substrates/inhibitors, and even to use this information to avoid drug-drug interactions.

In Chapter 5, we assessed the inhibitory effects of a series of test compounds on both human and mouse OCTs. Compounds with high affinities towards OCTs should be used as lead compounds and tested *in vivo* to evaluate their antidepressant-like effects through methods such as tail suspension test. Since major depressive disorder is

associated with decreased levels of neurotransmitters (especially 5-HT) in the CNS, 5-HT should be used as substrate instead of MPP^+ in saturation analyses, and inhibitory effects of these compounds on 5-HT transport through OCTs should be tested. These compounds should also be docked into homology models for interaction analyses. Incorporating the docking results, the chemical structures of test compounds and their binding affinities (IC_{50} values), we could extrapolate critical functional groups or pharmacophore that would facilitate inhibitory effects of the compounds, and this could be a start for rational drug design.

LIST OF REFERENCES

1. Koepsell, H., K. Lips, and C. Volk, *Polyspecific Organic Cation Transporters: Structure, Function, Physiological Roles, and Biopharmaceutical Implications.* Pharm Res, 2007. **24**(7): p. 1227-1251.
2. Giacomini, K.M. and Y. Sugiyama, *Goodman and Gilman's the pharmacological basis of therapeutics*. 11th ed. / editor, Laurence 1. Brunton ; associate editors, John S. Lazo, Keith L. Parker.. ed. Pharmacological basis of therapeutics. Vol. 1. 2006, New York: New York : McGraw-Hill.
3. Giacomini, K.M., et al., *Membrane transporters in drug development.* Nat Rev Drug Discov, 2010. **9**(3): p. 215-36.
4. He, L., K. Vasiliou, and D.W. Nebert, *Analysis and update of the human solute carrier (SLC) gene superfamily.* Human genomics, 2009. **3**(2): p. 195.
5. Koepsell, H., *The SLC22 family with transporters of organic cations, anions and zwitterions.* Molecular aspects of medicine, 2013. **34**(2-3): p. 413.
6. Jonker, J.W. and A.H. Schinkel, *Pharmacological and physiological functions of the polyspecific organic cation transporters: OCT1, 2, and 3 (SLC22A1-3).* The Journal of pharmacology and experimental therapeutics, 2004. **308**(1): p. 2.
7. Koepsell, H., B.M. Schmitt, and V. Gorboulev, *Organic cation transporters.* Rev Physiol Biochem Pharmacol, 2003. **150**: p. 36-90.
8. Dirk, G., et al., *Drug excretion mediated by a new prototype of polyspecific transporter.* Nature, 1994. **372**(6506): p. 549.
9. Emami Riedmaier, A., et al., *Metformin and cancer: from the old medicine cabinet to pharmacological pitfalls and prospects.* Trends in Pharmacological Sciences, 2012.
10. Kerb, R., et al., *Identification of genetic variations of the human organic cation transporter hOCT1 and their functional consequences.* Pharmacogenetics, 2002. **12**(8): p. 591.
11. Shu, Y., et al., *Effect of genetic variation in the organic cation transporter 1 (OCT1) on metformin action.* The Journal of clinical investigation, 2007. **117**(5): p. 1422.
12. Becker, M.L., et al., *Genetic variation in the organic cation transporter 1 is associated with metformin response in patients with diabetes mellitus.* The Pharmacogenomics Journal, 2009. **9**(4): p. 242.
13. Yan, S., et al., *Evolutionary conservation predicts function of variants of the human organic cation transporter, OCT1.* Proceedings of the National Academy of Sciences of the United States of America, 2003. **100**(10): p. 5902.

14. Itoda, M., et al., *Seven Novel Single Nucleotide Polymorphisms in the Human SLC22A1 Gene Encoding Organic Cation Transporter 1 (OCT1).* Drug Metabolism and Pharmacokinetics, 2004. **19**(4): p. 308-312.
15. Eriko, S., et al., *Human organic cation transporter (OCT1 and OCT2) gene polymorphisms and therapeutic effects of metformin.* Journal of Human Genetics, 2006. **52**(2): p. 117.
16. Fujita, T., et al., *Transport of drugs in the kidney by the human organic cation transporter, OCT2 and its genetic variants*. 2006: Hoboken. p. 25-36.
17. Leabman, M.K., et al., *Polymorphisms in a human kidney xenobiotic transporter, OCT2, exhibit altered function.* Pharmacogenetics, 2002. **12**(5): p. 395.
18. Is, S., et al., *Genetic Variants of the Organic Cation Transporter 2 Influence the Disposition of Metformin.* Clinical Pharmacology & Therapeutics, 2008. **84**(5): p. 559.
19. Kang, H.-J., et al., *Identification and functional characterization of genetic variants of human organic cation transporters in a Korean population.* Drug metabolism and disposition: the biological fate of chemicals, 2007. **35**(4): p. 667.
20. Chen, S.L., et al., *Role of organic cation transporter 3 (SLC22A3) and its missense variants in the pharmacologic action of metformin.* Pharmacogenetics and Genomics, 2010. **20**(11): p. 687-699.
21. Lazar, A., et al., *Novel mutations of the extraneuronal monoamine transporter gene in children and adolescents with obsessive– compulsive disorder.* The International Journal of Neuropsychopharmacology, 2008. **11**(1): p. 35-48.
22. Nies, A.T., et al., *Expression of organic cation transporters OCT1 (SLC22A1) and OCT3 (SLC22A3) is affected by genetic factors and cholestasis in human liver.* Hepatology, 2009. **50**(4): p. 1227-1240.
23. Okuda, M., et al., *cDNA Cloning and Functional Expression of a Novel Rat Kidney Organic Cation Transporter, OCT2.* Biochemical and Biophysical Research Communications, 1996. **224**(2): p. 500-507.
24. Nies, A.T., et al., *Organic cation transporters (OCTs, MATEs), in vitro and in vivo evidence for the importance in drug therapy.* Handb Exp Pharmacol, 2011(201): p. 105-67.
25. Kekuda, R., et al., *Cloning and functional characterization of a potential-sensitive, polyspecific organic cation transporter (OCT3) most abundantly expressed in placenta.* The Journal of biological chemistry, 1998. **273**(26): p. 15971.
26. Dirk, G., et al., *Molecular identification of the corticosterone- sensitive extraneuronal catecholamine transporter.* Nature Neuroscience, 1998. **1**(5): p. 349.
27. Wu, X., et al., *Structure, function, and regional distribution of the organic cation transporter OCT3 in the kidney.* American journal of physiology. Renal physiology, 2000. **279**(3): p. F449.
28. Wang, T., et al., *Choline Transporters in Human Lung Adenocarcinoma: Expression and Functional Implications.* Acta Biochimica et Biophysica Sinica, 2007. **39**(9): p. 668-674.
29. Sata, R., et al., *Functional analysis of organic cation transporter 3 expressed in human placenta.* The Journal of pharmacology and experimental therapeutics, 2005. **315**(2): p. 888.

30. Nicole, L.B., et al., *Organic cation transporter 3: Keeping the brake on extracellular serotonin in serotonin- transporter- deficient mice.* Proceedings of the National Academy of Sciences, 2008. **105**(48): p. 18976.
31. David-Alexandre, T., et al., *Genome- wide haplotype association study identifies the SLC22A3- LPAL2- LPA gene cluster as a risk locus for coronary artery disease.* Nature Genetics, 2009. **41**(3): p. 283.
32. Scott, A.T., et al., *Integrative molecular concept modeling of prostate cancer progression.* Nature Genetics, 2006. **39**(1): p. 41.
33. Chen, E.C., et al., *Targeted disruption of organic cation transporter 3 attenuates the pharmacologic response to metformin.* Molecular pharmacology, 2015. **88**(1): p. 75.
34. Koepsell, H. and H. Endou, *The SLC22 drug transporter family.* Pflugers Arch - Eur J Physiol, 2004. **447**(5): p. 666-676.
35. Fakhoury, M., *Revisiting the Serotonin Hypothesis: Implications for Major Depressive Disorders.* Mol Neurobiol, 2016. **53**(5): p. 2778-2786.
36. Akk, L., et al., *The treatment of psychotic depression: Is there consensus among guidelines and psychiatrists?* Journal of Affective Disorders, 2012.
37. Cho, S.K., et al., *Verapamil decreases the glucose-lowering effect of metformin in healthy volunteers.* British Journal of Clinical Pharmacology, 2014. **78**(6): p. 1426-1432.
38. Administration, F.a.D., *Guidance for industry: drug interaction studies-study design, data analysis, implications for dosing, and labeling recommendations*. 2012.
39. Agency, E.M., *Guideline on the Investigation of Drug Interactions*. 2010.
40. Popp, C., et al., *Amino acids critical for substrate affinity of rat organic cation transporter 1 line the substrate binding region in a model derived from the tertiary structure of lactose permease.* Molecular pharmacology, 2005. **67**(5): p. 1600.
41. Vyas, V.K., et al., *Homology Modeling a Fast Tool for Drug Discovery: Current Perspectives.* Indian Journal of Pharmaceutical Sciences, 2012. **74**(1): p. 1-17.
42. Ramachandran, S. and N.V. Dokholyan, *Homology Modeling: Generating Structural Models to Understand Protein Function and Mechanism*, in *Computational Modeling of Biological Systems: From Molecules to Pathways*, N.V. Dokholyan, Editor. 2012, Springer US: Boston, MA. p. 97-116.
43. Xiang, Z., *Advances in homology protein structure modeling.* Curr Protein Pept Sci, 2006. **7**(3): p. 217-27.
44. Chothia, C. and A.M. Lesk, *The relation between the divergence of sequence and structure in proteins.* The EMBO journal, 1986. **5**(4): p. 823.
45. Bioinformatics, R.C.f.S. *Protein Data Bank*. Feb 2017; Available from: http://www.rcsb.org/pdb/home/home.do.
46. Kopp, J. and T. Schwede, *The SWISS-MODEL Repository of annotated three-dimensional protein structure homology models.* Nucleic acids research, 2004. **32**(Database issue): p. D230.
47. Hilbert, M., G. Böhm, and R. Jaenicke, *Structural relationships of homologous proteins as a fundamental principle in homology modeling.* Proteins: Structure, Function, and Bioinformatics, 1993. **17**(2): p. 138-151.
48. Maurer-Stroh, S., W.-C. Wong, and F. Eisenhaber, *Not all transmembrane helices are born equal: Towards the extension of the sequence homology concept to membrane proteins.* Biology Direct, 2011. **6**(1): p. 57.

49. Takeda-shitaka, M., et al., *Protein Structure Prediction in Structure Based Drug Design.* Current Medicinal Chemistry, 2004. **11**(5): p. 551-558.
50. Francoijs, C.J.J., J.P.G. Klomp, and R.M.A. Knegtel, *Sequence annotation of nuclear receptor ligand- binding domains by automated homology modeling.* Protein Engineering Design and Selection, 2000. **13**(6): p. 391-394.
51. Leelananda, S.P. and S. Lindert, *Computational methods in drug discovery.* Beilstein J Org Chem, 2016. **12**: p. 2694-2718.
52. Pubmed, N. *Basic Local Alignment Search Tool*. Available from: https://blast.ncbi.nlm.nih.gov/Blast.cgi.
53. Dublin, U. *ClustalX*. [cited 2016; Available from: http://www.clustal.org/clustal2/.
54. Sali, A., *Modeller*. 2016.
55. Ravna, A.W., et al., *Membrane Transporters: Structure, Function and Targets for Drug Design*, in *Transporters as Targets for Drugs*, S. Napier and M. Bingham, Editors. 2009, Springer Berlin Heidelberg: Berlin, Heidelberg. p. 15-51.
56. Schlessinger, A., et al., *SLC Classification: An Update.* Clinical Pharmacology & Therapeutics, 2013. **94**(1): p. 19.
57. Gorboulev, V., et al., *Selectivity of the polyspecific cation transporter rOCT1 is changed by mutation of aspartate 475 to glutamate.* Molecular pharmacology, 1999. **56**(6): p. 1254.
58. Gorboulev, V., et al., *Subtype- specific affinity for corticosterone of rat organic cation transporters rOCT1 and rOCT2 depends on three amino acids within the substrate binding region.* Molecular pharmacology, 2005. **67**(5): p. 1612.
59. Volk, C., et al., *Different affinities of inhibitors to the outwardly and inwardly directed substrate binding site of organic cation transporter 2.* Molecular pharmacology, 2003. **64**(5): p. 1037.
60. Schmitt, B.M., et al., *Charge-to- substrate ratio during organic cation uptake by rat OCT2 is voltage dependent and altered by exchange of glutamate 448 with glutamine.* American journal of physiology. Renal physiology, 2009. **296**(4): p. F709.
61. Zhang, X., et al., *A conserved glutamate residue in transmembrane helix 10 influences substrate specificity of rabbit OCT2 (SLC22A2).* The Journal of biological chemistry, 2005. **280**(41): p. 34813.
62. Li, D.C., C.G. Nichols, and M. Sala-Rabanal, *Role of a Hydrophobic Pocket in Polyamine Interactions with the Polyspecific Organic Cation Transporter OCT3.* The Journal of biological chemistry, 2015. **290**(46): p. 27633.
63. Huang, Y., et al., *Structure and mechanism of the glycerol- 3- phosphate transporter from Escherichia coli.* Science (New York, N.Y.), 2003. **301**(5633): p. 616.
64. Pelis, R.M., et al., *Cysteine accessibility in the hydrophilic cleft of human organic cation transporter 2.* The Journal of biological chemistry, 2006. **281**(46): p. 35272.
65. Sturm, A., et al., *Identification of cysteines in rat organic cation transporters rOCT1 (C322, C451) and rOCT2 (C451) critical for transport activity and substrate affinity.* American journal of physiology. Renal physiology, 2007. **293**(3): p. F767.
66. Wu, X., et al., *Identity of the organic cation transporter OCT3 as the extraneuronal monoamine transporter (uptake2) and evidence for the expression of the transporter in the brain.* The Journal of biological chemistry, 1998. **273**(49): p. 32776.
67. Fromm, M.F. and R.B. Kim, *Drug Transporters*. 1 ed. Handbook of Experimental Pharmacology. Vol. 201. 2011: Springer-Verlag Berlin Heidelberg.

68. Busch, A.E., et al., *Monoamine neurotransmitter transport mediated by the polyspecific cation transporter rOCT1.* FEBS Letters, 1996. **395**(2-3): p. 153-156.
69. Hayer-Zillgen, M., M. Brüss, and H. Bönisch, *Expression and pharmacological profile of the human organic cation transporters hOCT1, hOCT2 and hOCT3.* British Journal of Pharmacology, 2002. **136**(6): p. 829-836.
70. Amphoux, A., et al., *Differential pharmacological in vitro properties of organic cation transporters and regional distribution in rat brain.* Neuropharmacology, 2006. **50**(8): p. 941-952.
71. Arndt, P., et al., *Interaction of cations, anions, and weak base quinine with rat renal cation transporter rOCT2 compared with rOCT1.* American journal of physiology. Renal physiology, 2001. **281**(3): p. F454.
72. Gründemann, D., et al., *Selective substrates for non- neuronal monoamine transporters.* Molecular pharmacology, 1999. **56**(1): p. 1.
73. Kakehi, M., et al., *Functional characterization of mouse cation transporter mOCT2 compared with mOCT1.* Biochemical and Biophysical Research Communications, 2002. **296**(3): p. 644-650.
74. NIMH. *NIMH depression statistics*. [cited 2017; Available from: http://www.nimh.nih.gov/statistics/index.shtml.
75. Anderson, I.M., et al., *Evidence- based guidelines for treating depressive disorders with antidepressants: a revision of the 2000 British Association for Psychopharmacology guidelines.* Journal of psychopharmacology (Oxford, England), 2008. **22**(4): p. 343.
76. Daws, L.C., W. Koek, and N.C. Mitchell, *Revisiting serotonin reuptake inhibitors and the therapeutic potential of " uptake- 2" in psychiatric disorders.* ACS chemical neuroscience, 2013. **4**(1): p. 16.
77. Feng, N., et al., *Local inhibition of organic cation transporters increases extracellular serotonin in the medial hypothalamus.* Brain Research, 2005. **1063**(1): p. 69-76.
78. Schmitt, A., et al., *Organic cation transporter capable of transporting serotonin is up- regulated in serotonin transporter- deficient mice.* Journal of Neuroscience Research, 2003. **71**(5): p. 701-709.
79. Kitaichi, K., et al., *Behavioral changes following antisense oligonucleotide-induced reduction of organic cation transporter- 3 in mice.* Neuroscience Letters, 2005. **382**(1): p. 195-200.
80. Duan, H. and J. Wang, *Impaired monoamine and organic cation uptake in choroid plexus in mice with targeted disruption of the plasma membrane monoamine transporter (Slc29a4) gene.* The Journal of biological chemistry, 2013. **288**(5): p. 3535.
81. Dickens, D., et al., *Lamotrigine is a substrate for OCT1 in brain endothelial cells.* Biochemical Pharmacology, 2012. **83**(6): p. 805-814.
82. Geier, E.G., et al., *Profiling Solute Carrier Transporters in the Human Blood–Brain Barrier.* Clinical Pharmacology & Therapeutics, 2013. **94**(6): p. 636.
83. Lin, C.J., et al., *Cellular localization of the organic cation transporters, OCT1 and OCT2, in brain microvessel endothelial cells and its implication for MPTP transport across the blood- brain barrier and MPTP- induced dopaminergic toxicity in rodents.* Journal of Neurochemistry, 2010. **114**(3): p. 717-727.

84. Busch, A.E., et al., *Human neurons express the polyspecific cation transporter hOCT2, which translocates monoamine neurotransmitters, amantadine, and memantine.* Molecular pharmacology, 1998. **54**(2): p. 342.
85. Naganuma, F., et al., *Predominant role of plasma membrane monoamine transporters in monoamine transport in 1321N1, a human astrocytoma- derived cell line.* Journal of Neurochemistry, 2014. **129**(4): p. 591-601.
86. Mei, C., et al., *The organic cation transporter- 3 is a pivotal modulator of neurodegeneration in the nigrostriatal dopaminergic pathway.* Proceedings of the National Academy of Sciences, 2009. **106**(19): p. 8043.
87. Duan, H. and J. Wang, *Selective transport of monoamine neurotransmitters by human plasma membrane monoamine transporter and organic cation transporter 3.* The Journal of pharmacology and experimental therapeutics, 2010. **335**(3): p. 743.
88. Wang, L. and D. Sweet, *Renal Organic Anion Transporters (SLC22 Family): Expression, Regulation, Roles in Toxicity, and Impact on Injury and Disease.* AAPS J, 2013. **15**(1): p. 53-69.
89. Zwart, R., et al., *Impaired Activity of the Extraneuronal Monoamine Transporter System Known as Uptake- 2 in Orct3/ Slc22a3- Deficient Mice.* Molecular and Cellular Biology, 2001. **21**(13): p. 4188.
90. Shnitsar, V., et al., *Expression of human organic cation transporter 3 in kidney carcinoma cell lines increases chemosensitivity to melphalan, irinotecan, and vincristine.* Cancer research, 2009. **69**(4): p. 1494.
91. Breining, P., et al., *High expression of organic cation transporter 3 in human BAT- like adipocytes. Implications for extraneuronal norepinephrine uptake.* Molecular and Cellular Endocrinology, 2017. **443**: p. 15-22.
92. Pedersen, B.P., et al., *Crystal structure of a eukaryotic phosphate transporter.* Nature, 2013. **496**(7446): p. 533-6.
93. Yadav, V., et al., *A phosphate transporter from the root endophytic fungus Piriformospora indica plays a role in phosphate transport to the host plant.* J Biol Chem, 2010. **285**(34): p. 26532-44.
94. Wang, L. and D.H. Sweet, *Potential for food-drug interactions by dietary phenolic acids on human organic anion transporters 1 (SLC22A6), 3 (SLC22A8), and 4 (SLC22A11).* Biochem Pharmacol, 2012. **84**(8): p. 1088-95.
95. *GOLD*. 2015, Cambridge Crystallographic Data Centre.
96. *SYBYL-X Suite*. Certara.
97. SBC. *Phobius*. Available from: http://phobius.sbc.su.se/.
98. Haenisch, B., et al., *Interaction of antidepressant and antipsychotic drugs with the human organic cation transporters hOCT1, hOCT2 and hOCT3.* Naunyn-Schmiedeberg's Arch Pharmacol, 2012. **385**(10): p. 1017-1023.
99. NIMH. *NIMH Depression*. [cited 2017; Available from: https://http://www.nimh.nih.gov/health/topics/depression/index.shtml.
100. Pascal, A., et al., *Transport of biogenic amine neurotransmitters at the mouse blood–retina and blood–brain barriers by uptake1 and uptake2.* Journal of Cerebral Blood Flow & Metabolism, 2012. **32**(11): p. 1989.
101. *Lipofectamine 2000 Reagent*. 2013, invitrogen by life technologies.
102. *Plasma Membrane Protein Extraction Kit*. 2014, Abcam.

103. Bordo, D. and P. Argos, *Suggestions for " safe" residue substitutions in site-directed mutagenesis.* Journal of Molecular Biology, 1991. **217**(4): p. 721-729.
104. Zhu, H.-J., et al., *Evaluation of organic cation transporter 3 (SLC22A3) inhibition as a potential mechanism of antidepressant action.* Pharmacological Research, 2012. **65**(4): p. 491-496.
105. Dukat, M., et al., *2- Amino- 6- chloro- 3,4- dihydroquinazoline: A novel 5- HT3 receptor antagonist with antidepressant character.* Bioorganic & Medicinal Chemistry Letters, 2013. **23**(21): p. 5945-5948.
106. Svenaeus, F., *Diagnosing mental disorders and saving the normal: American Psychiatric Association, 2013. Diagnostic and statistical manual of mental disorders, 5th ed. American Psychiatric Publishing: Washington, DC. 991 pp., ISBN: 978-0890425558. Price: $122.70.* Med Health Care and Philos, 2014. **17**(2): p. 241-244.
107. APAF. *Quantifying the Cost of Depression*. [cited 2017; Available from: http://www.workplacementalhealth.org/Mental-Health-Topics/Depression/Quantifying-the-Cost-of-Depression.
108. Wikipedia. *Major Depressive Disorder*. [cited 2017; Available from: https://en.wikipedia.org/wiki/Major_depressive_disorder#cite_note-3.
109. Little, A., *Treatment-resistant depression.* Am Fam Physician, 2009. **80**(2): p. 167-72.
110. Rahman, S. and M.T. Bardo, *Environmental enrichment increases amphetamine-induced glutamate neurotransmission in the nucleus accumbens: A neurochemical study.* Brain Research, 2008. **1197**: p. 40-46.
111. K., L.-K., *The global burden of disease: generating evidence, guiding policy.* Institute for Health Metrics and Evaluation, 2013.
112. Al-Harbi, K.S., *Treatment-resistant depression: therapeutic trends, challenges, and future directions.* Patient Prefer Adherence, 2012. **6**: p. 369-88.
113. Rahman, A.A., et al., *Conformationally- Restricted analogues and partition coefficients of the 5-HT 3 serotonin receptor ligands meta- Chlorophenylbiguanide (mCPBG) and meta- Chlorophenylguanidine (mCPG).* Bioorganic & Medicinal Chemistry Letters, 2003. **13**(6): p. 1119-1123.
114. Koepsell, H., *Substrate recognition and translocation by polyspecific organic cation transporters.* Biol Chem, 2011. **392**(1-2): p. 95-101.

VITA

Hebing Liu was born in Harbin, China. She received her Bachelor of Science degree in Basic Pharmacy in 2013 in China Pharmaceutical University, Nanjing, China. She joined Department of Pharmaceutics, Virginia Commonwealth University (VCU) in 2013.

During her PhD education, Hebing has published two abstracts and presented her research in the Annual Meetings of American Association of Pharmaceutical Scientists (AAPS) in 2015 and 2016, the Lowenthal Symposium in 2016, as well as poster presentation within School of Pharmacy, VCU.

During these four years, Hebing received Jyotsan and Mavji Thakker Award, Lowenthal Award, Phi Kappa Phi Award, PCEU-GSA-AAPS Student Travel Award (twice), Graduate Training/Travel Fund, Peter and Sian Byron General School of Pharmacy Graduate Student Travel Award, as well as the VCU Graduate School Dissertation Assistantship. She worked as an adjunct professor for Department of Biology for one semester teaching population genetics, and is also planning on continuing her study in VCU in Department of Biostatistics after graduation.

ABSTRACTS

1. Hebing Liu and Douglas H. Sweet. Point Mutation of hOCT3 to Identify Critical Residues for Substrate Interaction. AAPS Annual Meeting and Exposition, Orlando, November 2015.
2. Hebing Liu and Douglas H. Sweet. Identification of hOCT3 Structural Elements Impacting Transporter-Substrate Interactions. AAPS Annual Meeting and Exposition, Denver, November 2016.